UNIVERSITY OF CALIFORNIA

Los Angeles

Novel Polypeptide-Based Biomaterials for Prostate Cancer Therapies

A dissertation submitted in partial satisfaction

of the requirements for the degree Doctor of Philosophy

in Bioengineering

by

Kristine Marie Mayle

2015

ABSTRACT OF THE DISSERTATION

Novel Polypeptide-Based Biomaterials for Prostate Cancer Therapies

by

Kristine Marie Mayle
Doctor of Philosophy in Bioengineering
University of California, Los Angeles, 2015
Professor Daniel T. Kamei, Chair

Prostate cancer is the second leading cause of cancer-related death among American men, and current therapies are nonspecific with many negative side effects. As described in *Chapter 1*, these side effects are generally due to inadvertent harm to healthy cells, and therefore, the development of targeted therapies can improve patient welfare, as well as improve the efficacy of current therapies. Furthermore, the materials used for these therapies should be biocompatible and avoid undesired immune responses. One type of novel biomaterial is the polypeptide, which is comprised of amino acids that have a wide variety of chemical and physical properties. Polypeptides can also be designed to adopt secondary structures, such as alpha-helices, as well as self-assemble into macromolecular structures, such as nano-sized vesicles. Using polypeptides as the "core" material in this thesis, we have developed and investigated (i) novel cell penetrating peptides comprised of galactosylated poly(methionine), which can efficiently internalize into prostate cancer cells, and (ii) photoresponsive polypeptide-based gold nanoshells, where gold-coated polypeptide vesicles generate heat in response to near infrared light to kill cancer cells.

Naturally-occurring cell penetrating peptides, such as HIV-Tat, are generally cationic, with an abundance of the positively-charged amino acids arginine and lysine. Researchers have shown that synthetic polypeptides can be created to mimic the primary and secondary structures of natural cell penetrating peptides. Furthermore, these synthetic polypeptides can be modified to increase their internalization efficiency to outperform the natural peptides, for example, through incorporation of alpha-helical structures, cationic and functional side chains, and hydrophobic moieties. In *Chapter 2*, we investigated a novel polypeptide material synthesized by Dr. Timothy Deming's lab at UCLA for use as a cell penetrating peptide, galactosylated poly(methionine). To optimize the polypeptide, we performed cytotoxicity and fluorescent cellular uptake studies using polypeptides with a variety of properties, such as chain length and percent functionalization with galactose groups. We determined that the 50% functionalized galactosylated poly(methionine) was non-toxic to cells, and demonstrated significantly greater cellular uptake compared to nona-arginine (R9), which is known to be efficiently internalized by cells. This novel polypeptide represents a promising biomaterial for delivering anti-cancer therapies to prostate cancer cells.

The second focus of this thesis has been the use of self-assembled vesicles comprised of the block copolypeptide, poly(L-lysine)$_{60}$-*b*-poly(L-leucine)$_{20}$ ($K_{60}L_{20}$), as the core material for photothermal therapy using near infrared light. Researchers have developed gold nanostructures, which demonstrate enhanced absorption of light due to surface plasmon resonance (SPR). The SPR of the gold nanostructures can be tuned to a variety of wavelengths, ranging from ultraviolet to visible to the near infrared. In order to non-invasively treat tumors beneath the skin, near infrared light is desired, where light at this wavelength can penetrate a few centimeters into the tissue. Gold nanoshells, where a core material is coated with a thin layer of gold, have been

shown to generate heat in response to irradiation with near infrared light. The core materials used for gold nanoshells include solid silica nanoparticles, polymeric nanoparticles, and more recently, liposomes. In *Chapter 3*, we report the first ever use of polypeptide materials as the core material for a gold nanoshell. Our polypeptide based $K_{60}L_{20}$ gold nanoshells have demonstrated low toxicity in the absence of laser exposure, significant heat generation upon exposure to near infrared light, and as a result, localized cytotoxicity within the region of laser irradiation. In *Chapter 4*, we demonstrate the ability to reduce the overall size of the polypeptide-based gold nanoshells, so that they are in the size range to take advantage of the enhanced permeability and retention (EPR) effect, which leads to the collection of nanoparticles at a solid tumor site. These smaller gold nanoshells similarly demonstrated significant heat generation in response to near infrared irradiation and localized laser-induced cytotoxicity. To gain a better understanding of our gold nanoshells in the context of photothermal therapy, we developed a comprehensive mathematical model for heat transfer in *Chapter 5* to predict the temperature as a function of time and position in our *in vitro* experimental set-up. Our mathematical model was validated by comparing our predictions with our experimental results. This model can therefore be used in the future to determine which parameters in our gold nanoshells can be manipulated to improve heat generation, and therefore, potentially improve the destruction of tumors.

In *Chapter 6*, we conjugated a targeting ligand, the A11 minibody, to the polypeptide-based $K_{60}L_{20}$ gold nanoshells to improve their efficacy. Researchers have shown that active targeting agents, such as proteins and antibodies, can improve the specificity and effectiveness of photothermal therapy for cancer cells. The A11 minibody, which binds specifically to the prostate stem cell antigen (PSCA) overexpressed on the surfaces of local and metastatic prostate cancer cells, has successfully been demonstrated by Dr. Anna Wu's group at UCLA as a positron

emission tomography (PET) imaging agent for prostate cancer with *in vivo* models. Here, we demonstrate the first use of the A11 minibody to target a therapeutic agent to prostate cancer cells. Specifically, we were able to generate A11-conjugated nanoshells with the appropriate size and heat generation properties. These PSCA-targeted polypeptide-based gold nanoshells also showed promise by exhibiting greater efficacy as a photothermal therapy agent compared to non-targeted gold nanoshells.

This dissertation of Kristine Marie Mayle is approved.

Timothy J. Deming

Warren S. Grundfest

Anna M. Work

Daniel T. Kamei, Committee Chair

University of California, Los Angeles

2015

To Revan, my rock, and Stella, my happiness

TABLE OF CONTENTS

1 MOTIVATION AND BACKGROUND 1

1.1 PROSTATE CANCER 1

1.2 ENHANCING THE SPECIFICITY OF PROSTATE CANCER TREATMENT 2

1.3 NOVEL POLYPEPTIDE MATERIALS 3

1.3.1 Synthesis of Polypeptide Materials 4

1.3.1.1 Solid Phase Polypeptide Synthesis 4

1.3.1.2 Synthesis of Polypeptides using Recombinant DNA Technology 6

1.3.1.3 NCA Polymerization 7

1.4 THESIS OVERVIEW 10

2 GLYCOSYLATED POLY(METHIONINE) AS A NOVEL CELL PENETRATING PEPTIDE 11

2.1 CELL PENETRATING PEPTIDES 11

2.2 MATERIALS AND METHODS 15

2.2.1 Polypeptide Materials 15

2.2.2 Conversion of Concentration for Polypeptides 16

2.2.2.1 Convert from Molar Polypeptide Concentration to Molar Amino Acid Concentration 17

2.2.2.2 Convert from Molar Polypeptide Concentration to Mass Polypeptide Concentration 18

2.2.3 Cell Culture 18

2.2.4 Cytotoxicity of Polypeptides 19

2.2.5 Cellular Uptake 19

2.2.6 Cellular Uptake in an Excess Galactose Environment 20

2.2.7 Quantification of Uptake Using ImageJ (M-Gal 10, 50% versus R9) 21

2.2.8 Statisical Analysis of ImageJ Results 21

2.3 RESULTS AND DISCUSSION 22

2.3.1 Galactose Pendant Side Chain Groups for Functionalized Poly(methionine) 22

2.3.2 Altering the Percent Functionalization of the Galactosylated Poly(methionine) 23

2.3.3 Specificity of Uptake by Galactosylated Poly(methionine) 29

2.3.4 Comparison with an Established Cell Penetrating Peptide, Nona-Arginine 32

2.4 CONCLUSIONS 35

3 POLYPEPTIDE-BASED GOLD NANOSHELLS FOR PHOTOTHERMAL THERAPY 36
3.1 PHOTOTHERMAL THERAPY 36
3.2 MATERIALS AND METHODS 41
3.2.1 Materials 41
3.2.2 Synthesis of Block Copolypolypeptides 42
3.2.3 Coating of Gold Nanoshells 42
3.2.4 Characterization of Gold Nanoshells 43
3.2.5 Cytotoxicity of Gold Nanoshells 43
3.2.6 Measuring Heat Generation 43
3.2.7 Photothermal Therapy 44
3.3 RESULTS AND DISCUSSION 44
3.3.1 Making Polypeptide-Based Gold Nanoshells 44
3.3.2 Measuring Heat Generation from Gold Nanoshells 49
3.3.3 Photothermal Therapy Using Polypeptide-Based Gold Nanoshells 50
3.4 CONCLUSIONS 52
4 OPTIMIZATION OF THE POLYPEPTIDE-BASED GOLD NANOSHELLS 53
4.1 MATERIALS AND METHODS 53
4.1.1 Optimized $K_{60}L_{20}$ Processing 53
4.1.2 Optimized Gold Coating Procedure 54
4.1.3 Characterization of Gold Nanoshell Concentration 54
4.1.4 Cytotoxicity of Gold Nanoshells 55
4.1.5 Measuring Heat Generation 55
4.1.6 Photothermal Therapy 55
4.2 RESULTS AND DISCUSSION 56
4.2.1 Reduction of the $K_{60}L_{20}$ Gold Nanoshell Diameter 56
4.2.2 Use of the Optimized Gold Nanoshells for Photothermal Therapy 60
4.3 CONCLUSIONS 62
5 MATHEMATICAL MODELING OF THE HEAT TRANSFER ASSOCIATED WITH THE $K_{60}L_{20}$ GOLD NANOSHELLS 63
5.1 METHODS 65

5.1.1 Model 1: Macroscopic Energy Balance – Bulk Heating *65*

5.1.2 Model 2: Differential Conservation of Energy Equation – Heat Generation at All Nodes *67*

5.1.3 Model 3: Combination of Models 1 and 2 - Heat Generation Only Within the Laser Irradiated Region *74*

5.2 RESULTS AND DISCUSSION 79

5.2.1 Model 1: Macroscopic Energy Balance – Bulk Heating *79*

5.2.2 Model 2: Differential Conservation of Energy Equation – Heat Generation at All Nodes *80*

5.2.3 Model 3: Combination of Models 1 and 2 – Heat Generation only within the Laser Irradiated Region *83*

5.3 MODEL 4: RELAXING ASSUMPTIONS MADE IN MODEL 3 85

5.3.1 Heat Conduction from Irradiated Region *85*

5.3.2 Attenuation of the Laser Power Along the Z-Direction *87*

5.3.3 Scattering of Light by Gold Nanoshells *88*

5.3.4 Increased Heat Loss at the Boundaries *88*

5.3.4.1 Heat Transfer Coefficients 88

5.3.4.2 Evaporative Cooling at the Air-Liquid Interface 90

5.3.5 Modeling Heat Generation for our Optimized Polypeptide-Based Gold Nanoshells *91*

5.4 CONCLUSIONS 93

6 INVESTIGATING TARGETED POLYPEPTIDE-BASED GOLD NANOSHELLS 94

6.1 POTENTIAL FOR PSCA-TARGETED THERAPEUTICS USING THE A11 MINIBODY 94

6.2 MATERIALS AND METHODS 96

6.2.1 Synthesis of A11 Minibody *96*

6.2.2 Making Polypeptide-Based Gold Nanoshells *96*

6.2.3 Conjugation Scheme for A11 and PEG to Polypeptide-Based Gold Nanoshells *97*

6.2.4 Characterization of A11-Conjugated Gold Nanoshells *98*

6.2.5 Measuring Heat Generation *98*

6.2.6 Photothermal Therapy Using A11-Conjugated Nanoshells *98*

6.3 RESULTS AND DISCUSSION 99

6.3.1 A11-Conjugated Polypeptide-Based Gold Nanoshells *99*

6.3.2 PSCA-Targeted Photothermal Therapy Using Polypeptide-Based Gold Nanoshells *102*

6.4 SPECIFICITY OF A11-PSCA INTERACTION 103

6.5 CONCLUSIONS 104

7 APPENDIX 106

7.1 MATLAB CODE FOR MODEL 2 106

7.2 MATLAB CODE FOR MODEL 3 108

7.3 MATLAB CODE FOR MODEL 4 110

7.4 DETERMINING THE INTERNALIZATION RATE CONSTANT AND CELLULAR ASSOCIATION OF A11 MINIBODY 112

7.4.1 Materials and Methods *112*

7.4.1.1 Radiolabeling A11 Minibody 112

7.4.1.2 Cellular Binding and Trafficking 112

7.4.1.3 Mathematical Model of A11 Trafficking 113

7.4.1.4 Development of A11-Conjugated PEGylated Nanocarriers 116

7.4.1.5 Qualitative Cellular Uptake of Nanocarriers 117

7.4.2 Results and Discussion *117*

7.4.2.1 Evaluate the Internalization Rate Constant for the A11 Minibody 117

7.4.3 Evaluating Targeting of Nanosized Carrier Using the A11 Minibody *120*

8 REFERENCES 121

Acknowledgments

My family has played a strong role in building my confidence in myself and my abilities, telling me from a young age that I can be whatever I want and encouraging me to pursue those dreams.

To my dad: Every time I speak to my father, he reminds me how proud he is of me, that I should keep up the good work, and that he loves me. My whole life, he has been the voice that I hear cheering me on to the next level, he has been the person I look to for work ethic, and he is the person that grounds me in my roots.

To my mom: When I look at my mother, I see a fighter, who is brave, laughs whole heartedly at silly stories, and cares deeply about the people she loves. Speaking to my mother, she reminds me to be kind and to smile, even when times get tough.

To my Pap Samer: My grandfather passed away when I was very young, but I still feel his love and adoring gaze. In our short time together, he taught me to cherish each moment, as tomorrow is never promised to anyone.

To my grandma: My grandmother taught me to be strong, to lead, to be unconditionally supportive. In the future, I know that I will be able to get through anything, as her voice will forever be a part of me.

To my Uncle Mark: My uncle is quiet and steady. He is the calm voice in my head when times get tough. When I think of him, I am reminded to move slowly and purposefully through life.

To my little brother: My brother has always been creative and sensitive, he is empathetic and cares deeply about each and every person and animal. I am inspired by his love, which

knows no limits, and his patience, which allows him to stand by the people he loves in times of happiness, as well as hardship.

To Jamie, my best friend, my sister: She has always been my alter ego, my adventurous and daring side. Through it all, she's the person I can call, who will not think twice about standing up for me against any person or problem. Jamie has impacted my life in so many ways, I am a better person having her as my best friend.

To my Pap Charlie: He was kind and firm, and demonstrated strength that I did not know was possible. When I was in high school, he faced cancer, and although the battle was lost, I still remember the smile on his face, his squeezing hugs, and how much love I felt in his arms.

To Ted: Through my graduate studies, he has supported me, helped push me through the difficult times, and rejoiced in my successes as if they were his own. He has become one of my truest friends and cheerleaders in my life.

I have also been fortunate to have had a series of people, who have altered the course of my life, guiding me to where I am today.

To Jim Bartrug: Among softball skills, he taught me to take risks, to support the other players, and to change your angle or strategy when something isn't working. I never worried about winning or losing in summer softball, knowing that Jim was on the third base line, we were going to give everything we had, and that was enough. He taught me how a true leader guides his team to championships and beyond.

To Bryan Selph: He taught me to expand my comfort zone in an unknown area. As a young engineering co-op in a manufacturing plant, he sent me out to the production floor alone.

“Go explore,” he said, “talk to people.” I remind myself of these words to help push my own boundaries in life.

To Julie Fiore: My mentor at DuPont was known as “Queen of Specialty”. She was an engineer and she ran the department. Watching her in action, I realized I wanted to be in that position, I wanted to be the person everyone looked to for the answers, for direction. She taught me to ask questions, to communicate my ideas, and to explore my abilities.

To Jenn: My graduate student mentor was a Ph.D. candidate at the time. Thank you for the opportunity to grow and explore the life of a graduate student. She patiently listened and answered all my questions, allowed me to be independent, and gave me sound guidance when needed. I model my mentoring style after her approach.

This leads me to the Kamei Lab, where I have laughed, cried, grown, and blossomed. My Ph.D. experience has been shaped and molded by the members, both past and present. Meeting a Kamei lab member, you have an instantaneous bond, they quickly become your closest friend. It truly is a family and I have so many people to thank for taking me into their hearts.

To Dan: I have learned from Dan to place a critical eye on everything I see, hear, and touch. I look for and identify asymmetry and minute details others often miss. This trained skill was developed under his guidance, and I have attempted to pass the techniques onto my undergraduate students, so that they may also approach one step closer to his success. With Dan’s critical eye also comes immense love for his students, he cares deeply about their success, and not just present success. He builds us all to become successful leaders, researchers, and people for the future. You will not meet a person, who will be more honest in the face of challenges, more supportive in times of doubt, or more willing to go the distance for those he

cares about. I knew from the moment that I met Dan, I needed to be a part of this lab. I wanted his guidance and support throughout my graduate studies, and I knew I wanted his passion and commitment as a guide for the next stages of my life.

To Ricky: He has been my mentor and friend throughout my Ph.D. I turned to him as my voice of reason through grad school, he listened to my complaints, my fears, my worries, then promptly reminded me of my goals, my potential, and my strength. He has been the force reminding me to never give up, and he taught me to persevere through difficult times.

To Garrett: My partner in crime, my twin. We have been through the entire experience together, where we grew from competitors for a lab position, to casual friends, to close confidants. In lab, he challenges me to ask more difficult questions, to check my beliefs, and to take a moment to relax when it's needed. Kamei Lab experience would not have been the same without him.

To the Kamei lab graduate students: Past and present members, each one holds a special place in my Ph.D. memories. Mike, David, Sherine, and Brad made up my graduate student support team during my graduate studies. Mike taught me the polypeptide vesicle work, guiding me to one day become his "replacement". He was always willing to help anyone, and he reminded us of the importance of sacrifice for the good of others. David amazes me with his strength and drive, he is an inspiration to the lab for his dedication to everything he does. Sherine is and will be a force, she is strong and determined. I look forward to watching her grow. With a little under a year in our lab, Brad has integrated himself fully into the lab, and I see much of myself in his personality. I think he will be a great addition to the Kamei Lab Family.

To my undergraduate team: Bob, Cory, Katie, Vincent, and Kevin. They are strong people, full of energy and passion. Bob, my first teammate, was my partner. He is steadfast and loyal, a true friend. His smile and personality lights up a room, and I know he will go on to be a great leader. Cory was trained by Bob, and has a similarly infectious smile and personality. He began our journey to the development of the gold nanoshells, and even as he's moved on to pursue his life's passions, he's continued to be a supportive member of my team. Katie is very intelligent, she approaches problems in unique ways, giving her a clarity to identify creative solutions. Vincent's excitement and enthusiasm combined with hard work and dedication will prove him successful in all his endeavors. Kevin has grown quickly and efficiently into a bold and decisive researcher. Each person contributes a special talent to our subgroup. They have demonstrated the ability to work independently and collaboratively to achieve our collective goals, and I am so proud to be their mentor.

I have been fortunate to work with an amazing team, and the successes that I have been able to attain would not have been possible without them.

In addition to my direct team of researchers, Allison, Sam, Stephanie, and Alison are undergraduates, who I had the pleasure of watching grow during their time in the Kamei Lab. They have demonstrated grace in their journey from young students to independent researchers. Developing their professional etiquette, presentation skills, and lab skills, I am so humbled by their progress and their attitude toward the rapid and long-lasting changes. As a whole, Kamei Lab undergraduates are unique people, they are brave and ambitious. They join our lab for only a brief time, but their impact on current and future generations is unrivaled in most laboratory experiences.

In addition to the support from the Kamei Lab, there have been a number of people, who have gone beyond my expectations during my time at UCLA.

To the Di Carlo Lab: You are all a significant part of my experience at UCLA. As I have grown, I have also watched you all grow. I get excited watching you give presentations on your work, and I enjoy the smiles and conversations as we pass through our days. I feel lucky to have such an amazing group of people, who are also standing by to support me. Thank you.

To the Deming Lab: Collaboration with Professor Deming and his students has given me a unique experience. Meetings with Professor Deming allowed me to expand my thought process to understand the chemistry and synthesis techniques, and their distinctive challenges. I enjoyed working with his students, where Jessica, in particular, has become my colleague and friend that I will continue to look to for guidance and support.

To the Grundfest Lab: Thank you to Jun and Zach for helping bring my idea for a near infrared laser-triggered photothermal therapy agent to fruition. We would not have been able to quickly and successfully evaluate our technology without your help. I appreciate your willingness to listen and answer all my questions about a field that I had little to no experience with.

Finally, I have been so lucky to have found and built a happiness support network.

To Arash: Thank you for making sure I have a continuous stream of adventures and excitement in my life. Since you came into my life, I have pursued new activities and I have pushed the limits of my exploration. I appreciate all the little things and the support for any crazy idea I have. It's amazing to be adored for my kindness, intelligence, and energy.

To Revan and Stella: Revan has been my pillow when I was sad, my book prop when I was studying, and my patient listener for all my practice talks. I am so thankful to have brought you home with me that fall day and kept you close by always. Stella has taught me patience and poise. She fears the world, and therefore I must guide her and remind her of her own strength. At home, she is loving, kind, and loyal. She brings me joy as she reminds me to jump into life fully, as each movement she makes is full of heart and power.

As for the sections of my thesis, I would like to make the following acknowlegments:

Chapter 1, Section 1.3 is a version of U.-J. Choe, V. Z. Sun, J.-K. Y. Tan, and D. T. Kamei, *Self-Assembled Copolypeptide and Polypeptide Hybrid Vesicles: From Synthesis to Application*. Top Curr Chem, 2012, 310, 117-134, Springer Copyright © 2012. Adapted with permission of Springer.

Chapter 2 is a version of Kramer J, Schmidt N, Mayle KM, Kamei DT, Wong G, Deming TJ. "Reinventing cell penetrating peptides using glycosylated sulfonium ion sequences." American Chemical Society Central Science (Accepted: March 27, 2015). Note this is an open access article published under an ACS AuthorChoice Licence, which permits copying and redistribution of the article or any adaptations for non-commercial purposes. Dr. Timothy Deming was the director of research for this article. This work was supported by a grant from the National Science Foundation (DMR 1308081). Confocal laser scanning microscopy was performed at the CNSI Advanced Light Microscopy/Spectroscopy Shared Resource Facility at UCLA, supported with funding from NIH-NCRR shared resources grant (CHE-0722519).

Chapters 3-5 are being combined in preparation for publication. Dr. Daniel T. Kamei was the director of research for these thesis sections. This work was supported by a grant from the

National Science Foundation (DMR 1308081) to Dr. Timothy J. Deming and Dr. Daniel T. Kamei, as well as the National Science Foundation Graduate Research Fellowship (DGE-1144087) to Kristine M. Mayle.

Chapter 6 is also currently in preparation for publication. Dr. Daniel T. Kamei was the director of research for these thesis sections. This work was supported by a grant from the National Science Foundation (DMR 1308081) to Dr. Timothy J. Deming and Dr. Daniel T. Kamei, as well as the National Science Foundation Graduate Research Fellowship (DGE-1144087) to Kristine M. Mayle.

Kristine M. Mayle

Los Angeles, CA 90028
linkedin.com/in/kristinemayle
(740) 632-9459
kristinemayle@ucla.edu

Education

Ph.D. Candidate in Bioengineering, Molecular Cellular Tissue Therapeutics Track
University of California Los Angeles
Thesis Advisor: Dr. Daniel T. Kamei

B.S. in Chemical Engineering, Minor in Biology
Ohio University, Athens, Ohio: June 2010
GPA 3.80 overall; 3.80 in major, 3.97 in minor

Awards & Honors

Bruin Development Academy – Consulting, 2015-present
Committee of 200 Scholar, 2013-present
National Science Foundation Graduate Research Fellowship, 2012-present
UCLA Tech Forum Student Poster Competition - 2nd Place, UCLA 2013
Tau Beta Pi Outstanding Senior Nominee, Ohio University 2010
Outstanding Co-op Award, Ohio University 2010
Amgen Scholars Program, University of California San Diego, Summer 2009

Publications

Kramer J, Schmidt N, Mayle KM, Kamei DT, Wong G, Deming TJ. "Reinventing cell penetrating peptides using glycosylated sulfonium ion sequences." *American Chemical Society Central Science* (Accepted: March 27, 2015).

Mayle KM, Le AM, and Kamei DT. "The intracellular trafficking pathway of transferrin." *Biochim. Biophys. Acta* **1820** (2012): 264-81.

Singelyn JM, Sundaramurthy P, Johnson TD, Schup-Magoffin PJ, Hu DP, Faulk DM, Wang J, Mayle KM, Bartels K, Salvatore M, Kinsey AM, Demaria AN, Dib N, Christman KL. "Catheter-deliverable hydrogel derived from decellularized ventricular extracellular matrix increases endogenous cardiomyocytes and preserves cardiac function post-myocardial infarction." *J Am Coll Cardiol. **59** (2012): 751-63.*

Kummitha C, Mayle KM, Christman MA 2nd, Deosarkar SP, Schwartz AL, McCall KD, Kohn LD, Malgor R, Goetz, DJ. "A Sandwich ELISA for the Detection of Wnt5a." *Journal of Immunological Methods* **352** (2010): 38-44.

Research Experience

Dr. Daniel T. Kamei's Lab, University of California Los Angeles (UCLA)
Graduate Student Researcher, January 2011-present

- Developing and using novel nano-sized polypeptide biomaterials and engineered proteins for specific, targeted, and noninvasive prostate cancer treatment

Dr. Karen Christman's Lab, University of California San Diego (UCSD)
Amgen Scholar Undergraduate Research Assistant, Summer 2009

- Investigating the use of myocardial matrix for support the heart following a myocardial infarction

Dr. Doug Goetz's Lab, Ohio University - Athens, OH
Undergraduate Research Assistant, 2007-2009

- Developing novel diagnostic tests for the detection of Wnt5a using enzyme-linked immunosorbent assay (ELISA) technology

Presentations	**2012 UC Systemwide Bioengineering Conference,** UC Berkeley, CA *Oral Presentation* "Targeting prostate cancer using the A11 minibody." Mayle KM, Chiu RYT, Lamm RJ, Knowles S, Wu AM, Kamei DT. **2012 Biomedical Engineering Society Annual Meeting,** Atlanta, GA *Poster Presentation* "Prostate Cancer Drug Delivery Using the A11 Minibody." Mayle KM, Chiu RYT, Lamm RJ, Knowles S, Wu AM, Kamei DT. **2013 UCLA Tech Forum,** UC Los Angeles, CA *Poster Presentation* "Prostate Cancer Drug Delivery Using the A11 Minibody." Mayle KM, Chiu RYT, Lamm RJ, Knowles S, Wu AM, Kamei DT. **2013 UC Systemwide Bioengineering Conference,** UC San Diego, CA *Oral Presentation* "Transferrin Receptor-Targeted Block Copolypeptide Vesicles for the Delivery of Chemotherapeutics." Mayle KM, Choe UJ, Rodriguez AR, Lee BS, Yip AT, Deming TJ, Kamei DT. *Poster Presentation* "A11-Meidated Drug Delivery for the Treatment of Prostate Cancer." Mayle KM, Chiu RYT, Lamm RJ, Knowles S, Wu AM, Kamei DT. **2013 Biomedical Engineering Society,** Seattle, WA *Oral Presentation* "Enhanced Delivery of Chemotherapeutics using Targeted Block Copolypeptide Vesicles." Mayle KM, Choe UJ, Rodriguez AR, Lee BS, Yip AT, Deming TJ, Kamei DT. *Poster Presentation* "Using the A11 Minibody to Target Prostate Cancer." Mayle KM, Chiu RYT, Lamm RJ, Knowles S, Wu AM, Kamei DT. **2014 UC Systemwide Bioengineering Conference,** UC Irvine, CA *Oral Presentation* "Development of Targeted Systemic Treatments for Metastatic Prostate Cancer using Engineered Ligands." Mayle KM, Chiu RYT, Wang SJ, Dern KR, Lamm RJ, Knowles S, Mason AB, Wu AM, Kamei DT. **2014 Biomedical Engineering Society,** San Antonio, TX *Poster Presentation* "Targeting Metastatic Prostate Cancer using Engineered Ligands." Mayle KM, Chiu RYT, Wang SJ, Dern KR, Lamm RJ, Knowles S, Mason AB, Wu AM, Kamei DT.
Teaching Experience	**BE 100: Bioengineering Fundamentals (Thermodynamics),** UCLA *Teaching Assistant, Prof. Daniel T. Kamei*, Winter 2012 **BE 110: Biotransport and Bioreaction Processes,** UCLA *Teaching Assistant, Prof. Daniel T. Kamei*, Spring 2011, 2012 **BE 201/101: Engineering Principles for Drug Delivery ,** UCLA *Teaching Assistant, Prof. Daniel T. Kamei*, Fall 2011, Fall 2012, Fall 2013 **BE 495: Teaching Assistant Training Seminar** UCLA *Teaching Associate, Prof. Daniel T. Kamei*, Fall 2014
Outreach Work	**UCLA Engineering High School Summer Research Program,** UCLA *Graduate Student Mentor*, Summer 2012 **High School Engineering Outreach,** Hollywood High School *Interactive Presentation*, 2013 "Using Engineering to improve cancer therapies" **SASE White House STEM Initiative,** UCLA *Teacher and Course Designer*, 2015 "Engineering Better Medicines"
Industry	**DuPont Specialty Compounding,** DuPont Washington Works- Washington, WV *Co-operative Engineer with Assistant to Operations Support*, 2007- 2008

1 Motivation and Background

1.1 Prostate Cancer

Nearly 1 in 6 American men will be diagnosed with prostate cancer, and 1 in 36 American men will die from the disease, where prostate cancer is the second leading cause of death among this population[1]. Current treatment depends on the patient's age and tumor stage at diagnosis, whether it is localized and non-metastatic, or if it has already spread to other areas of the body. For localized tumors, options include active surveillance, surgical resection, and radiation therapy. If the prostate cancer spreads to other areas of the body, for example lymph nodes or bones, more aggressive treatment is necessary. Some options for metastatic tumors are hormone therapy and chemotherapy, which are generally administered systemically.

Both localized and systemic treatment options often have severe side effects[2]. Surgical resection, or radical prostatectomy, have long term side effects, such as urinary incontinence and sexual dysfunction. Electron beam radiation therapy, while less invasive, can lead to urinary, bowel, and erectile dysfunction. Systemic treatment options also often harm healthy cells throughout the body, leading to greater effects throughout the body. Hormone therapy, such as androgen deprivation therapy, can result in additional long-term symptoms and conditions in patients, such as breast swelling, hot flashes, anemia, and osteoporosis. If hormone therapy is ineffective, chemotherapeutic agents, such as docetaxel, may be used, however common side effects include nausea, hair loss, and immunodeficiency. Based on the severe short- and long-term side effects, there is a need for more specific treatment of prostate cancer, which avoids harm to healthy cells.

1.2 Enhancing the Specificity of Prostate Cancer Treatment

In order to prevent harm to healthy cells, researchers have been developing more specific therapies, which can target tumor tissue, bind to receptors and antigens on cancer cells, and facilitate uptake into cells, as well as remain inert until triggered by an external source.

Many prostate cancer treatments have been developed to take advantage of the prostate cancer biology. Tumors are characterized by poorly structured, leaky blood vessels, as well as a deficient lymphatic drainage system. Therefore, passive targeting of tumor tissue can be achieved through the use of particles with diameters in the range of 60-400 nm, which accumulate at the tumor site due to this distinctive morphology; a phenomenon known as the enhanced permeability and retention (EPR) effect[3]. Many researchers have created nano-sized drug delivery vehicles, such as polymeric nanoparticles, liposomes, and polypeptide vesicles, which demonstrate increased tumor targeting and efficacy when encapsulated with an anti-cancer drug. Furthermore, many cancer cells overexpress receptors and tumor-specific antigens, due to the need to acquire nutrients, growth factors, and signaling molecules to sustain their rapid growth and proliferation. Active targeting of cancer cells can be achieved through the attachment of biomolecules, such as proteins and antibodies, to specifically bind receptors and antigens on the surfaces of cancer cells. Furthermore, certain active targeting agents, such as proteins and cell penetrating peptides, can also facilitate uptake into cancer cells, enabling intracellular delivery of attached anti-cancer drugs. Incorporating features, such as passive and active targeting to tumor tissue, can improve the likelihood for delivery of anti-cancer drugs for the specific treatment of prostate cancer.

To prevent non-specific harm to healthy cells, researchers are also investigating focal therapies, which can be triggered by an external stimulus. Triggered therapy allows for spatial and temporal control of treatment, which avoids harming healthy cells. In triggered therapies, the therapy and the trigger alone are designed to not harm cells separately, only the combination of the therapy and trigger will result in cytotoxicity. Some examples of focal treatments undergoing clinical trials include: high intensity focused ultrasound[4], cryosurgery[4], and photothermal therapy[5]. These investigational treatments have shown promise as methods for treating cancer, while avoiding harm to healthy cells to prevent short- and long-term side effects.

The development of improved, specific prostate cancer therapies requires the use of biocompatible materials, where both natural and synthetic polymers have been used, ranging from poly(lactic-co-glycolic acid) to lipids to synthetic polypeptides. Synthetic polypeptide materials have shown promise as novel biomaterials as they incorporate a wide variety of chemical and physical properties using natural and unnatural amino acid building blocks. Polypeptide-based biomaterials have been used for several applications, such as improving drug delivery efficacy with cell penetrating peptides for enhancement of the uptake of anti-cancer therapeutics and with vesicular drug carriers through the macromolecular self-assembly of polypeptides. The focus of my thesis will be on the application of novel polypeptide materials to engineer more specific treatments for prostate cancer.

1.3 Novel Polypeptide Materials

This thesis focused on using polypeptide-based materials as the "core" of the therapeutic approach. Polypeptide-based biomaterials have shown promise in the development of drug delivery vehicles and targeting agents. Due to the wide variety of natural and synthetic amino

acid building blocks, it is possible to develop materials with a wide variety of physical and chemical properties. Additionally, polypeptides have the ability to adopt stable secondary structures, which enable self-assembly into supramolecular structures, such as vesicles. Recent advances in polymerization techniques have led to precise control over the polypeptides, resulting in easier customization and uniformity. Although the introductions to each of the subsequent chapters provide additional background material relevant for this thesis, the following sections in this chapter have focused on summarizing methods that have been used to create polypeptide materials, where polypeptides are defined here as polymers consisting of 20 or more amino acids, which is consistent with definitions found in the literature[6].

1.3.1 Synthesis of Polypeptide Materials

Recent advances in polypeptide synthesis have enabled the development of polypeptides, which incorporate additional functionality and secondary structures. Preparation of the primary structure of polypeptides requires special techniques, including solid phase synthesis, protein engineering, and N-carboxyanhydride (NCA) polymerization.

1.3.1.1 Solid Phase Polypeptide Synthesis

Polypeptides up to 50 amino acid residues can be synthesized using solid-phase peptide synthesis (SPPS)[7–9]. In this method, the peptide chain is assembled onto a solid bead (resin) using a process of repeated coupling and deprotection steps as each amino acid is added, followed by release of the peptide into solution when completed. Briefly, an amino acid is covalently anchored to the resin, and the free amine group on the amino acid is available to create an amide bond with a single protected amino acid, producing a dipeptide. Deprotection of the amino acid, reveals a free amine group, which can bind the next protected amino acid, further

lengthening the peptide chain. Repeated coupling and deprotection of single amino acids results in the formation of a precisely controlled peptide. While this technique has a high yield (~99%) for each amino acid addition step, the final polypeptide yield is generally low due to a certain number of chains acquiring a defect at each step. Furthermore as the chain length increases, there is an exponential increase in defects, where 50-mer and 100-mer peptides have a yield of only 60% and 37%, respectively[7,10,11]. Therefore, SPPS has typically been limited to polypeptide chains of ~50 amino acids[12].

In order to address this limitation, researchers have investigated methods to create longer peptides through combination of polypeptides formed through SPPS. One method is the native chemical ligation (NCL) method, where an unprotected synthetic polypeptide segment with a C-terminal α-thioester is reacted in a chemoselective manner with the N-terminal cysteine residue of another unprotected polypeptide segment[13]. This ligation technique requires the presence of a cysteine group at the N-terminus, and polypeptides lacking this amino acid at this position will first need to add a cysteine, which may result in disruption of the polypeptide construct. Other methods, which improve upon the drawbacks of NCL, are enzymatic ligation techniques, such as the subtiligase catalyzed fragment condensation (SCFC) method. Unlike NCL, SCFC only requires a free N-terminal amino group[14]. In this case, the subtiligase enzyme selectively catalyzes the condensation reaction between a polypeptide segment with an activated polypeptide ester and a free N-terminal amino group on a second segment. Thus, through the process of ligation, longer polypeptide chains can be formed from SPPS synthesized polypeptide blocks of approximately 50 amino acids with higher overall yields[12].

1.3.1.2 Synthesis of Polypeptides using Recombinant DNA Technology

Polypeptides have also been formed through the use of recombinant DNA technology, where genes are designed to encode for amino acid sequences to create peptides with desired features[10]. Researchers have taken advantage of this technology to precisely define peptides with near absolute monodispersity[15]. In this field, novel peptides have been designed based on two main approaches: selection of peptides, which perform a desired function, and repurposing peptide domains to achieve functions distinct from their native application[16]. In this way, a variety of unique, multifunctional polypeptides can be created by modular combination of peptide domains. Novel designs have been developed based on mimicking naturally occurring proteins, high throughput screening of peptide sequences, and the use of computational modeling.

There are three main steps to development of polypeptides using protein engineering: design, encoding, and producing the polypeptide sequence. In the design stage, the peptides with desired functionality are selected, the structural orientation of the peptide sequences, and the necessary amino acid sequences are selected. Next, the corresponding gene can be incorporated into a genetic vector, which is appropriate for expression in the host of interest, such as *Escherichia coli* (*E. coli*). Finally, transfection of the host organism can result in production of the polypeptide through overexpression of the gene, which is followed by thorough purification and characterization of the product.

While protein engineering can enable the development of novel polypeptides, there are several challenges to using these techniques. Careful selection of peptide sequences is important as long distance amino acid interactions, can affect structure and function. For example, the

amino acid sequence and organization of the peptides can affect the polypeptide solubility under different environmental conditions, such as pH, temperature, and salt concentration. Furthermore, in initial attempts to develop protein engineered polypeptides, peptide sequences were limited to naturally occurring amino acids, making it difficult to incorporate synthetic functional groups, such as alkenes and alkynes[17,18]. However, molecular biology techniques have enabled the incorporation of unnatural amino acids, which has been thoroughly reviewed previously[19]. In order to achieve a high yield and decrease unwanted downstream interactions of amino acid residues, protein engineering has primarily been limited to the synthesis of peptide domains 5-50 amino acids in length, and more specifically, the field of peptide-forming vesicles has focused the use of this technique to develop short oligopeptide sequences[20–22,16]. Other challenges to overcome include the selection of host organisms, especially in cases where post-translational modifications are needed, and purification of contaminants, and extensive characterization to identify possible genetic mutations or product denaturation. However, based on the success of large scale recombinant protein production for commercial applications, there is promise in using this approach in the future to synthesize multifunctional polypeptides with desired functionality.

1.3.1.3 NCA Polymerization

To synthesize high molecular weight chains of polypeptides the most general and common technnique is ring opening polymerization (ROPs) of α-amino acid-N-carboxyanhydride (NCA) monomers[23–26], which are readily prepared from commercially available amino acids[27]. Polypeptides of greater than 200 amino acids in length have been made with a high yield and in large quantities using this technique.

The first step of NCA polymerization is usually accomplished by the use of nucleophilic initiators, such as alkoxides, alcohols, amines, transition metals, and water[28]. There are two main schemes proposed for the NCA polymerization: the amine and activated monomer mechanisms, where the pathway is likely to switch back and forth between the two resulting mechanisms in undesired side reactions[29]. In the amine mechanism, shown in Figure 1.1, the chain grows linearly with monomer conversion through nucleophilic ring opening polymerization in the absence of side reactions. For the activated monomer mechanism, shown in Figure 1.2, the NCA monomer is deprotonated, becoming a nucleophile that can initiate chain growth. Previously, this method was hindered by significant side reactions, such as chain termination and chain transfer, which affect the control and predictability of the molecular weight distribution of the polymers. Recent advances in synthesis techniques have improved polymerization through NCA polymerization.

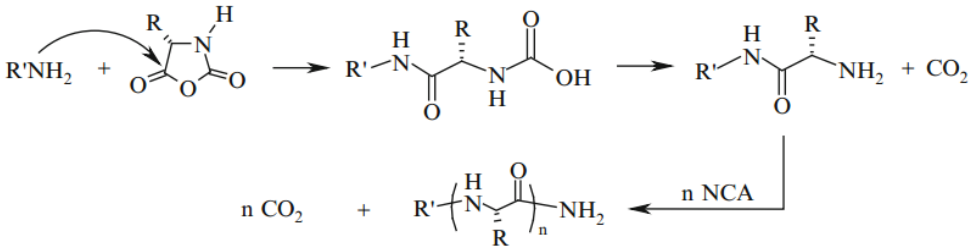

Figure 1.1. Proposed mechanism for NCA polymerization initiated by nucleophilic amines[29]. (Reprinted with permission from Synthesis of Polypeptides by Ring-Opening Polymerization of α-Amino Acid N-Carboxyanhydrides. Cheng J., Deming T. Top Curr Chem. 2012 310: 1-26. Copyright 2011. Springer-Verlag Berlin Heidelberg)

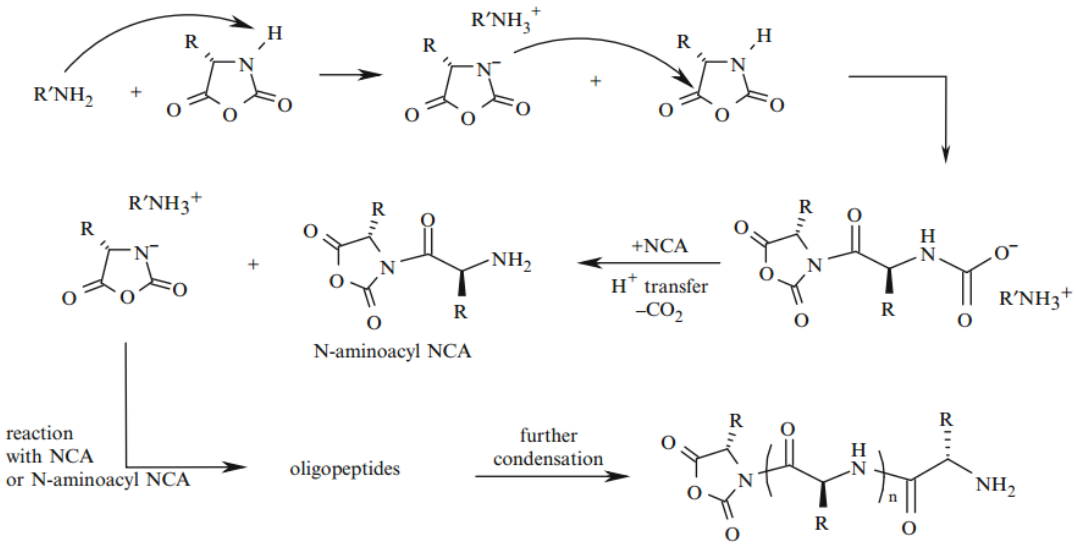

Figure 1.2. Proposed mechanism for NCA polymerization initiated by activated monomers[29]. (Reprinted with permission from Synthesis of Polypeptides by Ring-Opening Polymerization of α-Amino Acid N-Carboxyanhydrides. Cheng J., Deming T. Top Curr Chem. 2012 310: 1-26. Copyright 2011. Springer-Verlag Berlin Heidelberg)

One method employed to avoid the side reactions is the use of transition metal complexes to control the addition of NCA monomers to polymer chain ends, which results in improved reaction sensitivity and efficiency[30]. Initiators, such as zerovalent nickel and cobalt, were developed by Deming, and can react by oxidative addition across anhydride bonds in NCA monomers[31,32]. Living polymerization can then occur with the initiated metallacyclic complex through the addition of desired NCA monomers. This technique has been used to produce monodisperse polymers with controlled molecular weights, as well as defined sequence and composition[33–35]. In order to provide greater biofunctionality and the ability to self-assemble into ordered conformations, side-chain functionality and block copolypeptides have been developed using this method. In this thesis, we investigated polypeptides that were synthesized by the Deming Laboratory using transition-metal-mediated NCA polymerization. These polypeptides

included novel cell penetrating peptides with glycosylated side chains and block copolypeptides, which can self-assemble into polypeptide vesicles

1.4 Thesis Overview

In this thesis, polypeptide-based biomaterials were used to develop (i) novel cell penetrating peptides made from sugar-functionalized poly(methionine) and (ii) polypeptide-based gold nanoshells for photothermal therapy. To deepen our understanding of the transient heating associated with the laser irradiated gold nanoshells, we developed an extensive mathematical model for heat transfer that requires the use of numerical methods and MATLAB coding to predict our *in vitro* experimental data. Finally, we investigated the conjugation of a minibody to enable targeting to prostate cancer cells and enhance the efficacy of the polypeptide-based gold nanoshells.

2 Glycosylated Poly(methionine) as a Novel Cell Penetrating Peptide

2.1 Cell Penetrating Peptides

Certain proteins have been observed to be efficiently internalized into cells. Within these proteins, researchers discovered certain peptide sequences that are crucial for efficient cellular interaction and uptake, which have been aptly named cell penetrating peptides (CPPs). Some examples include penetratin, the 16-mer peptide derived from the third helix homeodomain of Antennapedia, and the Tat-derived 11-mer peptide derived from the HIV-Tat (transactivator of transcription) protein (Table 2.1). The naturally-derived CPPs are typically 9- to 35-mer cationic sequences composed of mainly arginine, lysine, and histidine amino acids. Furthermore, these naturally-derived CPPs have demonstrated effective intracellular delivery of cargo, such as nucleic acids and nanoparticle systems. Typical characteristics of CPPs include: low cytotoxicity, ability to efficiently cross the cell membrane for a variety of cell types, dose-dependent efficiency, and no restriction with respect to size or type of cargo[36,37].

Table 2.1. Cell penetrating peptides (Adapted with permission from Cell-Penetrating Peptides: Design, Synthesis, and Applications Dana Maria Copolovici, Kent Langel, Elo Eriste, and Ülo Langel ACS Nano 2014 8 (3), 1972-1994[36]. Copyright 2014 American Chemical Society)

Peptide	Sequence	Origin
Tat (48-60)[38,39]	GRKKRRQRRRPPQ	HIV-1 Tat
Penetratin[40]	KQIKIWFQNRRMKWKK	Drosophila Antennapedia homeodomain
MAP[41]	KLAKLAKALKAALKLA	Model amphipathic peptide (MAP)
Transportan/TP10[42,43]	GWTLNS/AGYLLGKINKALAALAKKIL	Galanin-Lysine-mastoparan
VP22[44]	NAKTRRHERRRKLAIER	Herpes simplex virus
Polyarginine[45]	R_n, n=(8,9)	Positively charged sequence
MPG[46]	GALFLGFLGAAGSTMGA	A hydrophobic domain from the fusion sequence of HIV gp41 and NLS of Simian Virus 40 (SV40) T-antigen
Pep-1[47]	KETWWETWWTEWSQPKKKRKV	NLS from Simian Virus 40 large T-antigen and reverse transcriptase of HIV-1
pVEC[48]	LLILRRRIRKQAHAHSK	Vascular endothelial (VE)-cadherin
YTA2[49]	YTAIAWVKAFIRKLRK	MMP cleavage site as seeding sequence
YTA4[49]	IAWVKAFIRKLRKGPLG	MMP cleavage site as seeding sequence
M918[50]	MVTVLFRRLRIRRACGPPRVRV	The tumor suppressor protein p14ARF
CADY[51]	GLWRALWRLLRSLWRLLWRA	Derived from the PPTG1 peptide

TP10 – transportan 10, VP22 – *Herpes simplex virus* (HSV) *type I* structural protein, NLS – nuclear localization signal, and pVEC – vascular endothelial cadherin-derived CPP, MMP – matrix metalloproteinase

Some general characteristics have been identified as important for designing the peptide sequence for optimal cellular uptake[36]. In general, effective CPPs are polycationic, where the positive charges enable them to interact strongly with the net negatively charged cell membrane. For example, the transacting activator of transcription (Tat) of the human immunodeficiency virus (HIV), Antennapedia homeodomain from *Drosophilia*, and VP22 from the herpes simplex virus carry charges of +8e, +7e, and +15e, respectively [52]. Similarly, homopolymers of arginine have demonstrated significant cellular internalization[45]. Additionally, many CPPs exhibit

amphipathic properties through primary and/or secondary structures, such as MAP, MPG, and Pep-1. Two types of amphipathic peptides exist: (1) primary amphipathic peptides containing both hydrophobic and hydrophilic residues, or domains, and (2) secondary amphipathic peptides adopting a conformational state, which positions the hydrophobic and hydrophilic residues on opposite sides of the molecule[53]. Using these basic design criteria, researchers have developed trial and error techniques and computational models to predict sequences that will be efficiently internalized by cells. Furthermore, recent advances in polymerization and conjugation chemistry techniques enable facile synthesis of polypeptides with precise control of the amino acid sequence and incorporation of desired functionality.

Synthetic CPPs range from simple polycationic homopolymers of cationic amino acids, such as polylysine and polyarginine, to more complex synthetic peptides, which can incorporate various positively charged amino acids and pendant side chains, or groups of molecules that are conjugated to the backbone of the chain. The high charge density of the naturally occurring CPPs enable strong binding to anions on the cell membrane, such as phosphates and sulfates. To mimic the membrane interaction of natural CPPs, many synthetic peptides have been designed using cationic amino acids, as well as positively charged pendant side chains groups, such as amine and phosphonium side chains[54,55]. Once bound to the cell membrane, CPPs may be internalized through direction translocation, where pores are formed in the cell membrane, or through an endocytosis mechanism, such as caveolae-mediated endocytosis.

To enhance cellular uptake, hydrophobic domains and secondary structure have been incorporated into the peptide. It has been shown that optimization of the hydrophobic content of the peptides has enabled greater cellular uptake, where the hydrophobic domain assists in

membrane translocation. The hydrophobic sequence destabilizes the membrane following interaction with hydrophobic lipid moieties on the cell surface, where some model studies have suggested direct transduction of amphipathic peptides occurs through pore formation, carpet-like perturbations, or inverted micelles formed in the bilayer membrane[56–58]. For example, studies have shown that increasing the hydrophobicity of the side chains and/or the backbone of the chain has enhanced the cellular uptake of peptides[54,59–62]. A balance of hydrophobic and hydrophilic domains, or amphipathic character, has been shown to be the essential criterion for translocation of peptides.

Finally, many amphipathic CPPs, such as transportan 10 (TP10) and MAP, adopt a secondary structure during interaction with the cellular membrane, which enhances membrane insertion and translocation. To create synthetic CPPs with secondary structure, the researchers must consider the charge, hydrogen bonding, and helicity of the peptide. While helical peptides can easily be made from hydrophobic amino acids, they typically have limited biological application due to low water solubility. Therefore researchers have developed methods to improve solubility and biofunctionality of alpha-helical peptides through the incorporation of hydrophilic side chains, such as sugar groups[63], as well as incorporate charge-containing amino acid groups, which have been known to destabilize helices[26]. Furthermore, researchers have demonstrated that cellular uptake can be improved through the synthesis of alpha-helical polypeptides[26,54,64]. Based on the wide range of chemical and physical properties of natural and synthetic amino acids, as well as the ability to incorporate functional groups and secondary structures, polypeptide-based materials show promise in developing synthetic CPPs that can effectively delivery intracellular cargo.

As part of this thesis, we investigated the use of a novel cationic polypeptide as a novel synthetic cell penetrating peptide: poly(methionine) functionalized with galactose side chains. Although this polypeptide does not have an alpha helical structure, it was examined because of the incorporation of cationic backbone and sugar functional groups. For the polypeptide backbone, poly(methionine) was synthesized using transition-metal-mediated-NCA polymerization followed by conjugation of galactose side chain groups to the methionine amino acid residues along the polypeptide backbone. The poly(methionine) was functionalized with galactose groups using the novel "methionine-click" chemistry developed by Kramer and Deming[65]. The addition of galactose increases the number of bonds to the sulfur of methionine from two to three bonds, introducing a positive charge and hydrophobic groups to the hydrophilic poly(methionine) polypeptide. We found that by controlling percent functionalization of the polypeptide, the glycosylated poly(methionine) could be optimized to have low cytotoxicity and superior cellular uptake. Polypeptides made from methionine amino acids represent a new class of cell penetrating peptides, which shows promise in delivering cargo with intracellular targets in the future.

2.2 Materials and Methods

2.2.1 Polypeptide Materials

The Deming Lab synthesized the polypeptides used in this chapter using techniques developed by Kramer and Deming[63,65], except for the R9 peptide, which was purchased from AnaSpec (Fremont, CA). These polymers include glucosylated poly(L-methionine) (M-Glc) and galactosylated poly(L-methionine) (M-Gal) with a variety of chain lengths, ranging from the 10-mer (M_{10}) and 60-mer (M_{60}) poly(methionine), and different percent functionalization, ranging

from 40% to 100% glycosylated polypeptides, where 40%-100% of the methionine residues were conjugated to a sugar group.

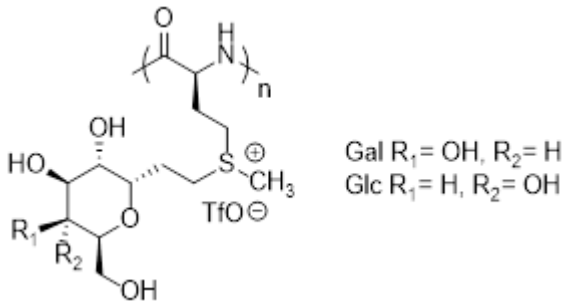

Figure 2.1. Glycosylated poly(methionine), where the side groups for R1 and R2 differ between galactosylated (Gal) poly(methionine) and glucosylated (Glc) poly(methionine)

2.2.2 Conversion of Concentration for Polypeptides

In this chapter, we primarily report the polypeptide concentrations based on mM amino acid in order to normalize effect of fluorescence for cellular uptake, since the polypeptides were labeled based on mole percent of amino acid. For illustration purposes, let's consider a situation, where a fluorescent dye is conjugated for every 10 amino acids. In this case, an M_{60} polypeptide would have 6 fluorescent molecules per chain. On the other hand, a similarly labeled M_{10} polypeptide would only have 1 fluorescent unit per chain, meaning that in order to have equal fluorescence, 6 M_{10} polypeptides would need to be used for 1 M_{60} polypeptide. In our actual study, 2 mol% fluorescent label per amino acid was used. In order to compare polypeptides of different chain lengths labeled in this manner, we needed to compare the polypeptides at the same amino acid concentration, where the fluorescence would be equal for the same uptake percentage. Table 2.2 shows the corresponding molar polypeptide concentration and mass concentrations.

Table 2.2. Conversions of concentrations for the glycosylated poly(methionine)

Polypeptide	mM Amino Acid	µM Polypeptide	mg/mL Polypeptide
M-Gal/Glc 10, 50%	0.03	3	0.007
M-Gal/Glc 10, 100%	0.03	3	0.011
M-Gal/Glc 60, 50%	0.03	0.5	0.007
M-Gal/Glc 60, 100%	0.03	0.5	0.011

The equations listed below in the following subsections were used to convert between concentrations for different chain lengths and percent functionalization.

2.2.2.1 Convert from Molar Polypeptide Concentration to Molar Amino Acid Concentration

An example calculation for the M-Gal 10 polypeptides to convert from µM polypeptide concentration to mM amino acid concentration:

$$3\ \frac{\mu mol\ polypeptide}{L} x\ \frac{1}{10^6}\frac{mol}{\mu mol} x \frac{10}{1}\frac{mol\ amino\ acid}{mol\ polypeptide} x \frac{10^3}{1}\frac{mmol}{mol} = 0.03\ mM\ amino\ acid \qquad (2.1)$$

This calculation is the same for polypeptides at any percent functionalization, since it is based on the number of amino acids per polypeptide chain.

2.2.2.2 Convert from Molar Polypeptide Concentration to Mass Polypeptide Concentration

An example calculation for M-Gal 10 at 50% functionalization to convert from polypeptide molar concentration to mass concentration, where the molecular weight of M-Gal 10, 50% is 2467 g/moL (see Table 2.3):

$$3\ \frac{\mu mol}{L}\ x\ \frac{1}{10^6}\frac{mol}{\mu mol}\ x\ 2467\ \frac{g}{mol}\ x\ \frac{10^3}{1}\frac{mg}{g}\ x\ \frac{1}{10^3}\frac{L}{mL} = 0.007\ \frac{mg}{mL} \qquad (2.2)$$

This calculation depends on the percent functionalization of the polypeptide, which affects the average molecular weight per amino acid (Table 2.3).

Table 2.3. Polypeptide molecular weight based on chain length and percent functionalization

Percent Functionalization	Average amino acid MW (g/mol)	M-Gal 10	M-Gal 60	M-Gal 15	M-Gal 35	M-Gal 45	M-Gal 55
100%	357.9	3579	21474	5369	12527	16106	19685
70%	291.18	2912	17471	-	-	-	-
50%	246.7	2467	14802	-	-	-	-
0%	135	-	-	-	-	-	-

2.2.3 Cell Culture

PC3 cell lines were obtained from the American Type Culture Collection (Manassas, Virginia). Roswell Park Memorial Institute (RPMI) 1640 cell culture media, penicillin-streptomycin (P/S), sodium pyruvate (NaPyr), phosphate buffered saline (PBS), and 0.25% trypsin with

ethylenediaminetetraacetic acid (EDTA) were purchased from Invitrogen (Carlsbad, California). Fetal bovine serum (FBS) was obtained from Hyclone (Waltham, Massachusetts). 96-well plates were purchased from Sigma-Aldrich (St. Louis, MO). The MTS cell proliferation assay kit was purchased from Promega (Madison, Wisconsin).

2.2.4 Cytotoxicity of Polypeptides

To quantify any cytotoxic effects of the various polypeptides on PC3 cells, the MTS cell proliferation assay (CellTiter 96 AQueous Non-Radioactive Cell Proliferation Assay) was used. Prior to the experiment, 96-well tissue culture plates were seeded at a density of $6x10^4$ cell/cm^2 for PC3 cells. The polypeptides were prepared in serum-free medium, which lacked fetal bovine serum (FBS), penicillin, and streptomycin, and the polypeptide concentrations were varied. After aspirating the original medium from each well, 100 µL of the prepared medium containing the polypeptides were added to each well and incubated for 5 h in a humidified environment (37°C, 5.0% CO_2). Following the incubation period, the medium containing polypeptides was aspirated. Subsequently, 20 µL of the MTS reagent was added to each well, and the plate was incubated for an additional 1 h. Cell viability relative to control wells (cells incubated in serum-free media without polypeptides) was quantified by reading the visible light absorbance values at 490 nm and 700 nm with an Infinite F200 plate reader (Tecan Systems Inc., San Jose, California).

2.2.5 Cellular Uptake

PC3 cells were seeded onto eight-well chambered coverglass units using a cell density of $6x10^4$ cells/cm^2. Fluorescently labeled polypeptides were diluted in serum-free media to the desired concentrations. Note that the overall fluorescence was measured for each sample at 0.06 mM amino acid concentration, and if necessary, unlabeled polypeptides were blended with the

labeled polypeptides to achieve equal fluorescence intensity per amino acid concentration for each sample. The cells were then incubated with the polypeptides in serum-free media for the desired time period in a 37°C humidified atmosphere with 5% CO_2. Following this incubation, the media was aspirated, and the cells were washed 3X with PBS to remove any free-floating and nonspecifically bound polypeptides before the confocal images were taken. Laser scanning confocal microscopy images were taken on a Leica Inverted TCS-SP1 MP Spectral Confocal and Multiphoton Microscope (Heidelberg, Germany) equipped with an argon laser (476 and 488 nm blue excitation: JDS Uniphase), a diode laser (DPSS; 561 nm yellow-green excitation: Melles Griot), a helium-neon laser (633 nm red excitation), and a two-photon laser setup consisting of a Spectra-Physics Millenia X 532 nm green diode pump laser and a Tsunami Ti-sapphire picosecond pulsed infrared laser tuned at 768 nm for UV excitation.

2.2.6 Cellular Uptake in an Excess Galactose Environment

PC3 cells were seeded onto eight-well chambered coverglass units using a cell density of $6x10^4$ cells/cm^2. Fluorescently labeled polypeptides were diluted to 0.03 mM amino acid sample concentrations in blank media containing 2 g/L free galactose, the same concentration as glucose in the cell culture media. The cells were then incubated with polypeptides and free galactose for 5 hrs in a 37°C humidified atmosphere with 5% CO_2. Following this incubation, the media was aspirated, and the cells were washed with PBS to remove any free-floating polypeptides that were not internalized before the confocal images were taken.

2.2.7 Quantification of Uptake Using ImageJ (M-Gal 10, 50% versus R9)

ImageJ was used to determine the average corrected total fluorescence per cell. Using the DIC and fluorescent images, the corrected total fluorescence per cell (CTFC) was calculated using the following equation (Eq. 2.3):

CTFC = integrated density – (area of selected cell x mean fluorescence of background) (2.3)

where the mean fluorescence, or mean gray value, is the sum of the gray values of all the pixels in the selection divided by the number of pixels; the area of the selected region of interest is given in μm; the integrated density is the product of the area and mean gray value; the mean fluorescence of the background is determined based on the average of 3 selections in the area where no cells are present. The mean value of the CTFC was found by averaging the CTFC for each cell in the image. The error bars represent the standard deviation.

2.2.8 Statisical Analysis of ImageJ Results

For statistical analysis, R software version 3.1.1 was used. A two-way analysis of variance (ANOVA) was performed between the peptide type (M-Gal 10, 50% and R9 (30:70 L:U)) and the peptide concentrations tested. The F values for peptide type and concentration were 123.49 and 18.32, respectively, where $p < 0.001$ for both factors. Subsequently, Tukey's honest significant difference (HSD) post-hoc test was performed to determine if there was a difference in the average corrected total fluorescence per cell between the M-Gal, 50% and R9 peptides. The difference in the means between the peptides (the mean of M-Gal 10, 50% subtracted from the mean of R9) was found to be -17624 with a 95% confidence interval of [-20631,-14616], where the p value was found to be much less than 0.05.

2.3 Results and Discussion

2.3.1 Galactose Pendant Side Chain Groups for Functionalized Poly(methionine)

In order to enhance the uptake of synthetic peptides, researchers have incorporated cationic amino acids and side chains. Cationic amino acids, such as arginine and lysine, have been shown to interact strongly with negatively charged molecules in the cell membrane resulting in greater cellular uptake. In order to introduce positive charges to the neutral poly(methionine) backbone, pendant side chains were attached through a novel "methionine click" method developed by the Deming Lab, which allows chemoselective alkylation of the methionine thioether groups[65]. The type of pendant side chain group has been shown to influence the uptake of synthetic cell penetrating peptides. Both hydrophobic and hydrophilic groups have been attached to peptides to enhance cellular uptake and enable specific-targeting to antigens or receptors on the cell surface.

Sugars, such as galactose, mannose, and fucose, are known to bind to lectins involved in endocytosis, intracellular trafficking, and nuclear import. Researchers have attached sugar groups to cationic polypeptides, such as polylysine, in order to enhance the transfection of cells[66–68]. Here, we investigated the use of galactose for the hydrophilic side chain group with the potential for cellular targeting to prostate cancer cells. Prostate cancer cells have been shown to express the galactosyl receptor, a cell surface lectin, which binds to galactose through a specific carbohydrate recognition domain[69]. Additionally, multivalent interactions of carbohydrates and lectin has been shown to enable high binding affinities and specificities[70]. Therefore, to enable strong and specific binding to the galactosyl receptor on the surface of prostate cancer cell, we functionalized each poly(methionine) with multiple galactose pendant side chains.

Initially the poly(methionine) molecules were 100% functionalized with the galactose pendant groups, using polypeptides of increasing degrees of polymerization (chain lengths). Previous studies have demonstrated that the length of the polypeptide chain can affect cellular uptake of synthetic CPPs, where longer cationic polypeptides may interact more strongly with the cell membrane. The results showed the toxicity of the galactosylated polypeptides increased with increasing chain length (Figure 2.2), likely due to the increasing overall amount of positive charges per polypeptide.

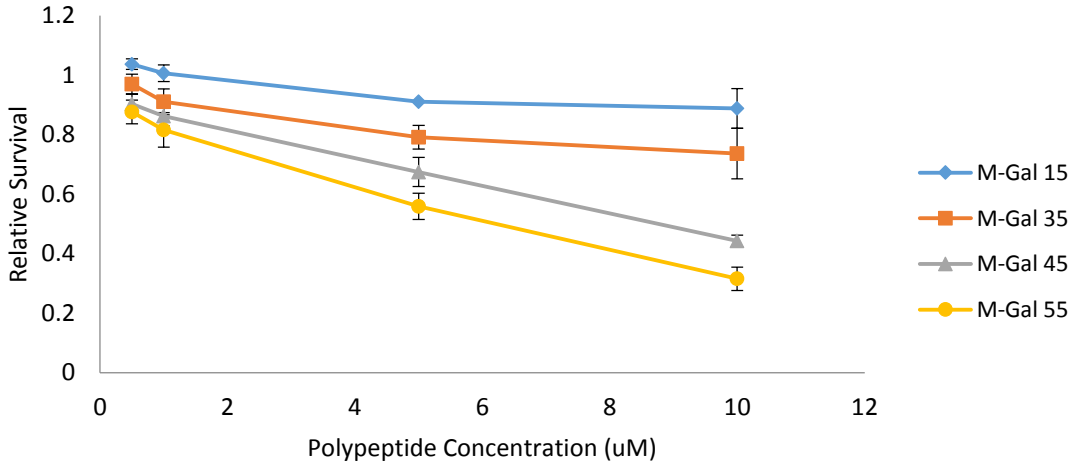

Figure 2.2. Cytotoxicity of 100% functionalized galactosylated poly(methionine) at different chain lengths reported in polypeptide concentration.

In order to reduce the toxicity of the polypeptides, especially those with the longer chain lengths, we investigated altering the number of sugar groups conjugated to the backbone, which resulted in changing the overall charge density of each polypeptide.

2.3.2 Altering the Percent Functionalization of the Galactosylated Poly(methionine)

To evaluate the effect of altering the number of sugar groups on the galactosylated poly(methionine), polypeptides were functionalized with varying amounts of galactose (Figure

2.3). As poly(methionine) is an insoluble, hydrophobic alpha-helical polypeptide, there was a minimum number of sugar groups needed to enable solubility in water (40-50% functionalization of the polypeptide chain). Conjugation of a galactose pendant side chain through alkylation of the thioether group adds a positive charge to the polypeptide by increasing the number of bonds to the sulfur group from two to three bonds. Therefore increasing the functionalization of the polypeptide will make it more cationic. Highly cationic polymers have been shown to be toxic to cells due to strong interactions with negatively charge molecules in the cell membrane.

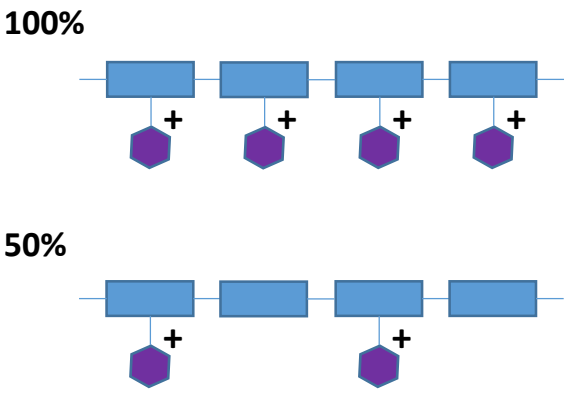

Figure 2.3. Effect of reducing the percent functionalization of the polypeptides. 100% functionalized (top) and 50% functionalized (bottom) with galactose functional groups.

As expected, increasing the number of sugar groups conjugated to the galactosylated poly(methionine) resulted in increased toxicity (Figure 2.4). In this case, we focused on the longest and shortest polypeptides, and we observed less overall toxicity for the shorter 10-mer chain lengths. To explain this result, we hypothesized that while the overall charge added is the same in each case, the number of contacts per polypeptide increases with increasing chain length (Figure 2.5). Furthermore, if we consider the entropic loss and the enthalpic gain of the

polypeptide binding to the cell, we can first assume a similar, if not slightly greater entropic loss for the longer polypeptide binding to the cell. However, for the enthalpic gain, the longer polypeptide would have a significantly greater gain compared to the shorter polypeptide. Therefore, we could expect more of the longer polypeptide to be bound to the cells, which could result in greater toxicity to the cell. Note that in this study, we evaluated the toxicity of the polypeptides based on molar amino acid concentration to coordinate with the cellular uptake studies. This represents the worst case scenario, where the 10-mer polypeptide is present in higher concentrations compared to the 60-mer as six M_{10} polypeptides have the same number of amino acid residues as one M_{60} polypeptide. However, the toxicity was still observed to be lower for the short polypeptides.

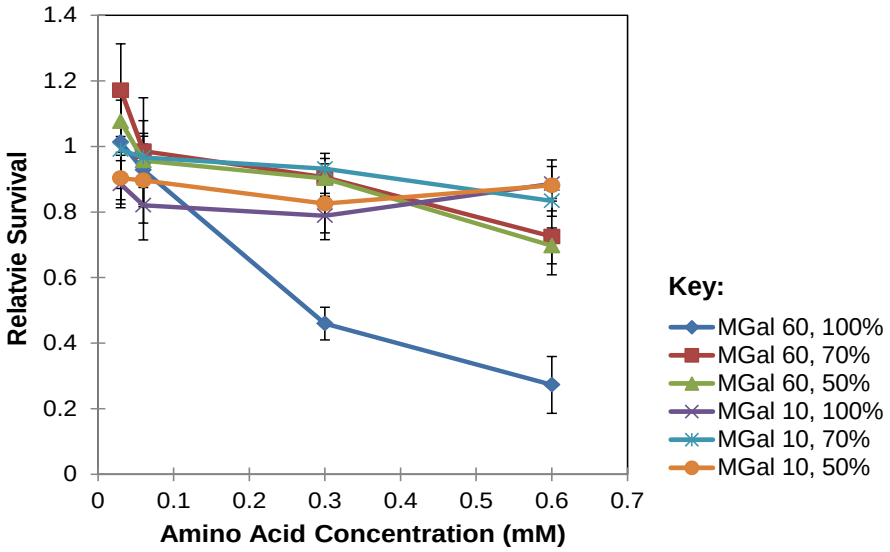

Figure 2.4. Cytotoxicity study for poly(methionine) at different percent functionalization and chain lengths.

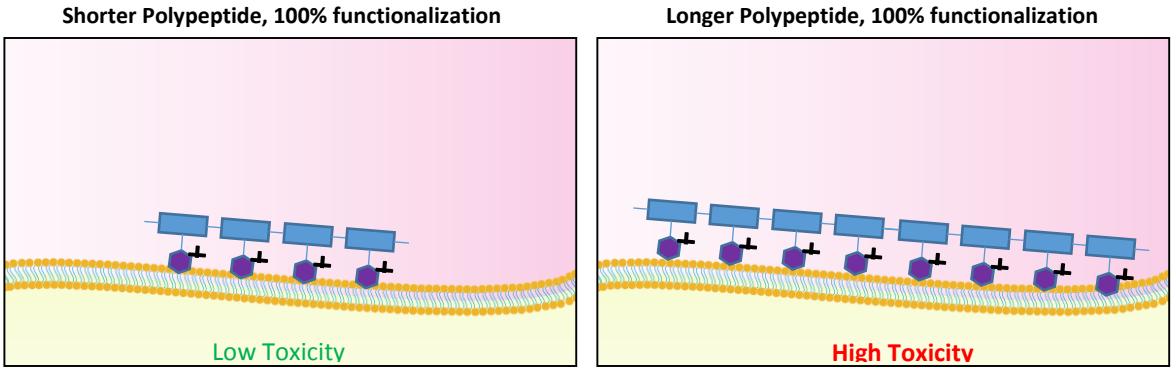

Figure 2.5. Increasing number of cell contacts per polypeptide could explain the increase in cytotoxicity for increasing chain length and percent functionalization.

Evaluation of the cellular uptake of the polypeptides at increasing percent functionalization, or numbers of sugar groups, demonstrated that highly functionalized polypeptides were less effective at entering cells (Figure 2.6). As shown in the figure, there was a trend of increasing cellular uptake with decreasing polypeptide functionalization for both short and long polypeptides, where the 50% functionalized polypeptides were found to have the greatest uptake and the lowest toxicity.

Furthermore, when the percent functionalization was set at 50%, we found no difference in the cellular uptake of galactosylated poly(methionine) at different chain lengths (Figure 2.7). Based on these results, we concluded that, when the ratio of hydrophilic to hydrophobic content is maintained constant with the 50% functionalization, maximum uptake and minimum toxicity are achieved. Other researchers have found that copolypeptides with a balance of hydrophobic and hydrophilic content improves their cellular uptake[54]. For the remainder of the studies we focused on the 50% functionalized poly(methionine).

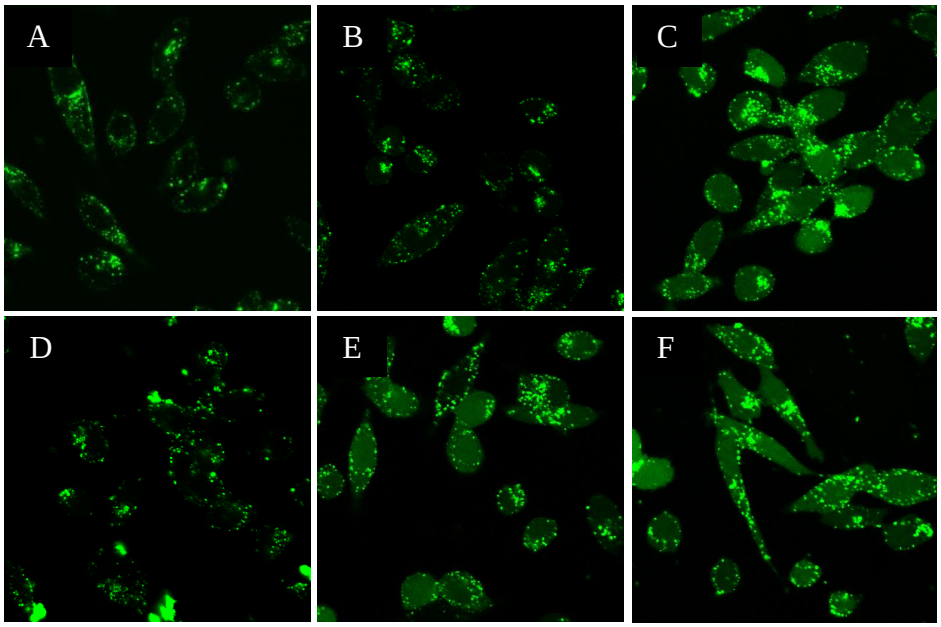

Figure 2.6. Cellular uptake of 0.03 mM amino acid (A-C) M-Gal 60 and (D-F) M-Gal 10 with different percent functionalization (A,D) 100%, (B,E) 70%, and (C,F) 50%.

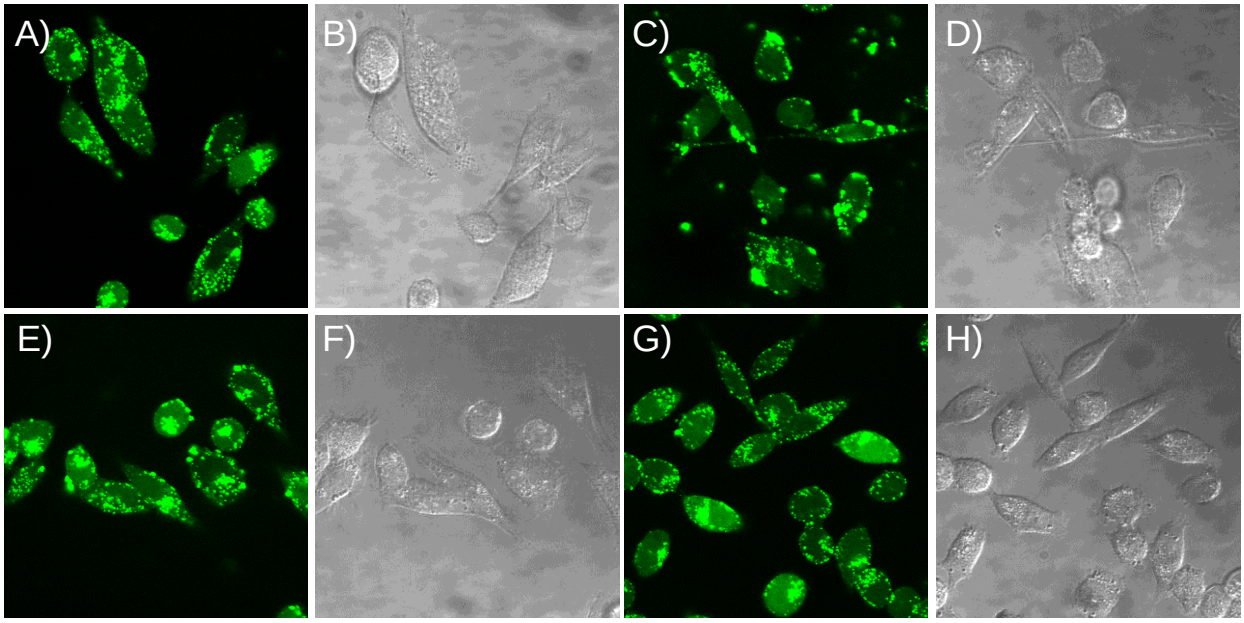

Figure 2.7. Cellular uptake study of various chain lengths of M-Gal (0.03 mM amino acid), where the percent functionalization was fixed at 50%. (A-B) M-Gal 10, (C-D) M-Gal 35, (E-F) M-Gal 45, (G-H) M-Gal 60, where (A,C,E,G) are LSCM images and (B,D,F,H) are DIC images.

2.3.3 Specificity of Uptake by Galactosylated Poly(methionine)

We investigated the specificity of galactosylated poly(methionine) for prostate cancer cells. Initially, we replaced the hydrophilic galactose pendant side chains with glucose, another type of sugar. For most types of cancer, cellular uptake of glucose is significantly higher compared to healthy tissue, where the glucose analogue, 2-deoxy-2(^{18}F)-fluoro-D-glucose, has been exploited for imaging of tumors[71]. The glucose is internalized through glucose transporters, where it can be used in aerobic glycolysis to generate energy for rapidly proliferating cells[72]. However, unlike most malignancies, prostate cancer is a slow growing cancer, and the rate of glycolysis and glucose uptake is low. Therefore we expected that specific uptake of glucose functionalized poly(methionine) would be limited in prostate cancer cells.

As shown in Figure 2.8, the cellular uptake was similar for the glucosylated poly(methionine) and galactosylated poly(methionine) for both short and long chain lengths. Based on these results, we hypothesized that the uptake of the galactosylated poly(methionine) was non-specific, where the galactose side chains mainly contributed to the hydrophilicity of the polypeptides.

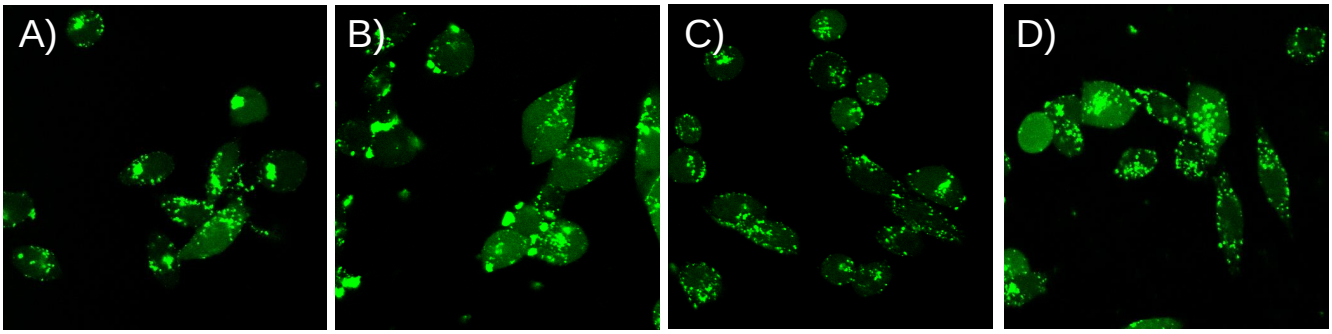

Figure 2.8. Cellular uptake of 50% functionalized (A) M-Gal 60, (B) M-Glc 60 (C) M-Gal 10 and M-Glc 10 at 0.03 mM amino acid for PC3 cells, 5 hr.

To further investigate the lack of specificity of the cellular uptake of galactosylated poly(methionine), we attempted to block specific binding of the polypeptides using excess free galactose, specifically, greater than 700-fold molar excess relative to the galactosylated poly(methionine). The excess free galactose would act to saturate the galactose binding sites, where an inhibition of cellular binding and uptake would indicate the importance of the galactose for cellular trafficking of the polypeptides (Figure 2.9).

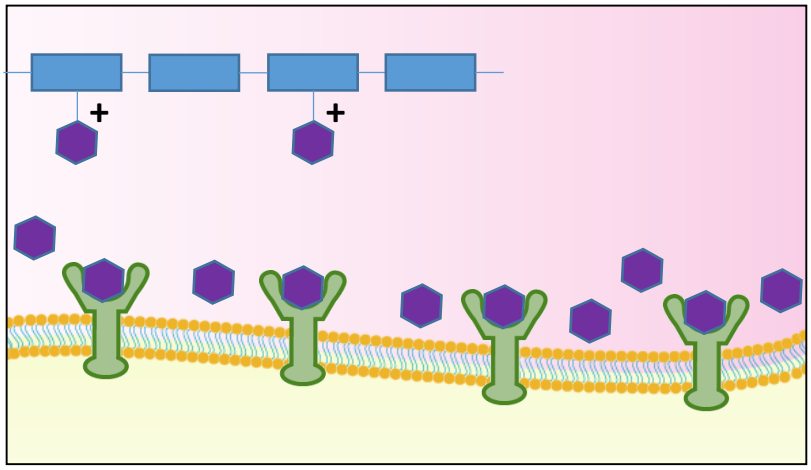

Figure 2.9. Excess free galactose (purple) could act to bind to galactose-specific binding sites on prostate cancer cells. If specific binding of the M-Gal polypeptides was specific, we would expect the binding and uptake to be limited.

The results showed that the excess galactose did not affect the uptake of galactosylated poly(methionine) (Figure 2.10). Therefore it was concluded that, rather than providing specific cellular targeting, the main contributions of the galactose pendant side chains to uptake are to increase the overall hydrophilicity and positive charge of the polypeptide. While it is possible that the M-Gal polypeptides bind to galactose binding sites on prostate cancer cells, it is not expected to be the dominant mechanism of cell entry. In the literature, peptides shown to bind specifically to Galectin-3 demonstrated significant binding with little cellular internalization[73].

This information further supports our hypothesis that other mechanisms of endocytosis likely play a key role in uptake of our polypeptides.

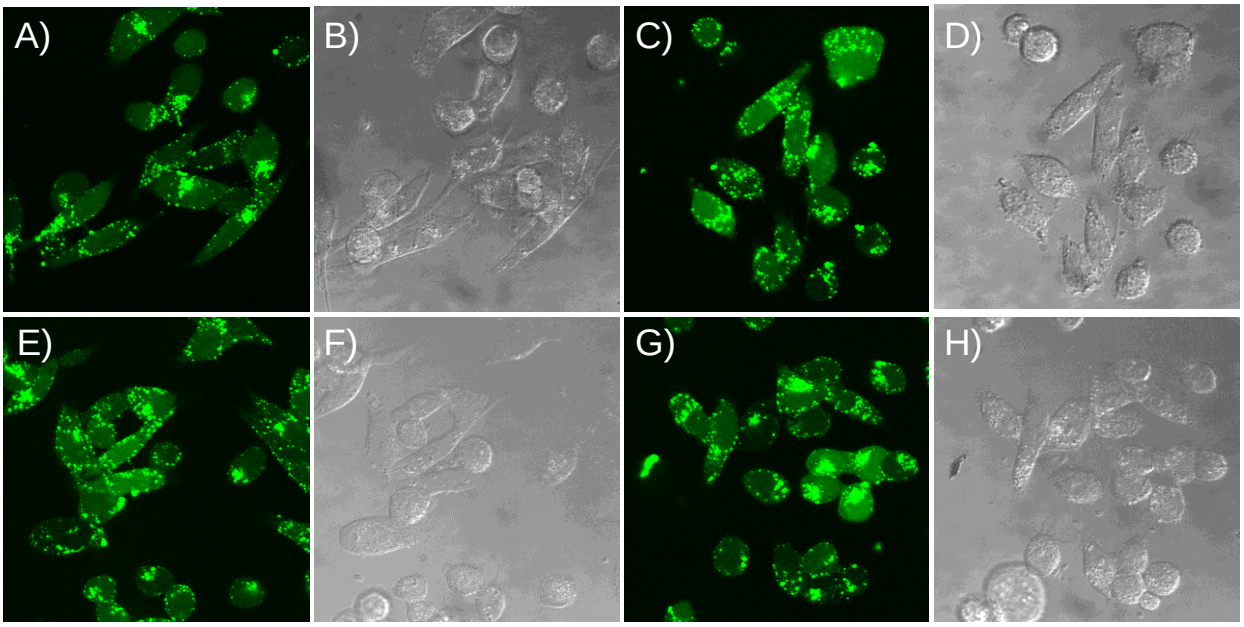

Figure 2.10. Uptake study for (A-D) M-Gal 60 in (A,B) control media and (C,D) 2 g/L excess free galactose and (E-H) M-Gal 10 in (E,F) control media and (G,H) 2 g/L excess galactose. The M-Gal 60 and M-Gal 10 were used at 0.03 mM amino acid concentrations.

2.3.4 Comparison with an Established Cell Penetrating Peptide, Nona-Arginine

Based on the high cellular uptake and low toxicity of the galactosylated poly(methionine), we wanted to evaluate its uptake ability against the established CPP, nona-arginine (R9). R9 is a short polypeptide comprised of 9 units of the basic amino acid, arginine, which was derived from the basic amino-acid rich post transduction domain of the naturally occurring HIV-transactivator of transcription (Tat) protein of the human immunodeficiency virus type 1 (HIV-1)[74]. R9 is a relatively non-toxic peptide, which can rapidly enter cells and has been used to deliver intracellular cargo. In this study, we focused on the 50% functionalized 10-mer galactosylated poly(methionine), which demonstrated low toxicity, high cellular uptake, and a degree of polymerization comparable to R9 (since 10 amino acids of the M-Gal 10 is similar to the 9 amino acids of R9). Cytotoxicity studies showed that both R9 and galactosylated poly(methionine) (M-Gal 10, 50%) were nontoxic at all concentrations tested (Figure 2.11).

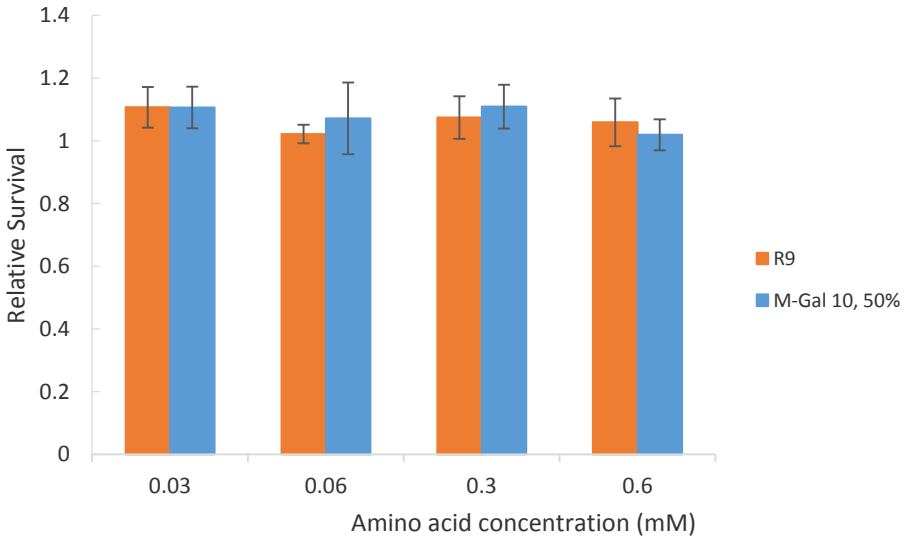

Figure 2.11. Cytotoxicity of M-Gal 10, 50% and R9, 5 h incubation.

Despite the comparable toxicity, the cellular uptake studies showed that galactosylated poly(methionine) outperformed R9 at all concentrations tested (Figure 2.12). ImageJ was used to quantify the cellular uptake based on total fluorescence per cell, and statistical analysis showed that M-Gal 10, 50% had significantly greater uptake compared to R9 (Figure 2.13). For these studies, concentration was reported in μM of polypeptide in order to compare with previous studies with R9. The exact mechanism for the enhanced uptake of our polypeptides requires more investigation. However, other polypeptides have also been shown to outperform R9, and their increase in uptake has been attributed to secondary structure, elongation of the cationic backbone chain, and incorporation of hydrophobic side chains[54,55]. The results reported in this chapter indicate that the novel glycosylated poly(methionine), which was not previously synthesized or investigated, shows promise for *in vivo* delivery of intracellular targets in the future.

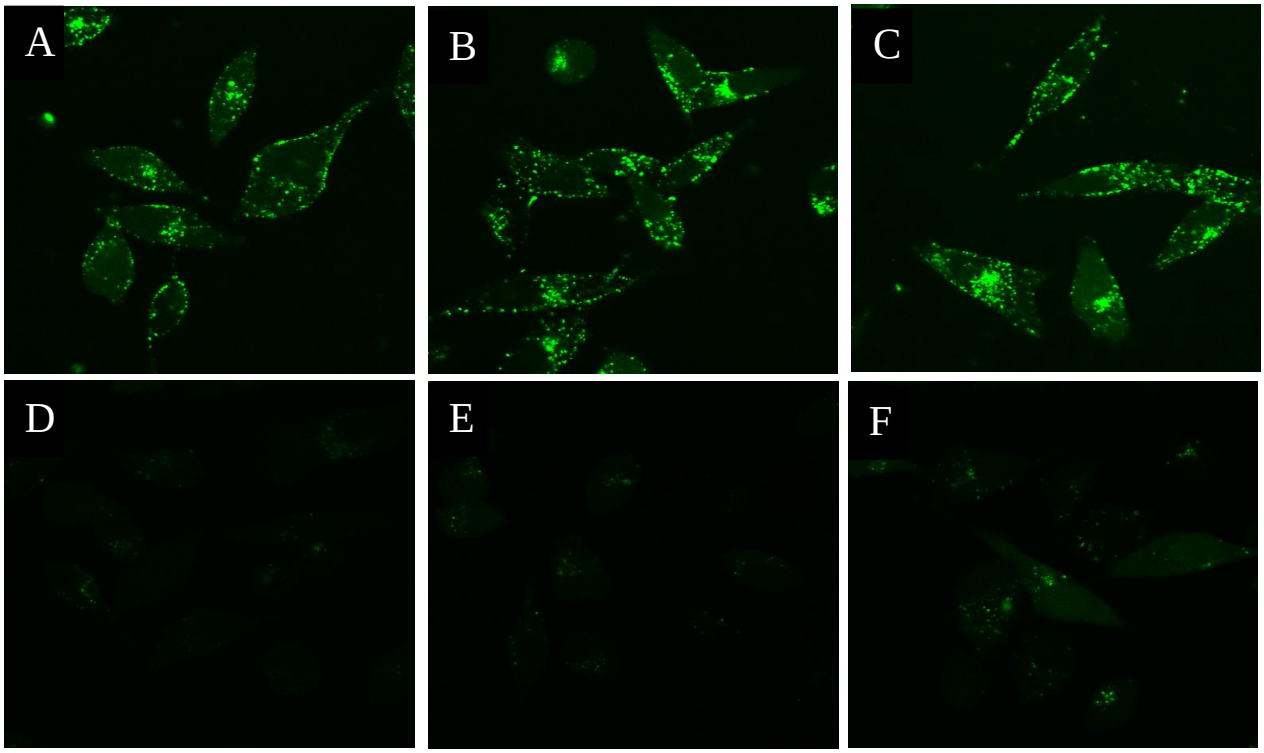

Figure 2.12. Uptake study of (A-C) M-Gal 10, 50% versus (D-F) R9 at various polypeptide concentrations (A,D) 3 µM, (B,E) 6 µM, (C,F) 12 µM.

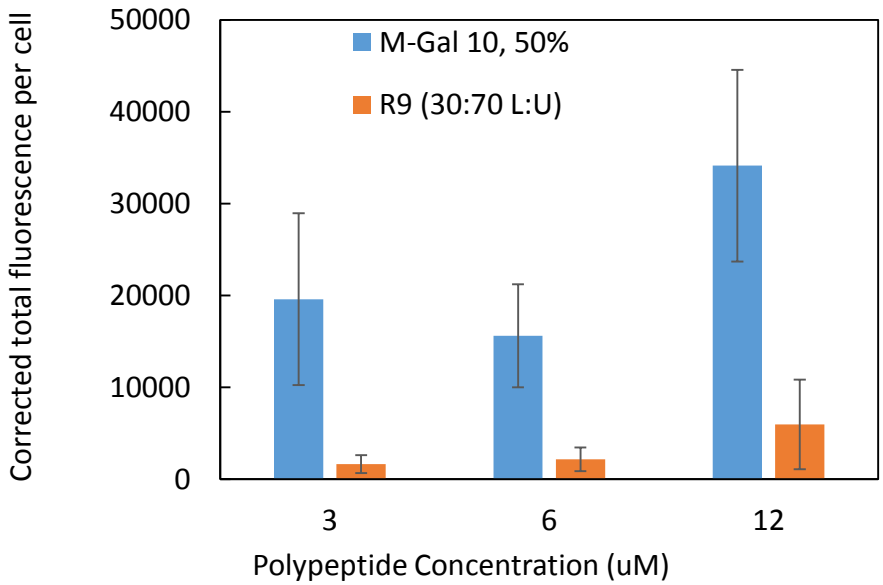

Figure 2.13. ImageJ quantification of cellular uptake of M10-Gal, 50% versus R9.

2.4 Conclusions

Here, we presented the first use of galactosylated poly(methionine) as a cell penetrating peptide. We performed cytotoxicity and fluorescent cellular uptake studies using polypeptides with a variety of properties, such as chain length and percent functionalization with galactose groups. Our 50% functionalized galactosylated poly(methionine) was found to be non-toxic to cells, and demonstrated significantly greater cellular uptake compared to a common cell penetrating peptide, nona-arginine (R9). This novel polypeptide represents a promising biomaterial for delivering anti-cancer therapies to prostate cancer cells.

3 Polypeptide-Based Gold Nanoshells for Photothermal Therapy

3.1 Photothermal Therapy

Nanosized metallic particles can convert energy absorbed from electromagnetic waves of light to heat. When a metal nanoparticle is exposed to light, the oscillating electromagnetic field induces a collective oscillation of the free electrons (conduction band electrons) of the metal[75] (Figure 3.1). The frequency of light at which the oscillation is a maximum is known as the surface plasmon resonance (SPR). The plasmon resonance of gold nanoparticles is dependent on the nanoparticle size and shape, as well as the dielectric properties of the surrounding medium that enables optical tunability by adjusting these features.

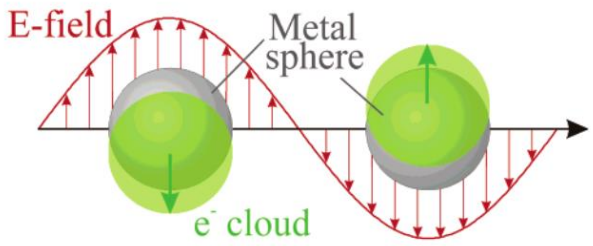

Figure 3.1. Oscillating electromagnetic field of energy can cause a collective oscillation of the conduction electrons in a metal nanoparticle[121]. (Reprinted with permission from The Optical Properties of Metal Nanoparticles: The Influence of Size, Shape, and Dielectric Environment. K. Lance Kelly, Eduardo Coronado, Lin Lin Zhao, and, and George C. Schatz*. The Journal of Physical Chemistry B 2003 107 (3), 668-677. Copyright 2003 American Chemical Society).

The SPR enhances all the radiative and nonradiative properties of the gold nanoparticles, making them excellent scatterers and absorbers of light[75–78]. Absorption of light occurs when the photon energy is dissipated due to inelastic properties, while scattering of light occurs when the photon energy causes electron oscillations in the matter which emit photon in the form of scattered light either at the same frequency as the incident light or at a shifted frequency. The

ratio of scattering to absorption is important when choosing an application for the nanoparticles. For example, high scattering of light enables cellular imaging, while a high absorption of light is required to generate thermal energy for photothermal therapy.

For photothermal therapy, it is desirable to develop gold nanoparticles that are responsive to near infrared light to minimize attenuation of the energy due to light-tissue interactions. In the near infrared region, the absorption of tissue chromophores, such as hemoglobin and water, and undesired damage to healthy tissue are minimal (Figure 3.2). In general, solid gold nanoparticles are not applicable to photothermal therapy as the tunability of the SPR band is limited to the visible region. In order to achieve an SPR band in the near infrared region, researchers have developed gold nanoparticles of different shapes and sizes, such as gold nanorods and gold nanoshells. Gold nanoshells, which are characterized by a thin layer of gold deposited onto a dielectric core, have demonstrated SPR bands ranging from UV to the mid-infrared region depending on the core diameter and shell thickness[79].

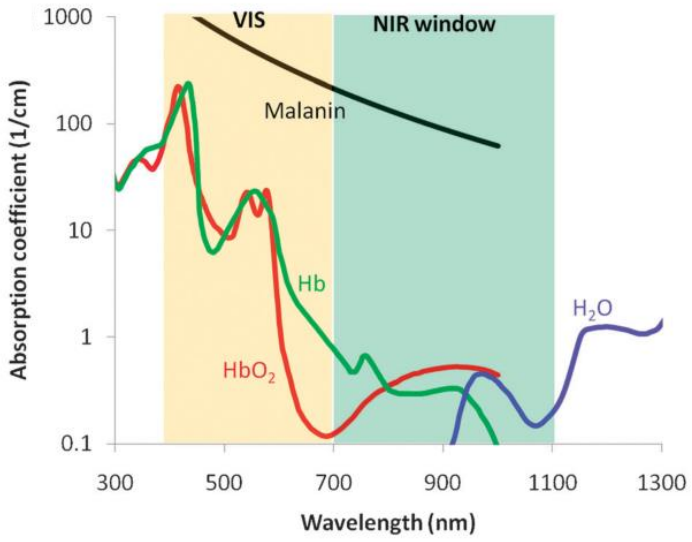

Figure 3.2. Absorption coefficient of tissue chromaphores as a function of the wavelength of light[122]. (Reprinted with permission from Thermophysical and biological responses of gold nanoparticle laser heating. Qin Z., Bischof J. Chemical Society Reviews. 2012, **41** (3), 1191-1217. Copyright 2012 Royal Society of Chemistry.)

The ability to tune the surface plasmon resonance of gold nanoshells has been described quantitatively through well-established theories, such as Mie's theory[76,79–81]. Mie's theory, which corresponds to the solution of the Maxwell equations for a dilute colloidal solution, is extended to gold nanoshells by specifying an additional boundary condition at the core-shell interface. Furthermore electronic structure methods result in exact agreement with Mie's theory for predicting the energies of the two dipole plasmon resonances as a function of the ratio of shell thickness to core radius [82]. Based on these two theories, a simple model based on an electromagnetic analogue of molecular orbital theory was developed to provide an intuitive understanding of the plasmon response of complex structures[83]. In this model, the plasmon response of the gold nanoshell is described as the interaction or "hybridization" of the fixed-frequency plasmon response supported by two simple geometries: a sphere and a hollow cavity. Due to the finite thickness of the shell, the plasmons of the inner cavity and outer sphere are able to interact with each other, where the strength of the interaction is dependent on this shell

thickness. This model explains the redshift of the plasmon resonance, where an increased hybridization of the surface plasmons of the inner and outer metallic surfaces of the shell occurs as the shell thickness is reduced.

The absorption and scattering of the gold nanoshells has been described using a Mie-based theory or numerical methods, such as the discrete dipole approximation. Researchers have developed models to predict the optical cross section of gold nanoshells, which is a measure of how well a material absorbs or scatters photons of incident light. For use in photothermal therapy, it is desirable to maximize the absorption efficiency at the desired wavelength in order to achieve maximal particle temperature and heat flux, where the absorption efficiency is the absorption cross section divided by the geometric cross section[84]. The absorption cross section is determined by parameters, such as the particle diameter, shell thickness, core materials, and surrounding medium. By varying these factors, researchers have optimized gold nanoshells for photothermal therapy using near infrared light as an external trigger.

To make gold nanoshells, a thin layer of gold is coated onto an aminated or thiolated core material. There are several methods to creating gold nanoshells. The classical method for creating gold coated silica nanoparticles is a several step process[79,81]. In this method, small gold colloids (2-3 nm) are seeded onto aminated silica nanoparticles. Subseqently, the gold shell is completed through a gold plating process, in which gold ions in solution are reduced onto the seeded gold colloids[79]. More recently, gold nanoshells have been made through a direct reduction of gold ions onto a functionalized core material using a gentle reducing agent, such as hydroxylamine, where the reaction is accelerated by the presence of gold surfaces, resulting in no new particle formation as all the Au^{3+} goes to the formation of the nanoshells[85,86]. In order to tune the surface plasmon resonance of the gold nanoshells the amount of gold added, the pH of

the solution, the core diameter, and the composition of the dielectric core material can be manipulated.

The properties of the core material, such as the dielectric constant, can affect the optical properties of the gold nanoshells, such as absorption efficiency, plasmon line width, and plasmon energies[87]. The core material of classical gold nanoshells was solid silica nanoparticles, however other materials have also been used as core materials, such as polymeric and semiconductor nanoparticle cores[79,87–89]. Furthermore, hollow core materials such as liposomes have been used, which provide additional benefits, such as the ability to encapsulate hydrophilic and hydrophobic cargo in the core and bilayer, respectively. Gold nanoshells with liposome cores have shown promise in photothermal therapy, as well as triggered release of anti-cancer drugs[86,90–92].

Polypeptide vesicles have never been used as the core material for gold nanoshells, and therefore, the work presented in this chapter is novel and significant. Polypeptide vesicles are an emerging class of biomaterials that have shown promise in delivering nucleic acids and anticancer drugs. Vesicles formed from amphiphilic polypeptides can also provide increased stability over conventional liposomes due to the formation of thicker vesicle membranes, which contributes to increased attractive interactions between the building blocks. Furthermore, polypeptides with a wide variety of chemical and physical properties can be synthesized from naturally occurring, as well as synthetic, amino acid residues using transition-metal-mediated living *N*-carboxyanhydride polymerization. Since polypeptide vesicles are made from amino acid building blocks, they have the potential to exhibit low immunogenicity and toxicity. In this thesis work, we have investigated the use of the poly(L-lysine)$_{60}$-*block*-poly(L-leucine)$_{20}$ block copolypeptide ($K_{60}L_{20}$) to form vesicles as a novel class of core material for hollow gold nanoshells.

Previously, Deming and Kamei research groups have examined the ability of the poly(L-lysine)$_{60}$-*block*-poly(L-leucine)$_{20}$ block copolypeptide ($K_{60}L_{20}$) to self-assemble into vesicular structures that could be extruded to 100-200 nm size with low polydispersity[23]. While the $K_{60}L_{20}$ vesicles were able to encapsulate hydrophilic cargo[23], use of the positively charged vesicles as a drug delivery vehicle was limited due to its high cytotoxicity. We reasoned that coating the vesicles in gold would enable use of the vesicles for photothermal therapy. We expected a reduction in toxicity for gold coated $K_{60}L_{20}$ vesicles, since gold nanoparticles are known to be nontoxic and the gold shell would mask the surface amines, which interact strongly with the net negatively charged cell membrane to induce cellular damage. To efficiently coat the $K_{60}L_{20}$ vesicles with gold, we took advantage of the abundance of amines on the vesicle surface, provided by the 60 residues of lysine in the hydrophilic block. Optimization of the gold coating allowed tunability of the surface plasmon resonance to the near infrared region. Furthermore, as predicted, the gold coated $K_{60}L_{20}$ vesicles had a reduced toxicity, demonstrated the ability to generate heat after exposure to an 808 nm laser, and laser-induced cytotoxicity for *in vitro* photothermal therapy experiments.

3.2 Materials and Methods

3.2.1 Materials

PC3 cell lines were obtained from the American Type Culture Collection (Manassas, Virginia). Roswell Park Memorial Institute (RPMI) 1640 cell culture media, penicillin-streptomycin (P/S), sodium pyruvate (NaPyr), phosphate buffered saline (PBS), and 0.25% trypsin with ethylenediaminetetraacetic acid (EDTA) were purchased from Invitrogen (Carlsbad, California). Fetal bovine serum (FBS) was obtained from Hyclone (Waltham, Massachusetts).

96-well plates were purchased from Sigma-Aldrich (St. Louis, MO). The MTS cell proliferation assay kit was purchased from Promega (Madison, Wisconsin). The Bradford reagent was obtained from Bio-Rad (Hercules, California).

3.2.2 Synthesis of Block Copolypolypeptides

The $K_{60}L_{20}$ block copolypeptide was synthesized using the transition-metal-initiated living *N*-carboxyanhydride polymerization technique as previously described[23]. The resulting copolypeptide was freeze-dried. The $K_{60}L_{20}$ polypeptide was processed into vesicles using a modification of a method previously reported[23]. Specifically, the vesicles were formed by first dissolving 10 mg of polypeptide in 1 mL of a 1:1 mixture between THF and sterile Milli-Q water. Subsequently, 250 µL of THF was added four times to yield a final polypeptide concentration of 0.5 % w/v. The mixture was placed in a dialysis bag (MWCO = 1,000 Da), and dialyzed against sterile Milli-Q water overnight to remove the THF, where the sterile Milli-Q water was changed every hour for the first 4 hrs. The resulting vesicles were extruded through a series of polycarbonate membrane with 1000 nm, 400 nm, and 200 nm pores (in that order) to obtain uniformly sized vesicles. The sizes of the vesicles and their distribution were analyzed with dynamic light scattering (DLS), and the Bradford assay was performed to quantify the final concentration of the polypeptide vesicles according to the manufacture supplied instructions, using the predialyzed samples as the standard.

3.2.3 Coating of Gold Nanoshells

A 5.4 mL solution of polypeptide vesicles (1.5 mg) was adjusted to pH 7 using 7% ammonium hydroxide (Sigma-Aldrich, St. Louis, MO). Hydroxylamine hydrochloride (Sigma-Aldrich, St. Louis, MO) was added in excess (500 µL of a 0.2 M solution) followed by 800 µL

of a 0.5% gold (III) chloride solution (Sigma-Aldrich, St. Louis, MO) in 50 µL aliquots. The pH was determined to be critical in the gold coating process, so the pH was adjusted as needed to maintain a pH of 7 throughout the coating process.

3.2.4 Characterization of Gold Nanoshells

Size and zeta potential measurements were performed on $K_{60}L_{20}$ vesicles with the Malvern Zetasizer Nano ZS model Zen 3600 (Malvern Instruments Inc, Westborough, Massachusetts). The gold nanoshells were also imaged, and the size was measured using transmission electron microscopy (TEM) with the T20 iCorr (FEI) High-Resolution CryoEM from the FEI Tecnai G2 Family with the help of Dr. Hong Zhao's group. The extinction profile of the gold nanoshells was measured to verify the strong surface plasmon resonance in the near infrared region using a UV-visible spectrophotometer (Thermo Scientific BioMate 3S) over a range of wavelengths from 400 to 1000 nm.

3.2.5 Cytotoxicity of Gold Nanoshells

PC3 cells were seeded onto 96 well plates at 88,000 cells/cm^2. Various concentrations of gold nanoshells in blank RPMI media (no fetal bovine serum or penicillin and streptomycin) were incubated with triplicate wells of PC3 cells for 5 h. After the 5 h incubation period, the medium was aspirated and fresh medium containing 20% MTS reagent solution (MTS cell proliferation assay; CellTiter 96® AQ_{ueous} Non-Radioactive Cell Proliferation Assay) was added to the cells. The cells were then incubated in a humidified CO_2 incubator at 37°C for 1 h, and the absorbance was measured at 490 nm.

3.2.6 Measuring Heat Generation

Gold nanoshells (3.5 mg/mL in ddH2O) were irradiated with 200 mW laser diode, 808 nm (ThorLabs, Inc., Newton, NJ) for 10 minutes, where the laser set-up was designed by Dr. Grundfest's laboratory. The temperature was measured at desired time points using a thermocouple.

3.2.7 Photothermal Therapy

PC3 cells were seeded onto 96 well plates at 88,000 cell/cm^2. Gold nanoshells (1 mg/mL) were incubated with PC3 prostate cancer cells for 2 h in serum-free media. Cells were then irradiated with 808 nm laser diode (200 mW) for 10 minutes. A Live/Dead Stain Kit (calcein AM and ethidium homodimer, Molecular Probes, CA, USA) was used to evaluate the viability of the cells. Cells were examined using fluorescent microscopy.

3.3 Results and Discussion

3.3.1 Making Polypeptide-Based Gold Nanoshells

Typically, aminated core materials have been used, since amines can form dative bonds with gold, enabling the formation of a gold coating. Based on the success of such aminated core materials, we chose to develop the polypeptide-based gold nanoshell using the $K_{60}L_{20}$ vesicles, which have an abundance of lysines on the surfaces. Using hydroxylamine to reduce the gold ions onto the surface of the vesicles, the $K_{60}L_{20}$ gold nanoshells were created (Figure 3.3).

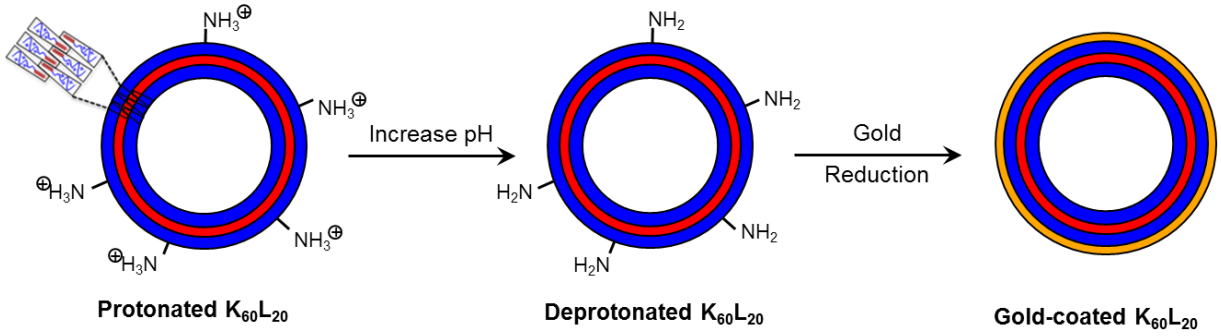

Figure 3.3. Schematic for making polypeptide-based gold nanoshells.

The surface plasmon resonance (SPR) of gold nanoshells can be tuned to the near infrared region by adjusting the ratio of the shell thickness to vesicle diameter. The diameter of the poly(L-lysine)$_{60}$-*block*-poly(L-leucine)$_{20}$ block copolypeptide ($K_{60}L_{20}$) vesicles was fixed at approximately 200 nm by serial extrusion through polycarbonate membranes. Therefore, we focused on adjusting the thickness of the gold coating to tune the SPR to the near infrared region. Previous studies have shown that reducing the shell thickness results in a red-shift of the spectral peak to longer wavelengths. Optimizing the pH of the solution to 7 during gold coating, we achieved gold that were responsive in the near infrared region (Figure 3.4). As shown in the figure, the $K_{60}L_{20}$ gold nanoshells show a broad absorption band between ~500 to 1000 nm, where strong absorption and/or scattering of light was observed at 808 nm, indicating that light in the near infrared range could be used to trigger a therapeutic response.

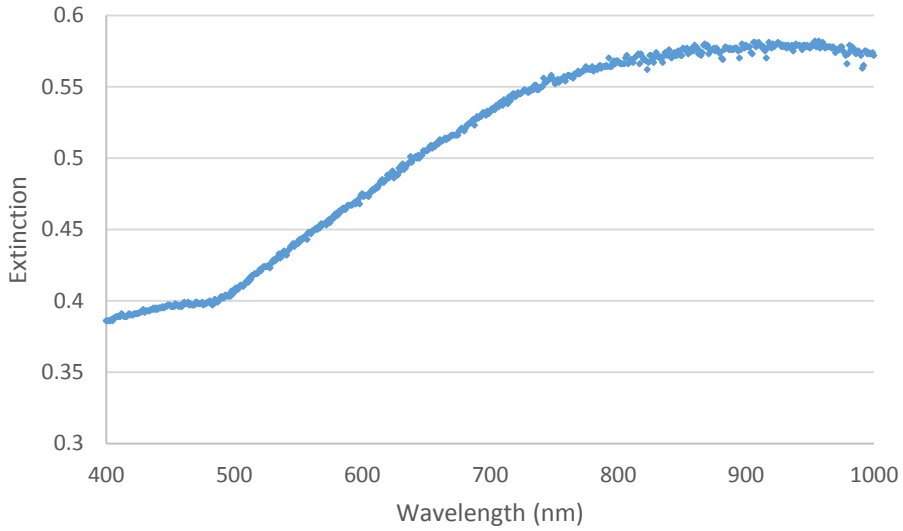

Figure 3.4. Visible-near infrared absorption spectra of polypeptide-based gold nanoshells, where the pH of the gold coating solution was set to 7. Extinction is the sum of the absorption and scattering of light.

Based on the dynamic light scattering (DLS) measurements, the gold nanoshells were relatively monodisperse and within the size range for passive targeting of tumor tissue (Table 3.1). Previous research has shown that nanoparticles with diameters in the range of 60-400 nm can accumulate within tumor tissue due to the leaky vasculature and poor lymphatic drainage at the tumor site, also known as the enhanced permeability and retention (EPR) effect[3]. Transmission electron microscopy (TEM) images show spherical gold nanoshells, where increasing the amount of gold added during the coating procedure results in a smoother and more spherical shape (Figure 3.5). The diameters observed with TEM were also consistent with those measured with DLS. Furthermore, the zeta potential, which is the potential at the no slip boundary of the nanoparticle, indicated that the gold nanoshells retained their positive surface charge, which should enable them to interact favorably with the net negatively charged cell membrane.

Table 3.1. Characterization of polypeptide-based gold nanoshells

$K_{60}L_{20}$ Vesicles	Size (nm)	Polydispersity Index (PDI)	Zeta Potential (mV)
Uncoated	232 ± 15	0.255 ± 0.058	14.3 ± 1.2*
Coated	359*	0.393*	29.2 ± 3.1*

* For these parameters N =1, otherwise N > 3

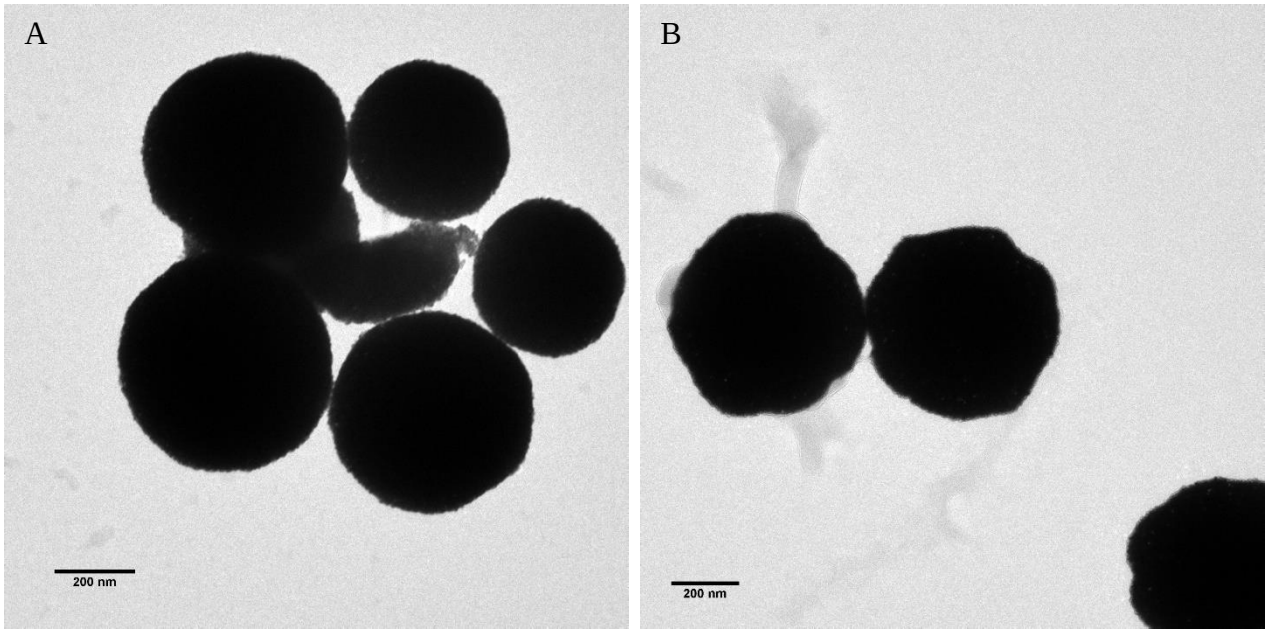

Figure 3.5. TEM images of $K_{60}L_{20}$ gold nanoshells with (A) complete gold coating and (B) partial gold coating, created by adding less gold during gold coating of the $K_{60}L_{20}$ vesicles.

Due to the strong cellular membrane interaction, positively charged carriers can be highly cytotoxic. Similarly, previous attempts to use the positively charged, uncoated $K_{60}L_{20}$ vesicles for drug delivery had been limited due to a dose dependent toxicity. Gold nanoparticles, on the other hand, are known to be relatively inert and non-toxic *in vitro* and *in vivo*, and we found that the gold coating reduced the toxicity of the vesicles (Figure 3.6). It is hypothesized that the addition of the gold coating disguised the abundance of lysine amino acids, resulting in a reduction of the overall toxicity.

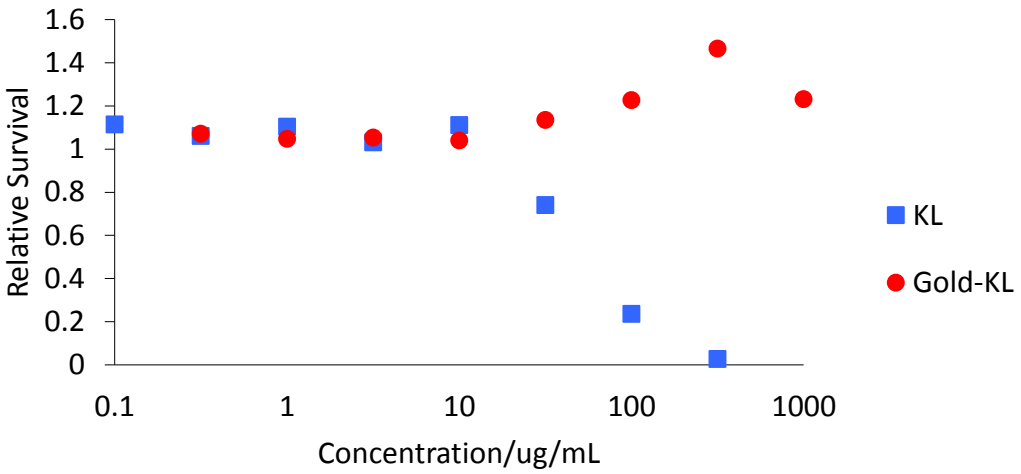

Figure 3.6. Cytotoxicity for uncoated $K_{60}L_{20}$ vesicles (blue) and $K_{60}L_{20}$ gold nanoshells (red).

3.3.2 Measuring Heat Generation from Gold Nanoshells

For ablation of tumor tissue in photothermal therapy, near infrared light that maximally overlaps with the surface plasmon resonance of the gold nanoshells is used as an external trigger. The energy absorbed by the gold nanoshells is dissipated to the surrounding environment as heat. Research has shown that cancer cells are more sensitive to temperature increases, compared to normal cells due to the more harsh microenvironment of low partial pressures of oxygen and acidic pH conditions, where temperatures above 42°C effectively ablate tumor tissue. The aqueous solution containing $K_{60}L_{20}$ gold nanoshells showed a 30°C temperature increase over a 10 min exposure to the 808 nm (200 mW) continuous diode laser, while water alone showed no temperature change (Figure 3.7). These results show that our polypeptide-based gold nanoshells show promise as a triggered, local photothermal therapy.

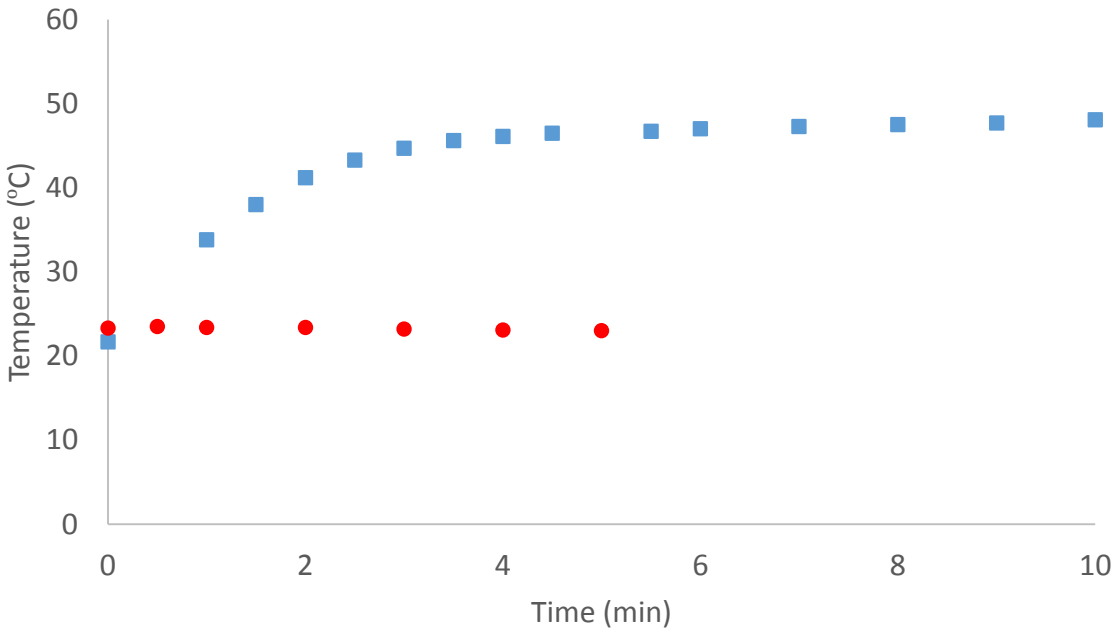

Figure 3.7. The temperature as a function of time for water (red circles) and gold nanoshells in water (blue squares) with exposure to a 200 mW laser diode, 808 nm.

3.3.3 Photothermal Therapy Using Polypeptide-Based Gold Nanoshells

Hyperthermia treatment of cancer cells uses elevated temperatures above 42ºC, which can denature proteins and disrupt cell membranes[93,94]. Gold nanoshells can provide localized heating to the tumor site in response to near infrared laser irradiation. To investigate the use of the $K_{60}L_{20}$ gold nanoshells for *in vitro* cytotoxicity, we incubated the gold nanoshells with prostate cancer cells for 2 h prior to irradiation with the near infrared laser. The results demonstrate that combination of $K_{60}L_{20}$ gold nanoshells and exposure to the near infrared laser results in cytotoxicity of the cells, where the green and red stain indicate live and dead cells, respectively (Figure 3.8 A, B). Furthermore, the cell death is limited to the region of cells irradiated by the laser. Additionally, no similar region is observed in cells with $K_{60}L_{20}$ gold nanoshells, which have not been irradiated (Figures 3.8 C, D), or when cells are irradiated with the laser in the absence of gold nanoshells (Figure 3.8 E, F). These promising *in vitro* results indicate that the $K_{60}L_{20}$ gold nanoshells can generate sufficient heat under near infrared irradiation to cause localized cytotoxicity of cancer cells.

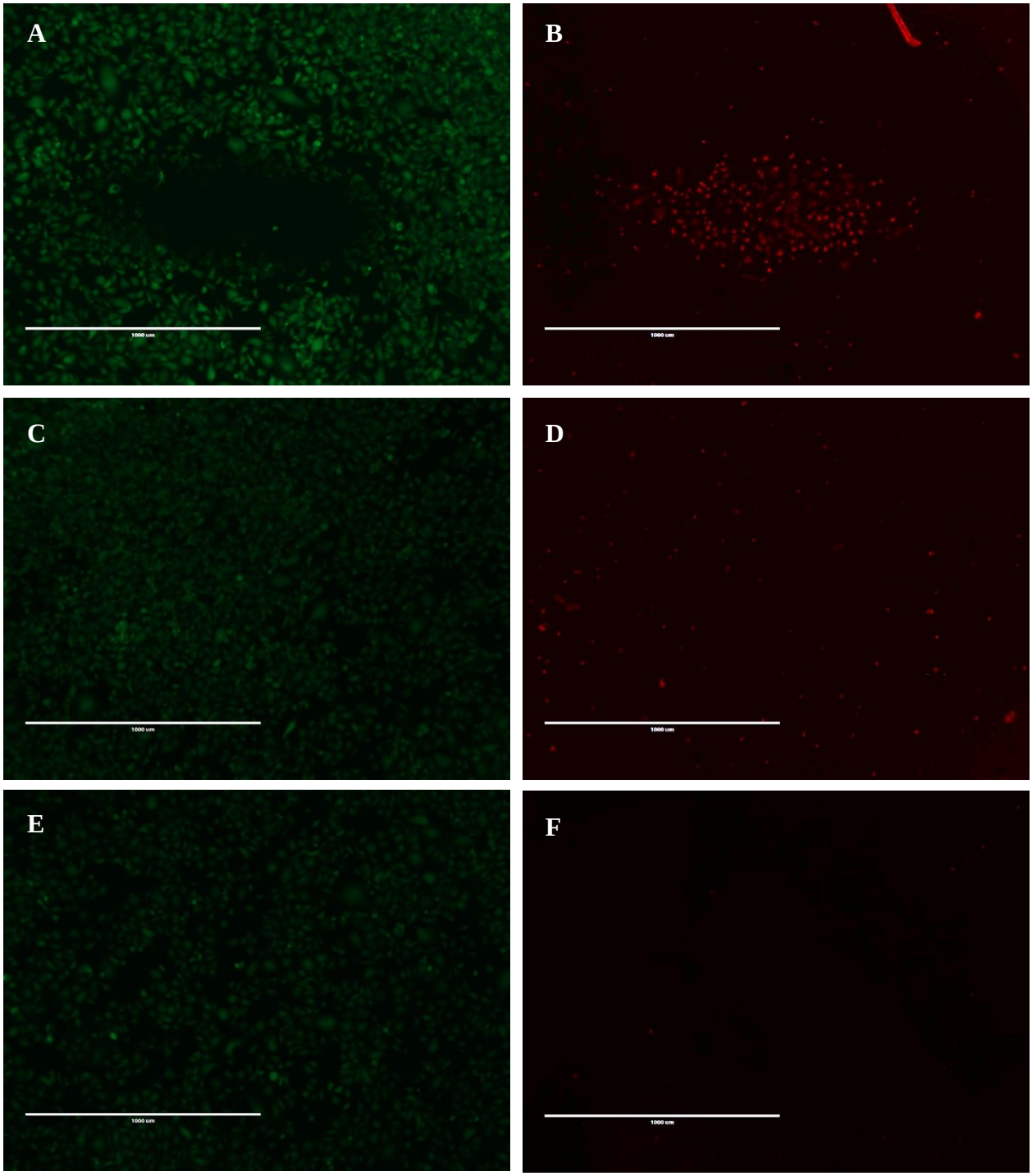

Figure 3.8. Cytotoxicity of (A, B) $K_{60}L_{20}$ gold nanoshells irradiated with 200 mW, 808 nm laser diode, (C, D) $K_{60}L_{20}$ gold nanoshells only (not exposed to the laser), and (E, F) cells only irradiated with the near infrared laser. Live cells are stained green (A, C, E) and dead cells are stained red (B, D, F).

3.4 Conclusions

Although these gold-coated polypeptide vesicles showed promise in phothermal therapy applications, their sizes were on the high end of the range of diameters associated with the enhanced permeability and retention (EPR) effect, which describes how nanoparticles accumulate in solid tumor tissue. We therefore focused on reducing the sizes of these gold nanoshells in the following chapter.

4 Optimization of the Polypeptide-Based Gold Nanoshells

While the $K_{60}L_{20}$ gold nanoshells investigated in Chapter 3 demonstrated potential as photothermal therapy agents, they were determined to be relatively large compared to other nanoshells in the literature. In this chapter, we optimized the protocol to generate gold nanoshells that are in the size range of 150 nm. The procedures used to reduce the overall size of the gold nanoshells, included (1) reducing the size of the $K_{60}L_{20}$ vesicle core, and (2) reducing the amount of gold added to the vesicle core (Figure 4.1). Similar to the previous sections, the optimized gold nanoshells were successfully used as a photothermal therapy agent *in vitro* for the localized and specific laser-induced toxicity of prostate cancer cells.

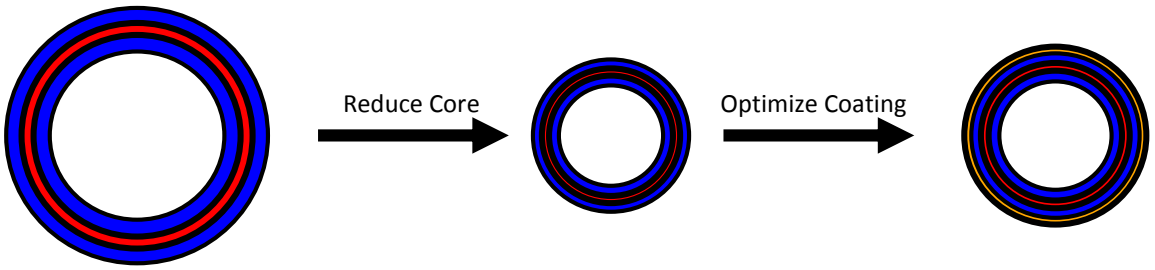

Figure 4.1. Approaches to reduce polypeptide-based gold nanoshell size.

4.1 Materials and Methods

Unless otherwise stated, the materials and methods are the same as described in Section 3.2

4.1.1 Optimized $K_{60}L_{20}$ Processing

The vesicles were formed by first dissolving 10 mg of polypeptide in 1 mL of a 15% tetrahydrofuran (THF) in sterile Milli-Q water. Subsequently, another 1 mL of a 15% THF solution was added to yield a final polypeptide concentration of 0.5 % w/v. The mixture was

placed in a dialysis bag (MWCO = 8,000 Da), and dialyzed against sterile Milli-Q water overnight to remove the THF, where the sterile Milli-Q water was changed every hour for the first 4 hrs. The resulting vesicles were extruded through a series of polycarbonate membrane with 1000 nm, 400 nm, 200 nm, and 100 nm pores (in that order) to obtain uniformly sized vesicles.

4.1.2 Optimized Gold Coating Procedure

A 2.7 mL solution of polypeptide vesicles (0.782 mg) was adjusted to pH 7 using 7% ammonium hydroxide (Sigma-Aldrich, St. Louis, MO). Hydroxylamine hydrochloride (Sigma-Aldrich, St. Louis, MO) was added in excess (500 µL of a 0.2 M solution) followed by 90 µL of a 0.5% gold (III) chloride solution (Sigma-Aldrich, St. Louis, MO) in two 45 µL aliquots. The solution was allowed to spin for 2 hrs, and then 108 µL of 0.5% gold (III) chloride solution was added in two 54 µL aliquots. The solution was allowed to spin overnight, and the gold coated vesicles were recovered by centrifugation at 9,000 rcf for 10 minutes. As previously determined, the pH was critical in the gold coating process, so the pH was adjusted as needed to maintain a pH of 7 throughout the coating process.

4.1.3 Characterization of Gold Nanoshell Concentration

To determine the concentration of gold nanoshells, the volume of gold per nanoshell was first calculated based on the thickness of the gold shell. This volume was then converted to mass of gold per particle using the density of gold (19.3 g/cm^3). Next, ICP-MS was used to measure the total amount of gold in the solution. Since we evaluated the mass per particle, the concentration of gold nanoshells in solution could be determined.

4.1.4 Cytotoxicity of Gold Nanoshells

To assess the cytotoxicity of the gold nanoshells, the MTS cell proliferation assay (CellTiter 96® AQ_{ueous} Non-Radioactive Cell Proliferation Assay) was performed with PC3 prostate cancer cells. PC3 cells were seeded onto 96 well plates at 88,000 cell/cm^2. Various concentrations of gold nanoshells were incubated with triplicate wells of cells for 5 h. After the 5 h incubation period, the medium was aspirated and fresh medium containing a 20% MTS reagent solution was added to the cells. The cells were then incubated in a humidified CO_2 incubator at 37°C for 1 h, and the absorbance was measured at 490 nm.

4.1.5 Measuring Heat Generation

Gold nanoshells (absorbance at 808 nm = 0.6, concentration = $1.1x10^8$ particles/mL) were irradiated with a 200 mW laser diode, 808 nm (ThorLabs, Inc., Newton, NJ) for 10 minutes. The temperature was measured at desired time points using a thermocouple (OMEGA Engineering INC., Stamford, CT).

4.1.6 Photothermal Therapy

PC3 cells were seeded onto 96 well plates at 88,000 cells/cm^2. Gold nanoshells (absorbance at 808 nm = 0.6, concentration = $1.1x10^8$ particles/mL) were incubated with PC3 prostate cancer cells for 2 h in serum-free media. Cells were then irradiated with an 808 nm laser diode (200 mW) for 10 minutes. A Live/Dead Stain Kit (calcein AM and ethidium homodimer, Molecular Probes, CA, USA) was then used to evaluate the viability of the cells. Cells were examined using fluorescent microscopy with EVOS fl Digital Inverted Fluorescence Microscope (Advanced Microscopy Group/Life Technologies, Grand Island, NY).

4.2 Results and Discussion

4.2.1 Reduction of the $K_{60}L_{20}$ Gold Nanoshell Diameter

To reduce the vesicle core, we focused first on altering the vesicle processing procedure. In the dual solvent processing method, the organic solvent acts to solubilize both the hydrophobic and hydrophilic blocks, while the aqueous solvent only solubilizes the hydrophilic block. In previous work with the polypeptide vesicles, reducing the ratio of THF:water has been shown to reduce the vesicle size. Reducing the THF is expected to reduce the amount of swelling of the hydrophobic region, which can decrease the radius of curvature of the vesicle. To understand this effect, consider that individual polypeptides take on a truncated cone shape prior to assembling into a vesicle supermolecular structure, as shown in Figure 4.2, where the red alpha helical structure represents the hydrophobic poly(leucine) block and the blue random coil structure represents the hydrophilic poly(lysine) block. By reducing the volume of the hydrophobic tail without significantly altering the area of the hydrophilic head, the polypeptide can take on a less truncated cone shape, which can self-assemble into smaller vesicles (Figure 4.3). After processing the vesicles with the new ratio of THF:water, the vesicle size was further reduced using an extrusion method to pass the vesicles through a series of nanosized pores, including a 100 nm pore size. As shown in Table 4.1, this new procedure significantly reduced the size of the $K_{60}L_{20}$ vesicles to 122 nm, while maintaining a relatively low polydispersity index.

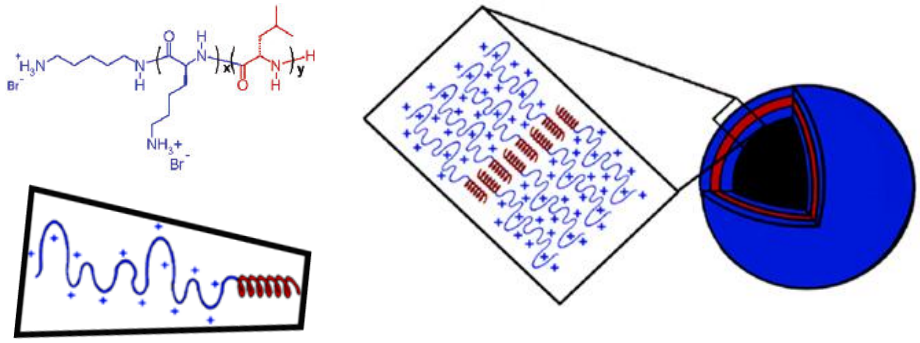

Figure 4.2. The random coil formation of the hydrophilic block and the alpha helical conformation of the hydrophilic block of the $K_{60}L_{20}$ polypeptides give the polypeptides a truncated cone shape, which can self-assemble into a vesicle structure[23]. The poly(lysine) block is represented by the blue random coil, and the poly(leucine) block is shown in red. (Reprinted with permission from Charged Polypeptide Vesicles with Controllable Diameter. Eric P. Holowka, Darrin J. Pochan, and Timothy J. Deming, Journal of the American Chemical Society 2005 127 (35), 12423-12428. Copyright 2005 American Chemical Society).

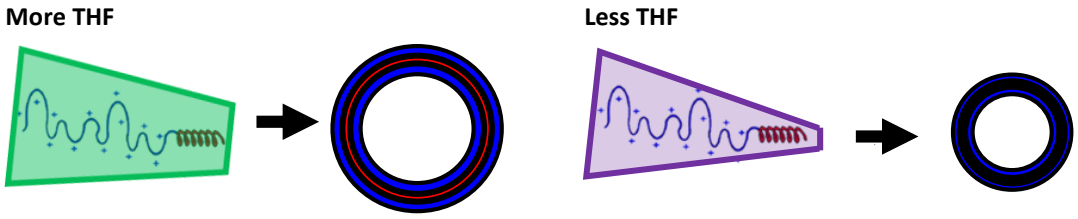

Figure 4.3. Effect of reducing the amount of THF in the processing of the polypeptides, which reduces the volume of the hydrophobic leucine segment, resulting in a smaller vesicle core.

Table 4.1. Characterization of the optimized $K_{60}L_{20}$ gold nanoshells.

$K_{60}L_{20}$ Vesicles	Size (nm)	Polydispersity Index (PDI)
Uncoated	122 ± 1	0.25 ± 0.01
Coated	150 ± 2	0.13 ± 0.02

Next, we modified the gold coating procedure to reduce the amount of gold added to the vesicle core. For this optimization, we reduced the amount of gold to achieve a gold nanoshell size of 150 nm (Table 4.1), while maintaining a low polydispersity index. This size range is ideal for passive targeting to prostate cancer tumors through the enhanced permeability and retention effect, as discussed previously. Transmission electron microscopy (TEM) and scanning electron microscopy (SEM) images show spherical gold nanoshells (Figure 4.4), where the diameter of the gold nanoshells observed with TEM were also consistent with those measured with DLS. Furthermore, the zeta potential of the gold nanoshells, which is the potential at the no slip boundary of the nanoparticle, is +50 mV, indicating that the gold nanoshells retained their positive surface charge, which should enable them to interact favorably with the net negatively charged cell membrane.

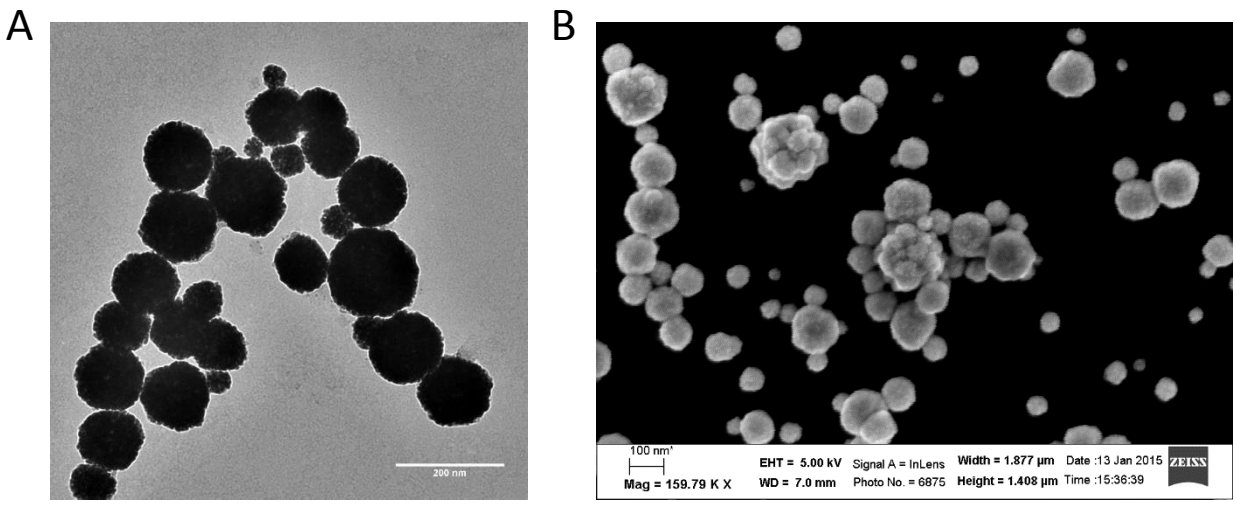

Figure 4.4. Images of the optimized $K_{60}L_{20}$ gold nanoshells, where A) transition electron microscopy (TEM) scale bar = 200 nm, and B) scanning electron microscopy (SEM) image scale bar = 100 nm.

Furthermore, the optimization of the gold coating procedure resulted in gold nanoshells with a distinct peak extinction in the near infrared region (Figure 4.5). The extinction profile for the larger gold nanoshells utilized in Sections 3.1-3.3 demonstrated a plateau shape, with an increased extinction in the near infrared region. The difference in the extinction profile may be attributed to multipole oscillations, which has been shown to be important in gold nanoshells with larger diameters. Based on the extinction profile for the optimized gold nanoshells, we expected them to be responsive to near infrared light for use as a photothermal therapy agent.

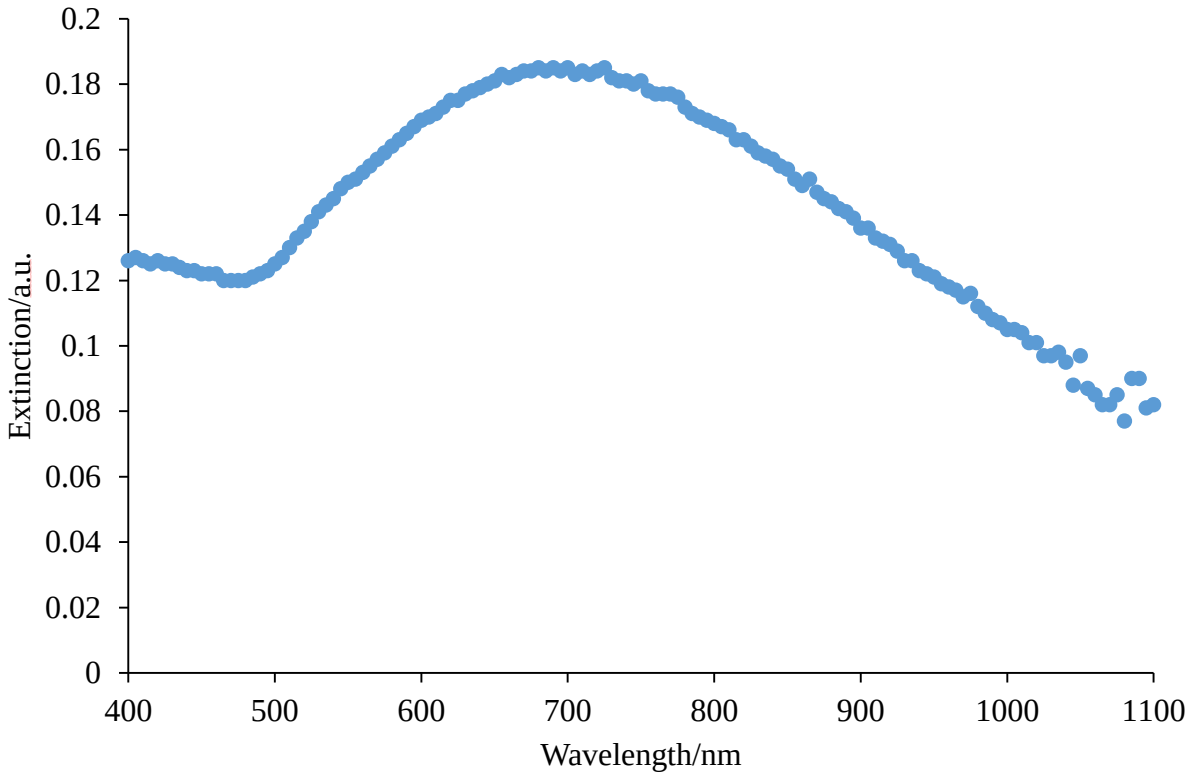

Figure 4.5. Visible-near infrared absorption spectra of the optimized polypeptide-based gold nanoshells. Extinction is the sum of the absorption and scattering of light in absorbance units (a.u.).

4.2.2 Use of the Optimized Gold Nanoshells for Photothermal Therapy

To determine the success of the optimized gold nanoshells, we first examined the heat generation when exposed to a near infrared laser at 808 nm wavelength. As demonstrated previously, the gold nanoshells generated significant amount of heat to cause laser-induced cell death (Figure 4.6), while water alone did not show any temperature increase when exposed to the near infrared laser.

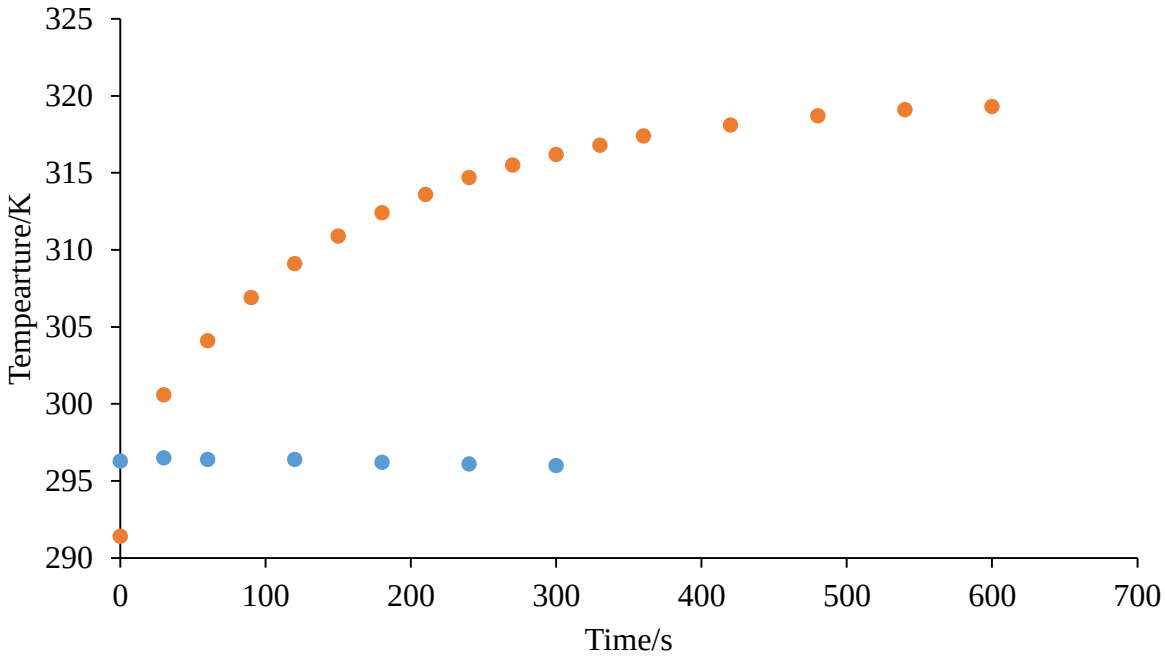

Figure 4.6. The temperature as a function of time for gold nanoshells in water with exposure to a 200 mW laser diode, 808 nm. Gold nanoshells are shown in orange and water only is shown in blue.

Next, the optimized gold nanoshells were tested as photothermal therapy agents *in vitro* with PC3 prostate cancer cells. As shown in Figure 4.7, the optimized gold nanoshells demonstrate localized laser-induced cytotoxicity (A, B), while laser alone shows no toxicity (C,

D). The gold nanoshells alone are relatively nontoxic to cells, as demonstrated by the lack of toxicity in the region outside laser irradiation in Figure 4.7 A, B, and further confirmed by a 5 hr cytotoxicity study with gold nanoshells alone (Figure 4.8). This result supports the potential of the polypeptide-based gold nanoshells for use as a photothermal therapy agent.

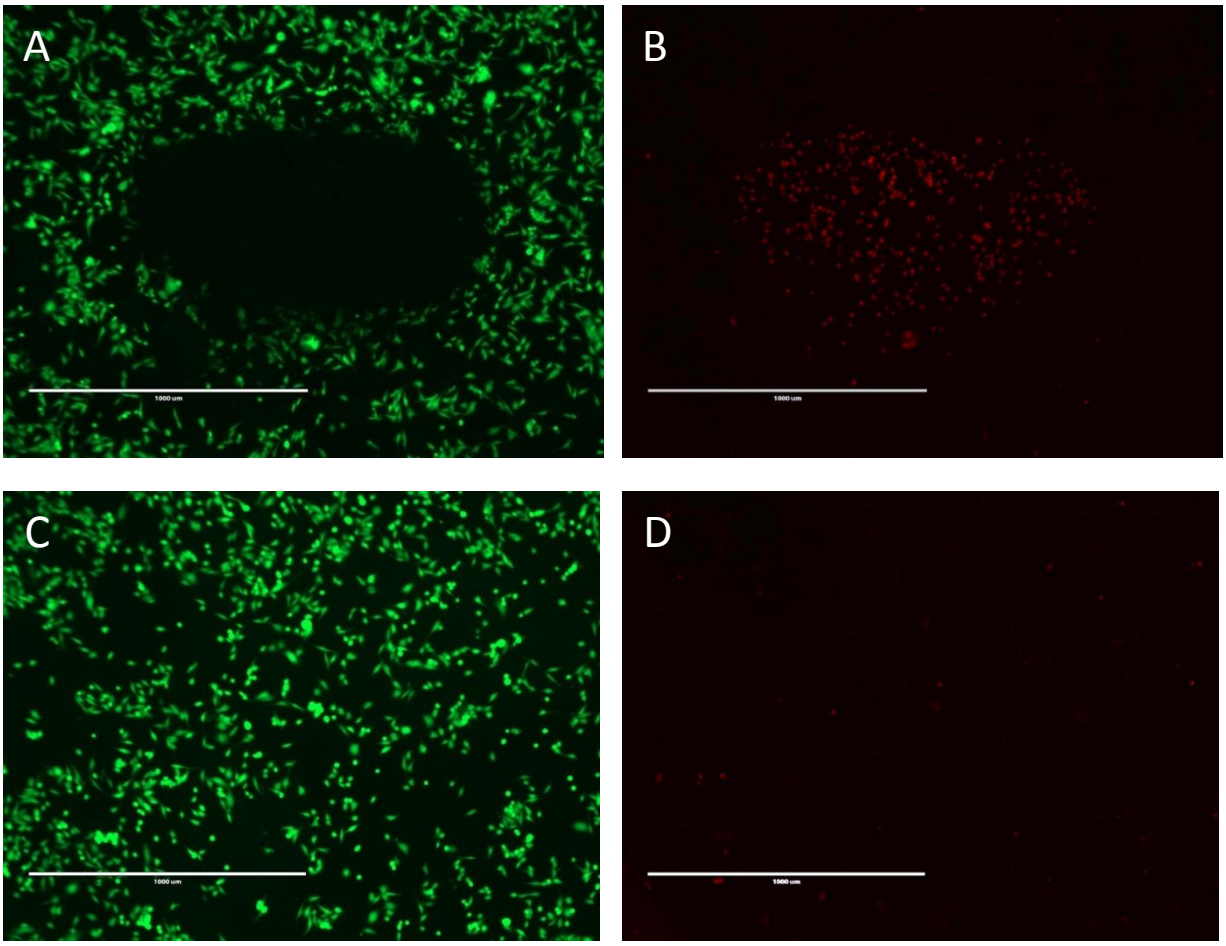

Figure 4.7. Cytotoxicity of (A, B) $K_{60}L_{20}$ gold nanoshells irradiated with 200 mW, 808 nm laser diode, (C, D) cells only irradiated with the near infrared laser. Live cells are stained green (A, C) and dead cells are stained red (B, D). Scale bar = 1 mm.

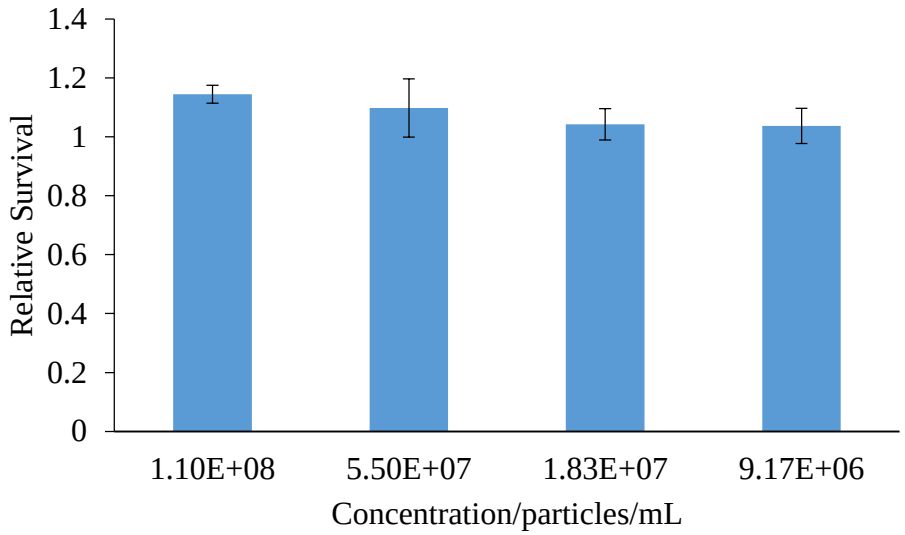

Figure 4.8. Cytotoxicity of $K_{60}L_{20}$ gold nanoshells after 5 hr incubation with PC3 cells.

4.3 Conclusions

This work presents the first use of block copolypeptide vesicles as the core material for gold nanoshells. The positively charged $K_{60}L_{20}$ vesicles were coated with a thin layer of gold, and generated significant heat in response to near infrared light. Furthermore, *in vitro* studies demonstrated laser-induced cytotoxicity for the gold nanoshells. Gold nanoshells made from block copolypeptide vesicles have several advantages as the core material, as they are made of amino acid residues, have been shown to be biocompatible and stable under a variety of biological conditions, and also have the potential to be loaded with anticancer drugs for controlled, laser-induced drug release, for a combination photothermal/chemotherapy treatment. As discussed in Chapter 6, we will investigate the use of targeting ligands to provide specificity to prostate cancer cells, which have been shown to lower the required dosage and power density, as well as increase the efficacy of the gold nanoshells.

5 Mathematical Modeling of the Heat Transfer Associated with the $K_{60}L_{20}$ Gold Nanoshells

To gain a better understanding of our $K_{60}L_{20}$ gold nanoshells in the context of photothermal therapy, we developed a comprehensive mathematical model for heat transfer. Such a model can be used in the future to determine which parameters can be manipulated to improve heat generation, and therefore, the destruction of tumors. The goal of this chapter was to develop rigorous mathematical models that were solved using numerical methods in the MATLAB programming language to predict the increase in temperature observed in our *in vitro* laser irradiation experiments (Figure 5.1).

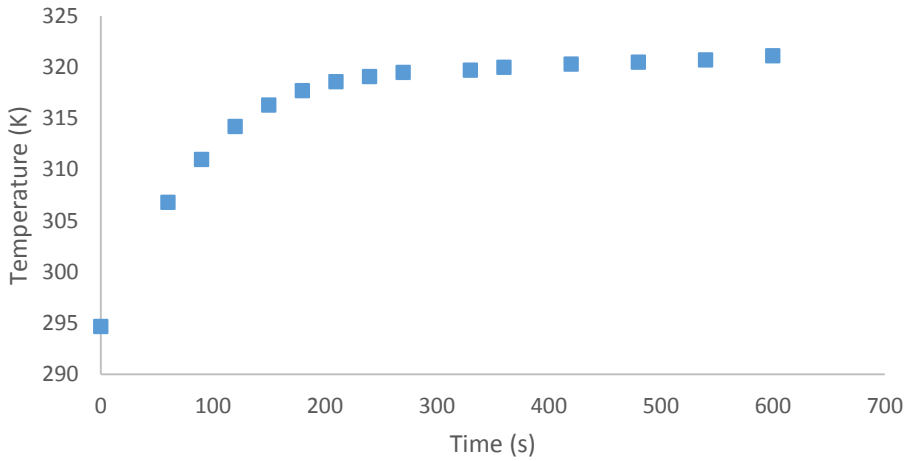

Figure 5.1. Modified from Figure 4.6 as temperature is now in Kelvins and time is in seconds. The temperature as a function of gold nanoshells in water with exposure to a 200 mW laser diode, 808 nm.

The heat generation by the gold nanoshells is a result of their strong absorbance of photons in the near infrared region, and subsequent conversion of the energy to heat. Several factors can

affect the heat generation of gold nanoshells, including the diameter of the gold nanoshell (which can affect the optical properties, such as absorption cross section and efficiency), gold nanoshell concentration, and laser power. Researchers have developed quantitative models to predict temperatures attained within well plates, cells *in vitro*, mock tumor phantoms, and tumors *in vivo* under a variety of parameters and conditions[95–97]. This approach to predicting the spatiotemporal heat distribution can enable optimization of nanoshell dosages for clinical treatment of tumors via photothermal therapy. Here, we report our theoretical derivation and results, where we considered three mathematical models to predict the heating of water due to irradiation of gold nanoshells (Figure 5.2): (1) a macroscopic energy balance to predict the temperature change within the well at the desired time points, assuming nanoshells at all locations generate heat and there is no heat loss from the well; (2) the differential form of the conservation of energy equation and the use of finite difference numerical methods to solve the partial differential equation at the different nodes, assuming nanoshells at all locations generate heat; (3) modification of Model 2 to allow only nanoshells within the path of the laser to generate heat.

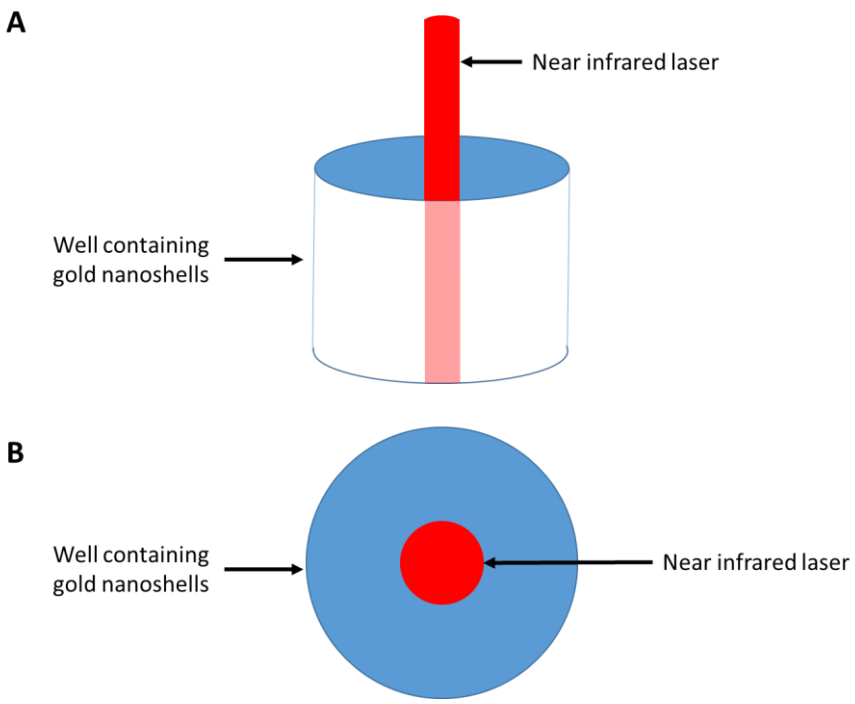

Figure 5.2 Diagram of the heat generation experiment performed in a 96-well plate with views from the (A) side and (B) top.

5.1 Methods

5.1.1 Model 1: Macroscopic Energy Balance – Bulk Heating

To predict the bulk, average temperature as a function of time, we applied an overall macroscopic energy balance to the well, where heat generation was assumed to occur at all positions within the well at the same constant rate:

$$\Delta T = \frac{Q_{laser}\Delta t}{\rho C_p} \tag{5.1}$$

where Δt is the change in time (s), ρ is the density of the fluid (kg/m^3), C_p is the specific heat capacity of water (J/kg*K), and ΔT is the change in temperature (K). Q_{laser} (W/m^3) is the heat

generated by the gold nanoshells, and it has been described by the following equation, which assumes all energy absorbed will be converted to heat[98]:

$$Q_{laser} = (\sigma_{abs} C_{GKL}) I \quad (5.2)$$

where σ_{abs} is the absorbance coefficient (1/mol*m), C_{GKL} is the concentration of gold nanoshells (mol/m^3), and I is the laser power density (W/m^2), where the laser power (0.2 W based on the purchased laser) was assumed to be equally distributed to all gold nanoshells within the entire well. Furthermore, if we assume all energy is absorbed by the gold nanoshells (neglecting the scattering of the light), the Beer-Lambert law can be used to replace the $\sigma_{abs}C_{GKL}$ term on the right hand side of Eq. (5.2) with A/g, where A is the optical density determined experimentally at the wavelength of irradiation from the UV-visible spectrophotometer (a.u.), and g is the path length of the cuvette used for the UV-visible spectrophotometer (0.01 m):

$$Q_{laser} = \frac{A}{g} I \quad (5.3)$$

Substituting (t-0) for Δt, along with (T_f-T_i) for ΔT where T_f and T_i are the final and initial (298 K) temperatures, respectively, Eq. (5.1) becomes the following equation:

$$T_f = \frac{Q_{laser} t}{\rho C_p} + T_i \quad (5.4)$$

To determine T_f as a function of time, Eq. (5.4) was solved at each time point using the parameters in Table 5.1.

Table 5.1. Heat transfer model parameters

Parameter	Description	Value
ρ	Fluid density	1000 kg/m^3
I	Laser power density	6220 W/m^2
C_p	Fluid heat capacity	4181 J/(kg*K)
A	Optical density	0.3 a.u.
k	Thermal conductivity of water	0.6 W/(m*K)
U_{wall}	Thermal conductivity through the wall	1.0x10^{-5} W/(m^2*K)
T_{wall}	Temperature of wall	298 K
h_{air}	Convective heat transfer coefficient of air	0.08 W/(m^2/K)
T_{air}	Temperature of air	298 K

5.1.2 Model 2: Differential Conservation of Energy Equation – Heat Generation at All Nodes

A more complex model for the heating of the well due to laser irradiation of the gold nanoshells was developed by using the differential form of the conservation of energy equation (Eq. (5.5)). This allowed there to be temperature gradients within the aqueous solution.

$$\rho C_p \frac{\partial T}{\partial t} = k\nabla^2 T + Q_{laser} \qquad (5.5)$$

The left-hand side of the equation is related to the change in energy with respect to time of a differential volume of solution. The first term on the right-hand side is associated with heat conduction (diffusion), while the second term is associated with the heat generated due to plasmonic heating of the gold nanoshells due to laser irradiation. In Eq. (5.5), T is the absolute temperature (K), t is time (s), k is the thermal conductivity (W/m*K), ρ is the density (kg/m^3), C_p

is the heat capacity (J/kg*K), and Q_{laser} can be obtained using Eq. (5.3). The parameters used in the model are shown in Table 5.1.

Since the experiment was performed in a 96-well plate as shown in Figure 5.2, Eq. (5.5) was analyzed in cylindrical coordinates, where expansion of the Laplacian yields:

$$\rho C_p \frac{\partial T}{\partial t} = k\left[\frac{1}{r}\frac{\partial}{\partial r}\left(r\frac{\partial T}{\partial r}\right) + \frac{1}{r^2}\frac{\partial}{\partial \theta}\left(\frac{\partial T}{\partial \theta}\right) + \frac{\partial}{\partial z}\left(\frac{\partial T}{\partial z}\right)\right] + Q_{laser} \qquad (5.6)$$

Since the temperature of the outer wall is the same all around and the nanoparticles should be relatively evenly distributed in the aqueous solution, this heat transfer problem is axisymmetric, and there is no temperature gradient in the θ direction. Equation (5.6) can therefore be simplified as follows:

$$\rho C_p \frac{\partial T}{\partial t} = k\left[\frac{1}{r}\frac{\partial}{\partial r}\left(r\frac{\partial T}{\partial r}\right) + \frac{\partial}{\partial z}\left(\frac{\partial T}{\partial z}\right)\right] + Q_{laser} \qquad (5.7)$$

In order to solve the above equation, we need two boundary conditions in the r-direction, two boundary conditions in the z-direction, and an initial condition (Figure 5.3).

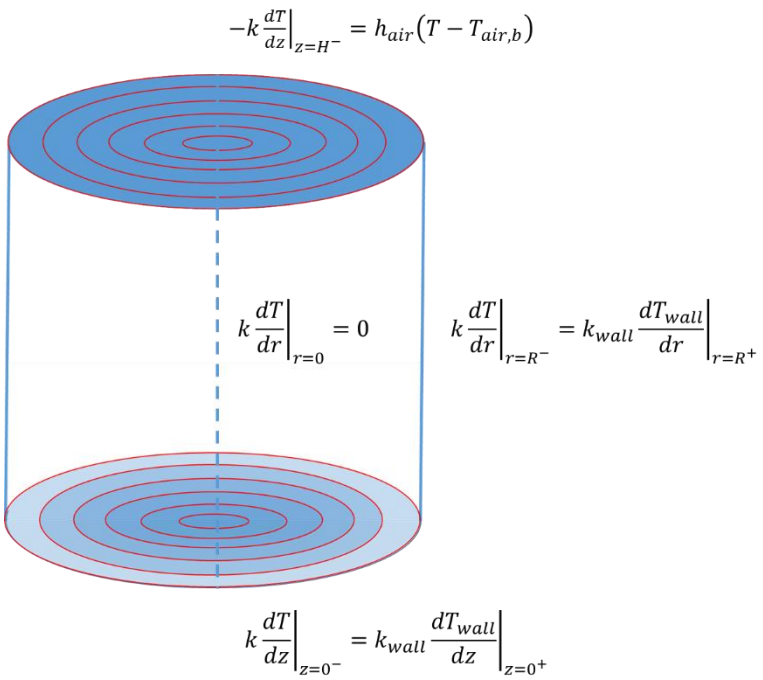

Figure 5.3 Boundary conditions. The dotted line (r = 0) is the symmetry axis. The r = R and z = 0 positions correspond to liquid-wall interfaces, and the z = H position corresponds to the liquid-air interface.

For the first boundary condition in the radial direction, we set the heat flux due to conduction to zero at the center (r = 0) due to axisymmetry:

$$k\frac{dT}{dr}\Big|_{r=0} = 0 \tag{5.8}$$

where k is the thermal conductivity of the water. The second boundary condition in the radial coordinate describes the heat flux to the wall due to conduction (r = R) is equal to the flux away through the wall (Eq. (5.9)).

$$k\frac{dT}{dr}\Big|_{r=R^-} = k_{wall}\frac{dT_{wall}}{dr}\Big|_{r=R^+} \tag{5.9}$$

where k_{wall} is the thermal conductivity of the polystyrene wall, T_{wall} is the temperature of the wall, R^- is the radial position just left of r = R in the aqueous solution, where R is the radius of the well, and R^+ is the radial position just right of r =R in the wall. For this model, we assumed that the temperature gradient through the wall is linear, and therefore, Eq. (5.9) can be simplified to the following:

$$-k\frac{dT}{dr}\Big|_{r=R^-} = U_{wall}\left(T_{wall,in} - T_{wall,out}\right) = U_{wall}\left(T - T_{wall,out}\right) \qquad (5.10)$$

where $U_{wall} = k_{wall}/d$, d is the thickness of the wall, $T_{wall,in}$ is the temperature of the inner wall that is equal to the temperature in the aqueous solution at $r=R^-$, and $T_{wall,out}$ is the outer temperature of the wall, which is assumed to be 25ºC.

The first boundary condition in the z-direction is located at the bottom of the well, and similar to Eq. (5.9). Specifically, the heat flux to the bottom of the well (z =0) is set equal to the heat flux through the wall:

$$k\frac{dT}{dz}\Big|_{z=0^-} = k_{wall}\frac{dT_{wall}}{dz}\Big|_{z=0^+} \qquad (5.11)$$

where $z = 0^-$ is the z-coordinate just below the bottom position of the well in the solid, and $z = 0^+$ is the z-coordinate just above the bottom of the well in the aqueous solution. Similar to Eq. (5.9), we assumed that the temperature gradient through the wall is linear, and Eq. (5.11) can be simplified to:

$$k\frac{dT}{dz}\Big|_{z=0^-} = U_{wall}\left(T_{wall,in} - T_{wall,out}\right) = U_{wall}\left(T - T_{wall,out}\right) \qquad (5.12)$$

where $U_{wall} = k_{wall}/d$, d is the thickness of the wall, $T_{wall,in}$ is the temperature of the inner wall that is equal to the temperature in the aqueous solution at $z=0^+$, and $T_{wall,out}$ is the outer temperature of the wall, which is assumed to be 25ºC. The second boundary condition in the z-direction

corresponds to the heat flux to the water-air surface (z = H) being equal to the heat convected away from the surface at the water-air interface:

$$-k\frac{dT}{dz}\Big|_{z=H^-} = h_{air}\left(T_{air,s} - T_{air,b}\right) = h_{air}\left(T - T_{air,b}\right) \quad (5.13)$$

where h_{wall} is the convective heat transfer coefficient for air, $z = H^-$ indicates the position just below the water-air interface in the aqueous solution, $T_{air,s}$ is the temperature of the air at the water-air interface (which is equal to the temperature of water at that same position), and $T_{air,b}$ is the bulk temperature of the air (25^{o}C).

The initial temperature condition for the entire aqueous solution (t =0) was set to the initial temperature of the water solution (T_i) 25 ^{o}C (298 K):

$$T(r, z, t = 0) = T_i \quad (5.14)$$

For this model, we solved the partial differential equation using the finite difference numerical method. For this approach, the aqueous solution in the cylindrical well was divided into a finite number of small regions and a reference point was assigned to the center of each region, termed a node (see Figures 5.4 and 5.5). Each node represents a certain region, and its temperature is a measure of the average temperature of the region. Increasing the number of nodal points in the r-direction (N_r) and the z-direction (N_z) increases the numerical accuracy. The nodes were uniformly spaced by a thickness, $\Delta r = R/N_r$ and $\Delta z = H/N_z$, where R is the radius of the well (3.2×10^{-3} m), N_r is the number of nodes in the r-direction (51), H is the height of the well (1.07×10^{-2} m), and N_z is the number of nodes in the z-direction (51).

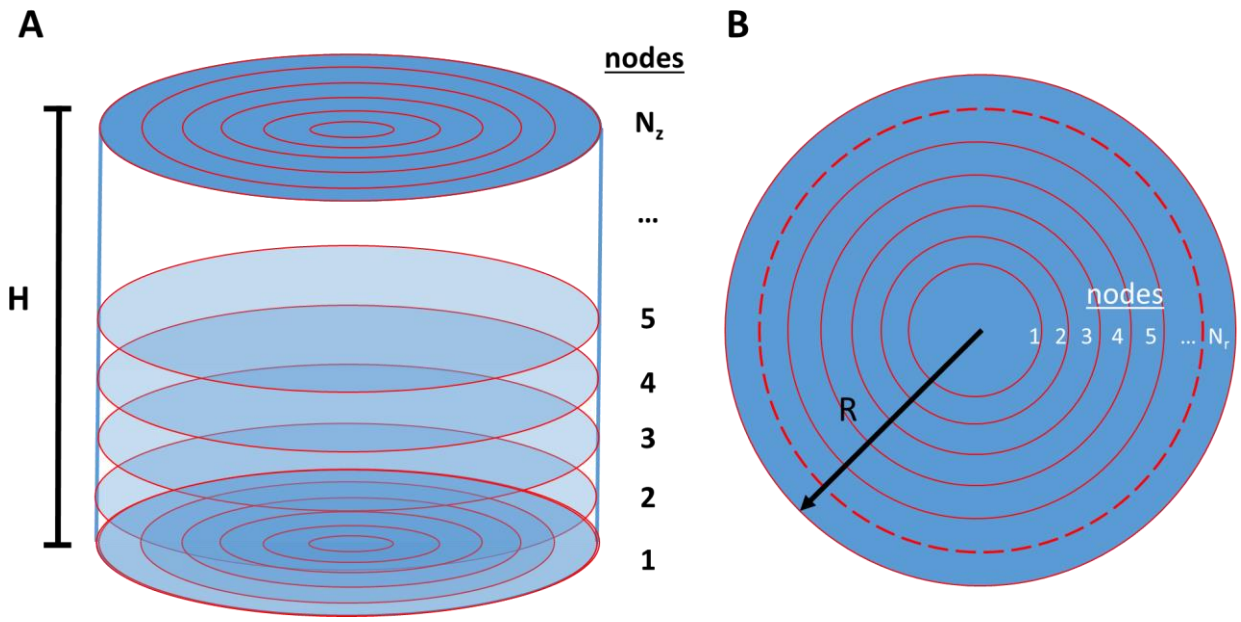

Figure 5.4. Diagram of the nodes for the medium in the 96-well plate with views from the (A) side and (B) top.

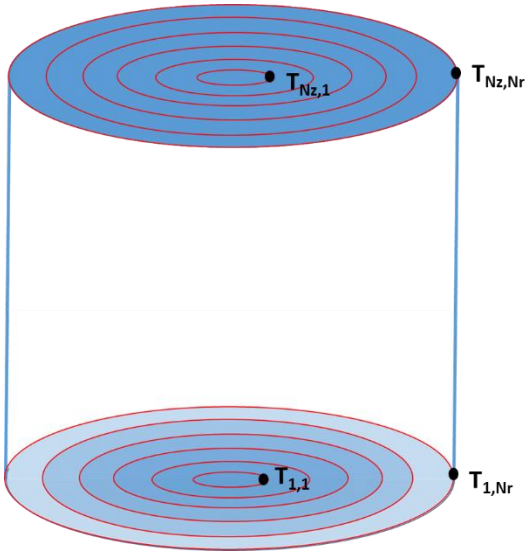

Figure 5.5. Schematic of the coordinate system for the medium in the 96-well plate, where N_r is the number of nodes in the r-direction and N_z is the number of nodes in the z-direction.

After writing the differential form of the conservation of energy equation for each node, the equations were converted using finite difference approaches. Specifically, for the interior nodes (non-boundary nodes), a finite-difference form of Eq. (5.7) was derived using the explicit discretization scheme as follows:

$$\frac{T_{i,j}^{n+1} - T_{i,j}^{n}}{\Delta t} = \alpha \left[\frac{T_{i,j+1}^{n} - 2T_{i,j}^{n} + T_{i,j-1}^{n}}{\Delta r^2}\right] + \frac{\alpha}{r}\left[\frac{T_{i,j+1}^{n} - T_{i,j-1}^{n}}{\Delta r}\right] + \alpha \left[\frac{T_{i+1,j}^{n} - 2T_{i,j}^{n} + T_{i-1,j}^{n}}{\Delta z^2}\right] + \frac{Q_{i,j}^{n}}{\rho C_p}$$

(5.15)

where i and j are the indices for the z and r nodes, respectively, Δt is the time step, Δr is the spacing of the nodes in the r-direction, Δz is the spacing of the z-direction, and the subscript n is used to denote the time dependence of temperature, where T^n and T^{n+1} are the previous and new temperature points, respectively. Additionally, to simplify the number of variables in the equation, α was set equal to $k/(\rho C_p)$. Rearranging to solve for the temperature at the new time point ($T_{i,j}^{n+1}$) yields the following:

$$T_{i,j}^{n+1} = \alpha\Delta t \left[\frac{T_{i,j+1}^{n} - 2T_{i,j}^{n} + T_{i,j-1}^{n}}{\Delta r^2}\right] + \frac{\alpha\Delta t}{r}\left[\frac{T_{i,j+1}^{n} - T_{i,j-1}^{n}}{\Delta r}\right] + \alpha\Delta t \left[\frac{T_{i+1,j}^{n} - 2T_{i,j}^{n} + T_{i-1,j}^{n}}{\Delta z^2}\right] + \frac{Q_{laser}\Delta t}{\rho C_p} + T_{i,j}^{n}$$

(5.16)

Similarly, the boundary conditions were rewritten using finite difference methods, where the boundary conditions in the r-direction (Eqs. (5.8) and (5.10)) were rewritten as Eqs. (5.17) and (5.18) using forward and backward finite difference equations, respectively, and the resulting equations were rearranged to solve for the appropriate node temperatures:

$$T_{i,1}^{n+1} = T_{i,2}^{n+1} \tag{5.17}$$

$$T_{i,nr}^{n+1} = \frac{T_{i,nr-1}^{n+1} + \frac{k_{wall}\Delta r}{d \quad k} T_{wall}}{1 + \frac{k_{wall}\Delta r}{d \quad k}} \tag{5.18}$$

For the z-direction boundary conditions (Eqs. (5.12) and (5.13)), the following equations were also derived using forward and backward finite difference equations, respectively:

$$T_{1,j}^{n+1} = \frac{T_{2,j}^{n+1} + \frac{k_{wall}\Delta z}{d \quad k} T_{wall}}{1 + \frac{k_{wall}\Delta z}{d \quad k}} \tag{5.19}$$

$$T_{nz,j}^{n+1} = \frac{T_{nz-1,j}^{n+1} + h_{air}\frac{\Delta z}{k} T_{air}}{1 + h_{air}\frac{\Delta z}{k}} \tag{5.20}$$

MATLAB code was then written to solve for the temperature at each r and z position (node) as a function of time using Eqs. (5.16)-(5.20). See Appendix for the MATLAB code.

5.1.3 Model 3: Combination of Models 1 and 2 - Heat Generation Only Within the Laser Irradiated Region

In this model, we assume that only the gold nanoshells within the path of the laser generate heat, and the heat is then conducted to the region outside of the path of the laser. For this approach, we defined two regions. The region in the path of the laser (the inner cylinder) was modeled with a macroscopic energy balance, while the region outside of this path (the cylindrical annulus) was modeled with the differential form of the conservation of energy equation to allow

for gradients in temperature in this region. Since all the properties in the inner cylinder are treated as being uniform due to the macroscopic energy balance approach and since the temperature of the outer wall is the same all around, this heat transfer problem is also axisymmetric and independent of the θ coordinate. Due to axisymmetry and the region outside of the laser illumination only being involved in heat conduction (Figure 5.6), the differential form of the conservation of energy equation for this cylindrical annulus region is given by:

$$\rho C_p \frac{\partial T}{\partial t} = k\left[\frac{1}{r}\frac{\partial}{\partial r}\left(r\frac{\partial T}{\partial r}\right) + \frac{\partial}{\partial z}\left(\frac{\partial T}{\partial z}\right)\right] \qquad (5.21)$$

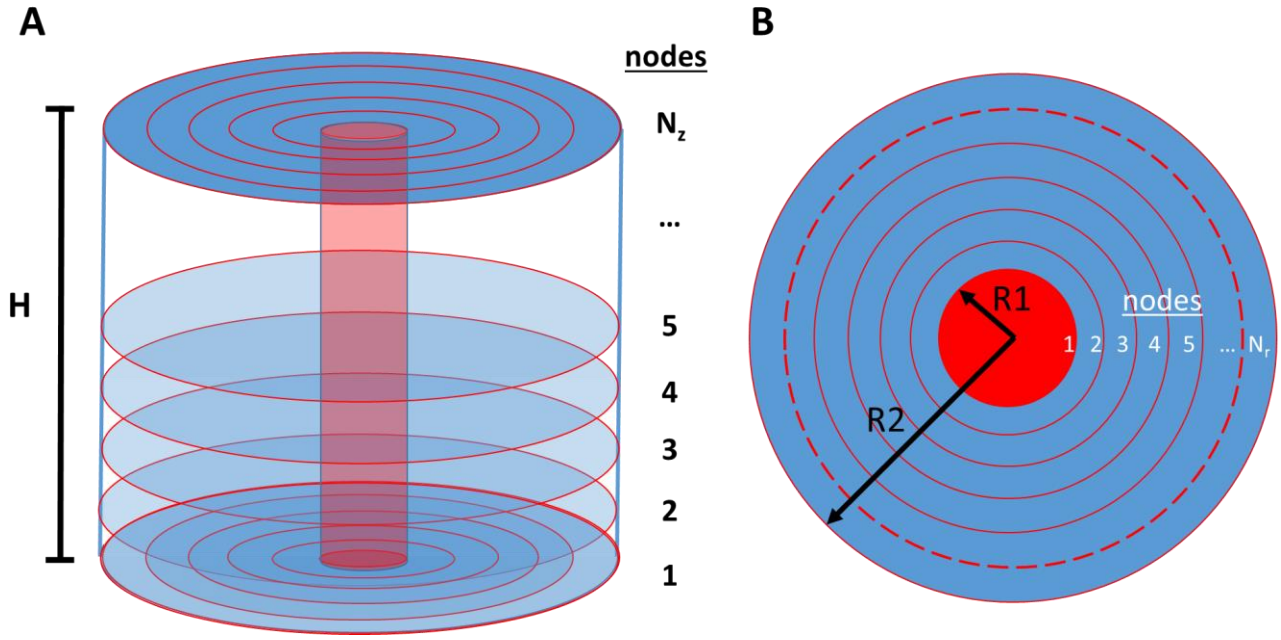

Figure 5.6. Schematic of the region illuminated by the laser, assumed to be a cylinder with a radius R1 (shown in red), and heat conduction occurs in the region outside the cylinder (R2 – R1, where R2 is the radius of the well) as shown by (A) side view (z-direction nodes) and (B) top view (r-direction nodes).

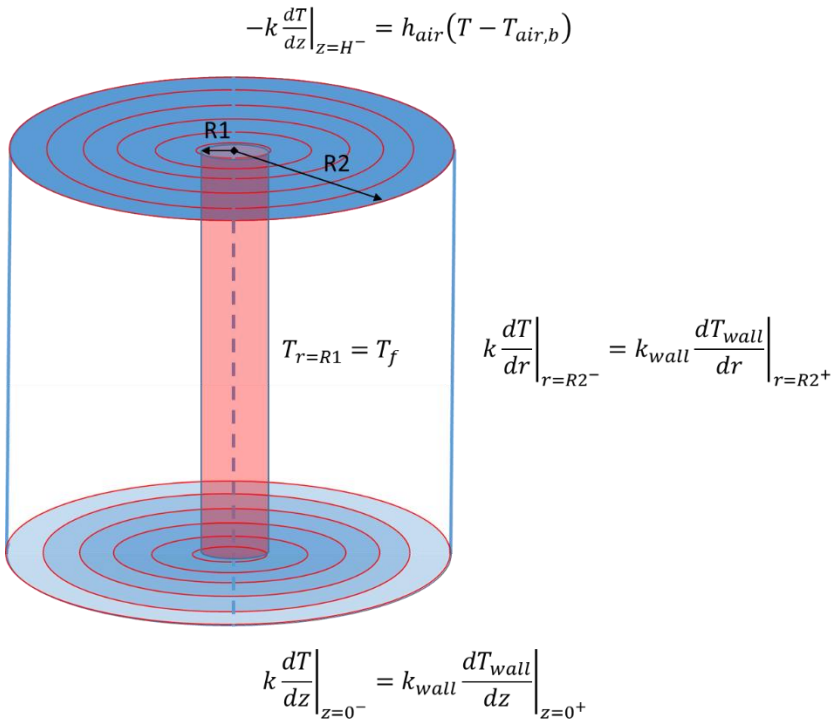

Figure 5.7. Boundary conditions. The temperature at r = R1 was determined by the macroscopic energy balance of irradiated region. The r = R2 and z = 0 positions correspond to the liquid-wall interfaces, and the z = H position corresponds to the air-liquid interface.

To solve Eq. (5.21), we need 2 boundary conditions in the r-direction, 2 boundary conditions in the z-direction, and one initial condition (Figure 5.7).

To determine the temperature boundary condition at node 1 at position r = R1, we applied a macroscopic energy balance to the region illuminated by the laser, which is modeled as an inner cylinder with radius R1 where all properties in this region are treated as being uniform, including heat generation

$$\Delta T = \frac{Q_{laser}\Delta t}{\rho C_p} \tag{5.22}$$

where Q_{laser} is the energy generated by the laser described by Eq. (5.3), Δt is the change in time, ρ is the density of the fluid, C_p is the specific heat capacity of water, and ΔT is the change in temperature in the inner cylinder. Substituting (t-0) for Δt, along with (T_f-T_i) for ΔT where T_f and T_i are the final and initial (298 K) temperatures, respectively, the final temperature at the time point of interest is given by:

$$T_f = \frac{Q_{laser} t}{\rho C_p} + T_i \qquad (5.23)$$

In this model, we determined the power density (I) to be 500,000 W/m^2, where the laser power (0.2 W) was divided by the inner area irradiated by the laser. Furthermore, the optical density of gold nanoshells within the irradiated region was estimated to be 0.006 a.u. since the area of the irradiated region was 2% of the total area of the well, and the total optical density of the entire well solution was 0.3 a.u. (0.3 a.u. x 0.02 = 0.006 a.u.).

For each time step, T_f is then used as the boundary condition at r = R1 (node j = 1) at all z-positions, $T_{i,1}$, since we assume uniformity throughout the entire cylinder.

$$T_{i,1} = T_f \qquad \text{Eq. (5.24)}$$

The remaining boundary conditions are the same as those used in Method 2, where there is heat conduction at the polystyrene wall (r = R2) and bottom (z = 0), as well as convection due to air at the top of the fluid (z = H) (Eq. 5.10, 5.12, 5.13). The initial condition used was the temperature at the start of the experiment, *i.e.*, 25 ºC (298 K).

The remaining boundary conditions are the same as those used in Model 2, where there is heat conduction at the side (r = R2) and bottom (z = 0) polystyrene wall, as well as convection due to air at the top of the fluid (z = H) (Eqs. (5.10), (5.12), and (5.13)). The initial condition was

also the same as in Model 2 (Eq. (5.14)), where the temperature throughout the entire solution at t=0 was 25ºC (298 K).

Similar to Model 2, we numerically solved the equations using finite difference numerical methods. For this approach, the cylindrical annulus outside the laser irradiation region (r = R2 - R1) was subdivided into a finite number of small regions and a reference point was assigned to the center of each region, termed a node (see Figure 5.6). The nodes were uniformly spaced by a thickness, $\Delta r = (R2-R1)/N_r$ and $\Delta z = H/N_z$, where R2 is the radius of the well (3.2×10^{-3} m), R1 is the radius of the illuminated region (0.5×10^{-3} m), N_r is the number of nodes in the r-direction (51), H is the height of the well (1.07×10^{-2} m), and N_z is the number of nodes in the z-direction (51).

In order to solve the governing equation (Eq. (5.21)), it was rewritten using finite difference approaches as shown below:

$$T_{i,j}^{n+1} = \alpha\Delta t\left[\frac{T_{i,j+1}^{n} - 2T_{i,j}^{n} + T_{i,j-1}^{n}}{\Delta r^2}\right] + \frac{\alpha\Delta t}{r}\left[\frac{T_{i,j+1}^{n} - T_{i,j-1}^{n}}{\Delta r}\right] + \alpha\Delta t\left[\frac{T_{i+1,j}^{n} - 2T_{i,j}^{n} + T_{i-1,j}^{n}}{\Delta z^2}\right] + T_{i,j}^{n} \quad (5.25)$$

This equation is the same as Eq. (5.16) except for the absence of the heat generation term. As previously mentioned, the initial condition was that the entire aqueous solution was at 298K (Eq. (5.14)). In addition to the boundary condition given by Eq. (5.24), the boundary conditions that were rewritten previously using finite difference approaches (Eqs. (5.18), (5.19), and (5.20)) were used again.

$$T_{i,j}^{n+1} = \alpha\Delta t\left[\frac{T_{i,j+1}^{n} - 2T_{i,j}^{n} + T_{i,j-1}^{n}}{\Delta r^2}\right] + \frac{\alpha\Delta t}{r}\left[\frac{T_{i,j+1}^{n} - T_{i,j-1}^{n}}{\Delta r}\right] + \alpha\Delta t\left[\frac{T_{i+1,j}^{n} - 2T_{i,j}^{n} + T_{i-1,j}^{n}}{\Delta z^2}\right] + T_{i,j}^{n} \quad (5.26)$$

Code was written in MATLAB to simultaneously solve the equations to determine the temperature at each node as a function of time (Appendix). To generate the transient temperature plots, a point was chosen at an r- and z- position that was estimated to be where the thermocouple was placed.

5.2 Results and Discussion

5.2.1 Model 1: Macroscopic Energy Balance – Bulk Heating

A macroscopic energy balance was performed in the entire aqueous solution to model the heat generation. In this case, the laser power was assumed to be distributed over the entire well. The temperature at each time point was calculated using Eq. (5.4), and the results are shown in Figure 5.8. The model predicted that the temperature increased linearly with time, where the slope was equal to $\frac{Q_{laser}}{\rho C_p}$ (Figure 5.8). This approximate macroscopic energy balance approach was not expected to accurately predict the experimental results, but it was encouraging to see that the temperature change of approximately 27 K with a final temperature of 325 K at 10 min was similar to the experimentally measured 23K change and a final temperature of 321 K at 10 min.

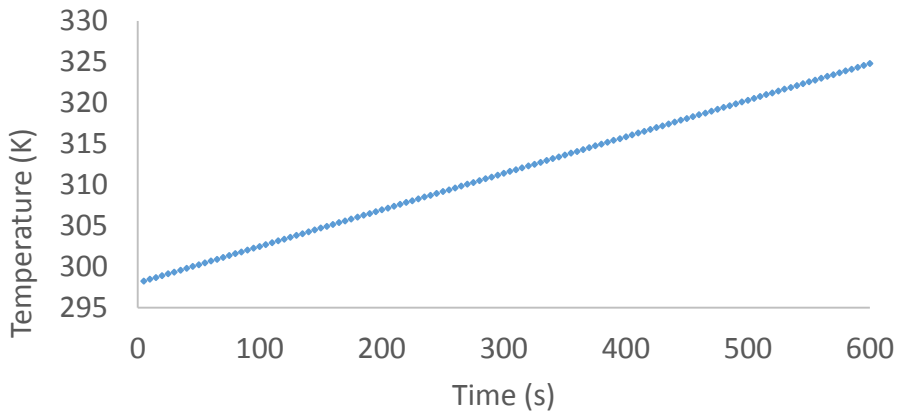

Figure 5.8. Predicted temperature as a function of time using Model 1.

5.2.2 Model 2: Differential Conservation of Energy Equation – Heat Generation at All Nodes

It was not surprising that the macroscopic energy balance did not capture the shape of the temperature increase with time. We knew that we instead had to consider temperature gradients within the system. Since this is very involved, we first developed Model 2 to determine whether our equations and MATLAB code could reproduce the results of Model 1. Despite being a more complex model involving many nodes, the results of Models 1 and 2 were expected to be almost exactly the same as all of the gold nanoshells were treated as being uniformly distributed within the aqueous solution, all of the nanoshells were allowed to generate heat, and the heat transfer to the environment was minimal due to small heat transfer coefficients and low wall conductivities. Model 2 predicted the temperature at r- and z- positions throughout the entire well at each time point (Figure 5.9). As shown in Figure 5.9, due to there being some heat transfer (although

minimal) to the air via convection, there was a slight temperature gradient in the z-direction. However, if you look closely at the values, the temperature gradient was extremely small.

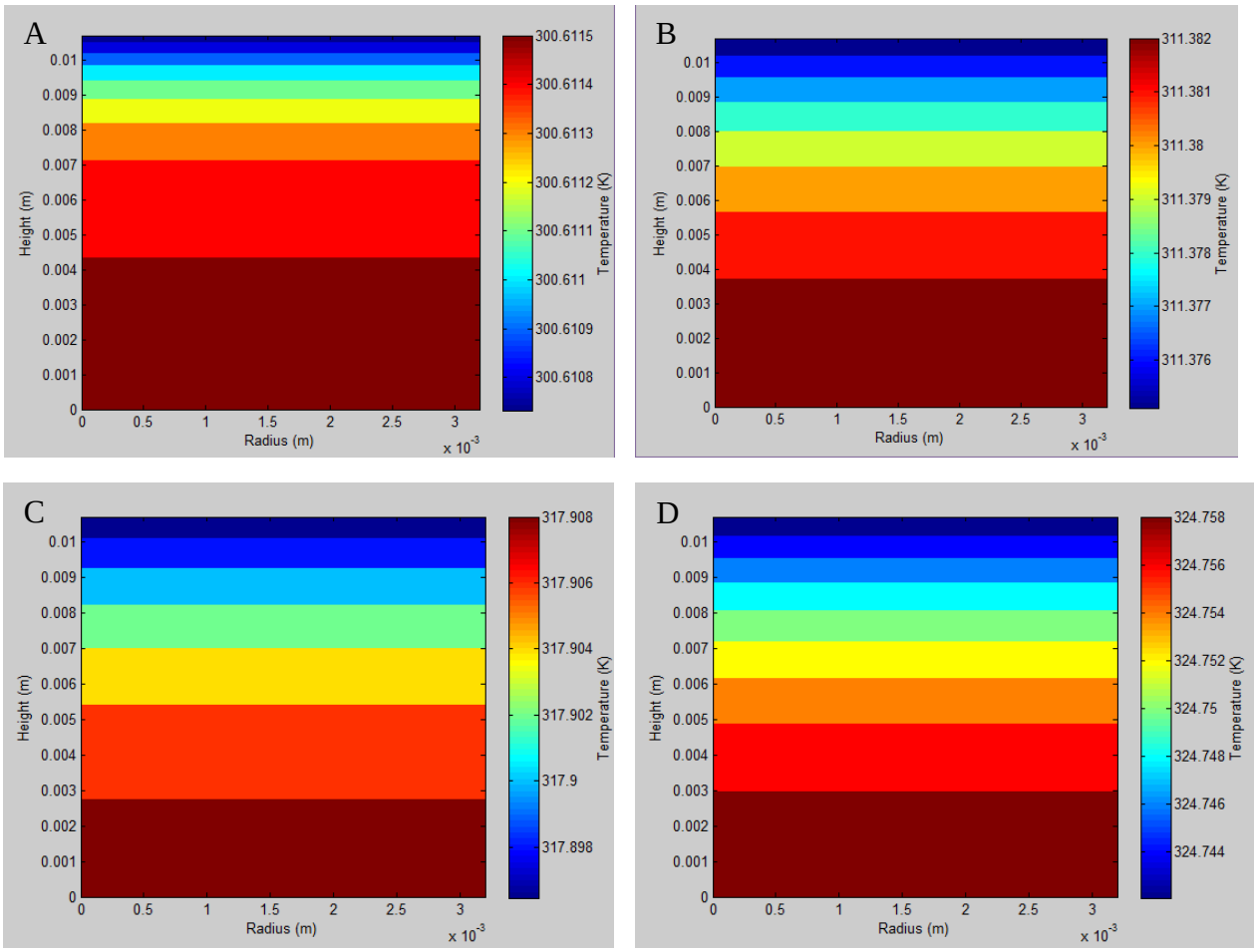

Figure 5.9. Predicted temperature profile of water in well using Model 2 at (A) 1 min, (B) 5 min, (C) 7.5 min, and (D) 10 min.

To compare with our experimental data, we subsequently chose a location within the well to closely match the location of the thermocouple in the experimental set-up to determine the temperature as a function of time. As expected and as shown in Figure 5.10, Model 2 predicted the same linear increase in temperature as a function of time as we had observed in Model 1. To understand this mathematically, note that all nodes in the well start at the same temperature and

have the same generation term (Q_{laser}), and gradients in temperature in the r- and z-directions are close to zero due to minimal heat transfer to the environment $\left(\frac{\partial T}{\partial r} = \frac{\partial T}{\partial z} = 0\right)$. We therefore can simplify Eq. (5.7) to the following expression:

$$\rho C_p \frac{dT}{dt} = Q_{laser} \tag{5.27}$$

Equation (5.26) can then be rearranged and integrated to find the temperature as a function of time, which turned out to be the same as Eq. (5.23) from Model 1:

$$T_f = \frac{Q_{laser} t}{\rho C_p} + T_i \tag{5.23}$$

Using a linear trend line, the slope and y-intercept were confirmed to be the expected values of $\frac{Q_{laser}}{\rho C_p}$ (0.044 K/s) and T_i (298 K), respectively.

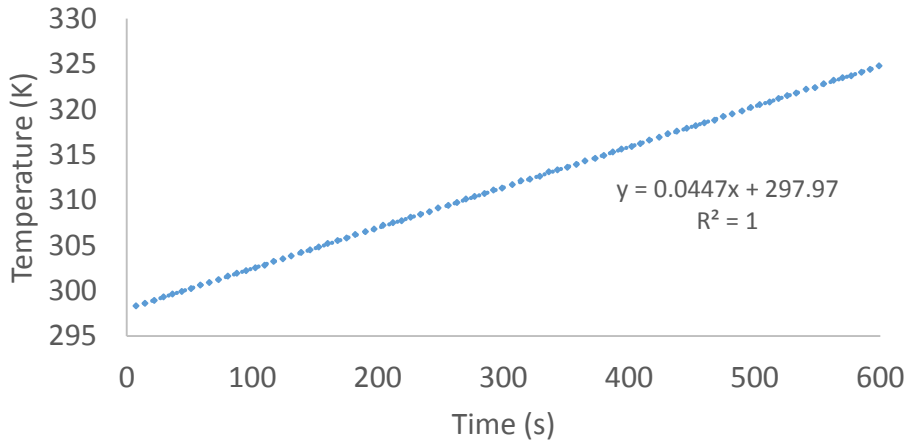

Figure 5.10. Predicted temperature as a function of time using Model 2.

5.2.3 Model 3: Combination of Models 1 and 2 – Heat Generation only within the Laser Irradiated Region

Model 3 corresponds to our first attempt to more closely capture all of the phenomena occurring in our *in vitro* experiment. As mentioned earlier, this model assumes that only the gold nanoshells within the path of the laser generate heat and that the heat is then conducted to the region outside of the path of the laser. This model predicted larger gradients than in the case of Model 3; however, the gradients were only in the radial direction (Figure 5.11).

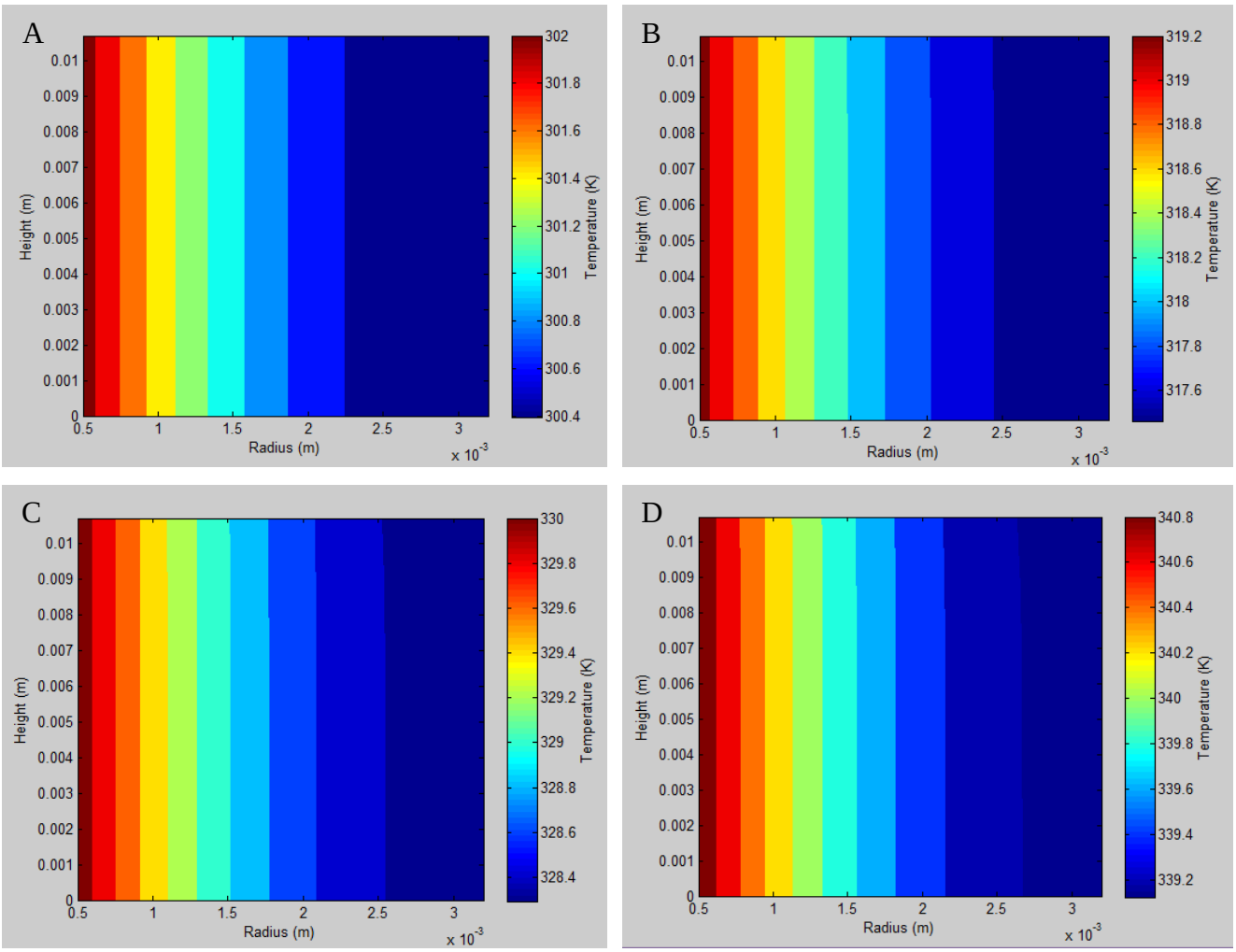

Figure 5.11. Predicted heating profile of water in well using Model 3 at (A) 1 minute, (B) 5 minutes, (C) 7.5 minutes, and (D) 10 minutes.

In order to determine the temperature dependence on time, we chose a position within the well, which was close to the location of the thermocouple in the experimental set-up. Model 3 also predicted that the temperature at this position varied linearly with time (Figure 5.12). Additionally, the change in temperature predicted (approximately 42 K) was significantly greater than the experimentally measured (approximately 27 K) as the final temperature at 10 min was predicted to be approximately 340 K instead of 321 K.

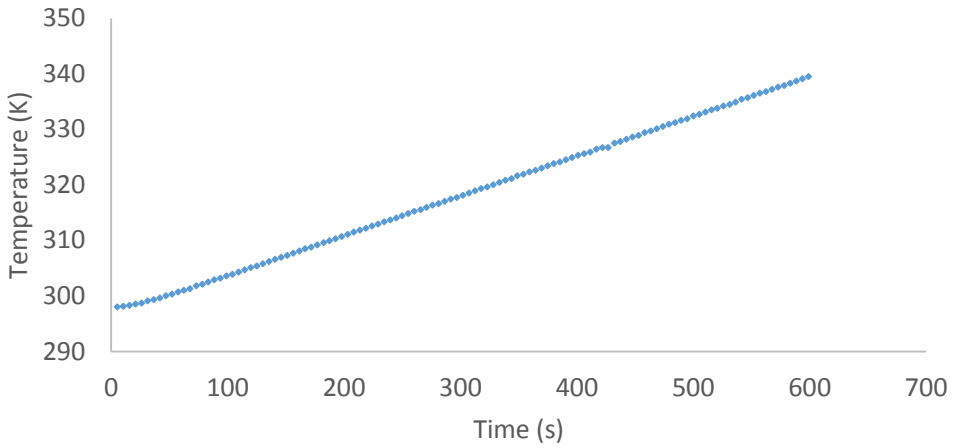

Figure 5.12. Predicted temperature as a function of time using Model 3.

It is not surprising that we are overpredicting the temperature rise. A closer look at Eq. (5.22) shows that we are assuming no heat loss from the inner cylinder. This assumption will need to be relaxed as heat is clearly being significantly conducted to the outer region represented by the cylindrical annulus. The current mathematical model does not allow this phenomenon to be taken into account as the equality of temperatures is used at the R1 boundary. Nevertheless, Model 3 is definitely more representative of the actual experimental set-up, and we further relaxed more assumptions of this model (see next section) to more accurately predict the shape of the temperature vs. time plot (since they have all been linear) as well as the final temperature.

5.3 Model 4: Relaxing Assumptions Made in Model 3

We relaxed more assumptions in our mathematical model to more accurately predict the heating of the gold nanoshells in response to irradiation with the near infrared laser. We focused on the following steps to improve the model:

- Allowed heat loss from the irradiated region, assumed to be an inner cylinder
- Allowed attenuation of the laser power along the z-direction due to interaction with gold nanoshells
- Allowed scattering of light by the gold nanoshells
- Increased heat loss due to conduction at the solid-liquid interface.
- Increased heat loss due to convection at the air-liquid interface.
- Increased heat loss due to heat of vaporization at the air-liquid interface.

In the next sections, the details of how we extended Model 3 to improve the model predictions will be discussed.

5.3.1 Heat Conduction from Irradiated Region

Previously, in Model 3, we modeled the irradiated region as a uniform cylinder, where the gold nanoshells in this region generated heat in response to laser exposure. Furthermore, the heat generated in this region was predicted using a macroscopic energy balance, and the final temperature at each time point became the boundary condition for solving the spatiotemporal temperature profile in the outer region. In Model 4, instead of using a uniform cylinder to represent the irradiated region, we allowed temperature variations in the inner cylinder by dividing the region into nodes, which continued into the outer region. The nodes in the irradiated region were modeled using the differential form of the conservation of energy equation

containing the heat generation term, Q_{laser}, (Eq. (5.7)), while the nodes outside the irradiated region were modeled with the differential form of the conservation of energy equation without the heat generation term (Eq. (5.21)). For our system, we estimated that the first 7 nodes would represent the irradiated region, where the radius of the laser was measured to be approximately 0.5 mm and each node was set a distance of 0.06 mm apart.

An initial condition (Eq. (5.14)) and boundary conditions were needed in order to solve the equations. In addition to the boundary conditions (1) at the center due to axisymmetry (Eq. (5.8)), (2) at the liquid-wall interface in the r-direction (Eq. (5.10)), (3) at the liquid-wall interface in the z-direction (Eq. (5.12)), and (4) liquid-air interface in the z-direction (Eq. (5.13)), we included two additional boundary conditions in the radial direction, which relate the heat loss from the irradiated region to the outer cylindrical annulus. Also note that the next sections will describe how we modified the boundary condition at the liquid-air interface (Eq. (5.13)) to incorporate heat loss due to evaporation.

The first additional boundary condition corresponded to the heat flux to the outer region (r = R1) being equal to the heat flux from the irradiated region (Eq. (5.28)).

$$-k\frac{dT}{dr}\Big|_{r=R1^-} = -k\frac{dT}{dr}\Big|_{r=R1^+} \tag{5.28}$$

where $R1^-$ is the radial position just left of r = R1 in the aqueous solution of the irradiated region (where R1 is the radius of the irradiated region) and $R1^+$ is the radial position just right of r =R in the aqueous solution in the outer region.

The second additional boundary condition in the radial coordinate assumes equilibrium of temperatures across the boundary of the irradiated region (r = R1) (Eq. (5.29)):

$$T|_{r=R1^-} = T|_{r=R1^+} \tag{5.29}$$

5.3.2 Attenuation of the Laser Power Along the Z-Direction

As the laser light passes through the solution, the gold nanoshells will act to absorb and scatter the light, which results in an attenuation of the laser power along the z-direction. Since our model assumes the heat generated by gold nanoshells, Q_{laser} (Eq. (5.3)), is directly proportional to the laser power density, attenuation of the laser power can greatly affect the temperature profile within the solution.

In order to incorporate this feature into our model, we utilized the Beer-Lambert Law to predict the laser power density, I, as a function of position within the well (Eq. (5.30))

$$I = I_0 * 10^{-(\varepsilon C_{GKL})z} \tag{5.30}$$

where I_0 is the laser power density in water only, and z is the vertical position in the well. Once again, the Beer-Lambert Law was used to replace the εC_{GKL} term in Eq. (5.30) with OD/g, where OD is the optical density as measured by the UV spectrophotometer and g is the path length (Eq. (5.31)).

$$I = I_0 * 10^{-\left(\frac{OD}{g}\right)z} \tag{5.31}$$

Here, we are using the optical density instead of only absorbance, since gold nanoshells significantly scatter, as well as absorb the light, and the scattering effect (which is also captured in the optical density) also acts to reduce the laser power density along the z-direction. The laser power density, I, predicted at each z-position can then be input into Eq. (5.3) to predict the heat generation term, Q_{laser}, at each point within the well. Using this model, we expect that gold

nanoshells near the bottom of the well will generate less heat, compared to gold nanoshells near the top of the well.

5.3.3 Scattering of Light by Gold Nanoshells

Previously in Model 3, we assumed that all the light was absorbed by the gold nanoshells and converted to heat. However, it has been previously shown that gold nanoshells significantly scatter the incident light, which does not contribute to the generation of heat. The fraction of light which is absorbed versus scattered by gold nanoshells is typically dependent upon the core diameter, shell thickness, and refractive index of water and gold.

In order to incorporate the scattering of light into our model, we estimated the energy absorbed by the gold nanoshells at 808 nm wavelength, and entered this value as A in the Q_{laser} equation (Eq. (5.3)). To estimate the energy absorbed by gold nanoshells, A, the Mie Theory was applied to determine the absorption cross-sectional area compared to the total extinction cross sectional area, where extinction is the sum of the scattering and absorption of light by the gold nanoshells[79,81,99]. It was determined that based on our gold nanoshell size, approximately 10% of the total light energy is absorbed. Therefore, to calculate A, the optical density at 808 nm as measured by a UV spectrophotometer was multiplied by 0.10, leading to predicting significantly less heat generation by our gold nanoshells, as compared to our previous models.

5.3.4 Increased Heat Loss at the Boundaries

5.3.4.1 Heat Transfer Coefficients

To more accurately capture the heat loss to the surroundings, we increased the conduction through the polystyrene plate and convection at the air-liquid interface. In our previous models, we chose parameters available in literature for a similar gold nanorod system[96]; however, for Model 4

we used a more rigorous approach then just using values published by another research group. Specifically, we used material properties and empirical correlations that were available in literature to predict the heat transfer coefficients. The values for the thermal conductivity through the wall, U_{wall}, and the convective heat transfer coefficient of air, h_{air} used in this model can be found in Table 5.2 below.

We first revisited the heat transfer coefficient related to the polystyrene plate, which is found in the boundary conditions at the wall in the radial direction at r = R2 (Eq. (5.10)) and at the bottom of the plate at z = 0 (Eq. (5.12)). To determine U_{wall}, we looked up the thermal conductivity of polystyrene (0.1 W/m*K[100]) and divided that by the thickness of the wall of the 96-well plate (measured to be $1x10^{-3}$ m) (Table 5.2). The increase in U_{wall} was expected to increase the rate at which the heat was conducted away from the solution through the polystyrene wall, reducing the overall temperature of the solution.

Next, we investigated the convective heat transfer coefficient at the air-liquid interface, which affects the boundary condition at z = H (Eq. (5.13)). To estimate the value of the convective heat transfer coefficient of air, we used empirical correlations that were determined for external free convection[101]. Using the correlations, we predicted a range of values for h_{air}, and tested them in Model 4. Table 5.2 lists the value for h_{air} that we decided upon. As in the case for U_{wall}, the increase in h_{air} was expected to increase the rate at which heat was lost from the solution, affecting the spatiotemporal temperature profile within the well.

Furthermore, we slightly increased the thermal conductivity of GKL in water, k, which affects the differential form of the energy conservation equations (Eqs. (5.7) and (5.21)), as well as the boundary conditions (Eqs (5.10), (5.12), (5.13), and (5.28)). The thermal conductivity was

increased to the shown in Table 5.2, because it is reasonable to assume that a high concentration of GKL could increase the conductivity of the solution. In fact, this assumption has been made in similar energy conservation mathematical models for capturing the photothermal therapy effect of gold nanorods[96].

Table 5.1. Model 4 heat transfer parameters

Parameter	Description	Value
ρ	Fluid density	1000 kg/m^3
I_0	Laser power density in water	3.33x10^5 W/m^2
C_p	Fluid heat capacity	4184 J/(kg*K)
OD	Optical density	0.6 a.u.
k	Thermal conductivity of GKL in water	0.75 W/(m*K)
U_{wall}	Thermal conductivity through the wall	100 W/(m^2*K)
T_{wall}	Temperature of wall	290 K
h_{air}	Convective heat transfer coefficient of air	15 W/(m^2/K)
T_{air}	Temperature of air	290 K
$\dot{m}$	Average rate of mass loss to evaporation	3.3x10^{-8} kg/s
H_{vap}	Heat of vaporization	2.46x10^6 J/kg

5.3.4.2 Evaporative Cooling at the Air-Liquid Interface

In order to more fully capture the heat loss occurring in the well, we also incorporated evaporative cooling at the air-liquid interface. Here we estimated the amount of solution that is evaporated over the laser irradiation period based on the mass of water apprearing as condensate on the wall of the well over the duration of the experiment. This mass loss was assumed to occur at a linear rate, and the estimated average rate of mass loss due to evaporation is shown in Table

5.2. Next, to incorporate this effect into our model, we included it in the boundary condition at the air-liquid interface. Specifically, Eq. (5.13) is replaced with the following equation:

$$-k\frac{dT}{dz}\Big|_{z=H^-} = h_{air}\left(T_{air,s} - T_{air,b}\right) + \frac{\dot{m}H_{vap}}{S} = h_{air}\left(T - T_{air,b}\right) + \frac{\dot{m}H_{vap}}{S} \tag{5.32}$$

where $\dot{m}$ is the average rate of water loss to evaporation, H_{vap} is the heat of vaporization of water, and S is the surface area of the well, estimated to be 32 mm^2 (Table 5.2).

5.3.5 Modeling Heat Generation for our Optimized Polypeptide-Based Gold Nanoshells

In this section, we show the results of applying the above modifications to predict the experimental heat generation as a function of time for the optimized polypeptide-based gold nanoshells.

In order to determine the spatiotemporal variations in temperature, we again used the finite difference method to expand the conservation of energy equations in the irradiated region, as well as the solution in the outer region, Equs (5.7) and (5.21), respectively. Next, we applied the boundary conditions with the modifications addressed earlier in Section 5.3 (Eqs (5.8), (5.10), (5.12), (5.13), (5.28), and (5.29)) and the initial condition (Eqn (5.14)). Using the revised model, we predicted temperature gradients in the radial and z-directions as shown in Figure 5.13. As shown in Figure 5.14, Model 4 did a reasonable job of predicting the increase in temperature with respect to time, indicating that relaxing the assumptions of Model 3 more appropriately captured the physical processes occurring in the experiment.

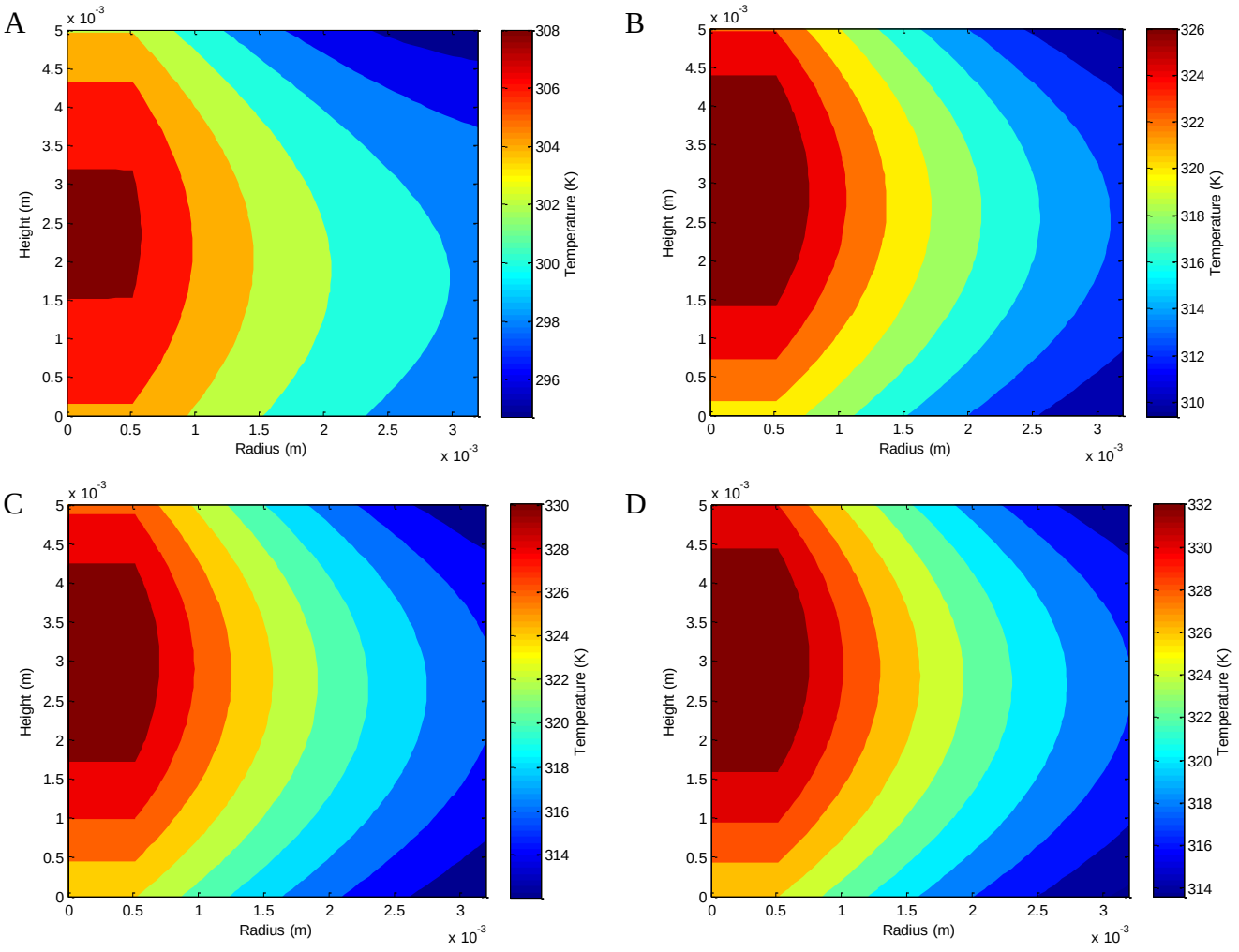

Figure 5.13. Predicted heating profile of water in well using Model 4 at (A) 1 minute, (B) 5 minutes, (C) 7.5 minutes, and (D) 10 minutes.

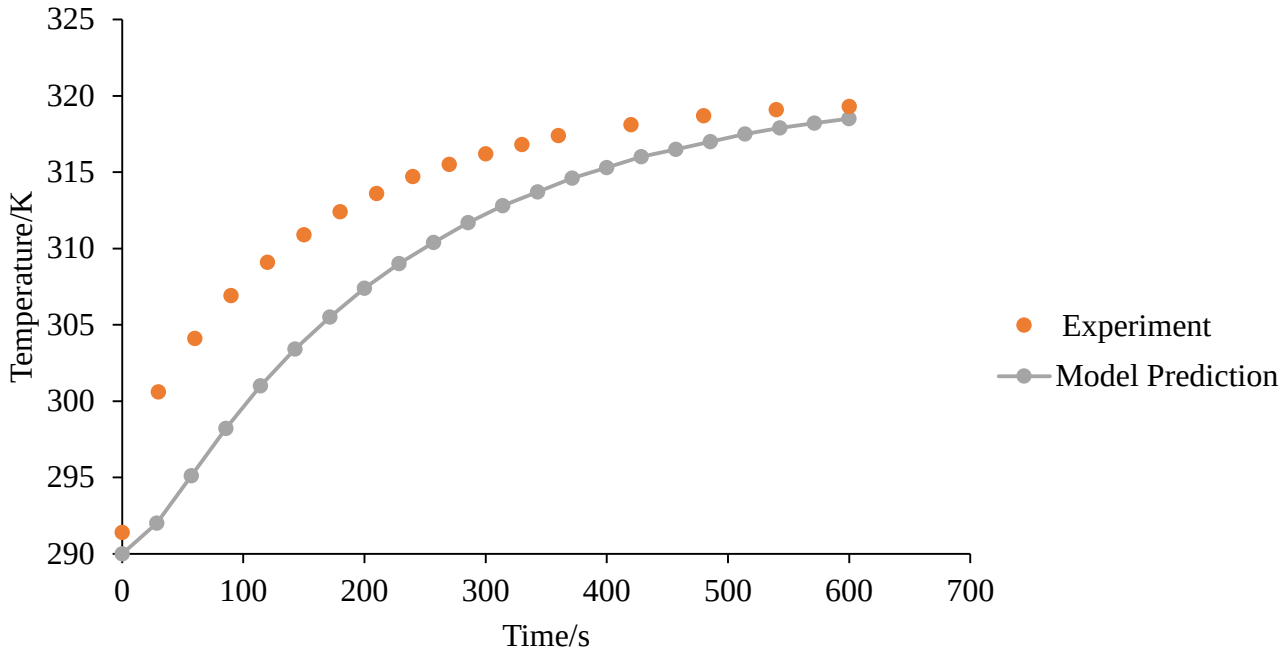

Figure 5.14. Mathematical model prediction of temperature profile for gold nanoshells in water with exposure to a 200 mW laser diode, 808 nm.

5.4 Conclusions

We developed a comprehensive mathematical model for heat transfer to predict the temperature as a function of time and position in our *in vitro* experimental set-up. Our mathematical model was validated by comparing our predictions with our experimental results. We envision using the model in the future to determine how we can engineer our gold nanoshells to improve heating properties. For example, in our current mathematical model, Q_{laser} is related to the absorbance of our gold nanoshells, and that is an input into the model that we can manipulate through engineering the design of the nanoshells. We want to be able to improve heat generation, which, in turn, would lead to greater destruction of tumors.

6 Investigating Targeted Polypeptide-Based Gold Nanoshells

An enhancement in cancer cell killing efficacy for gold nanoshells has been demonstrated by specifically targeting receptors and antigens on the surfaces of cancer cells[84,102–106]. Based on the high specificity of the A11 minibody for PSCA-expressing prostate cancer cells, we investigated its use as a targeting ligand for the polypeptide-based gold nanoshells developed in Chapter 4 for the treatment of prostate cancer.

6.1 Potential for PSCA-Targeted Therapeutics Using the A11 Minibody

Prostate cancer cells can be targeted through prostate-specific membrane bound antigens, such as prostate specific membrane antigen (PSMA) and prostate stem cell antigen (PSCA). Here, we focused on targeting PSCA, which is predominantly prostate-specific and is overexpressed on prostate cancer cells with restrictive expression in normal tissues. PSCA expression increases markedly with tumor stage, grade, and progression to androgen independence, where PSCA was found in 80% of localized tumors and all bone metastases[107,108]. The expression patterns of PSCA enable targeting of difficult to treat metastatic and androgen-independent tumor cells. Based on the promise of PSCA, researchers developed antibodies against PSCA, which could enable specificity in the treatment and imaging of prostate cancer cells.

Previously, a murine monoclonal antibody was generated against PSCA to be used for immunotherapy, which is the use of antibodies to stimulate host tumor-antigen-specific immune response. The murine monoclonal antibody inhibited prostate cancer tumor growth and metastases for both androgen-dependent and androgen-independent cells, prolonging the life of tumor-bearing mice[109]. The mechanism of action for the antibody was found to be direct and

dependent on cross linking; however, due to the lack of understanding of the function of PSCA in cancerous and normal tissues the downstream signaling induced by antibody binding has not been determined[110]. Since murine monoclonal antibodies can be immunogenic and result in the development of a human antihuman antibody (HAMA) response in patients, a humanized version was then developed, which was also able to bind and inhibit growth of prostate cancer cells that even had low levels low PSCA expression[111]. While the humanized antibody showed promise for prostate cancer treatment, the high specificity also made it a promising candidate for diagnostic imaging.

Positron emission tomography (PET) for the detection of prostate cancer has been limited by nonspecific uptake, low glucose utilization, and inefficient radiolabeling and synthesis of radiotracers. Therefore, researchers have developed PET probes, which specifically target antigens present on prostate cancer cells. Although the humanized anti-PSCA antibody appeared promising as a specific PET probe for detection of prostate cancer, the long circulation half-life of the full-sized antibody prevented imaging of the tumor until 168 hours post-injection when the background signal became low. To enable more rapid imaging of the tumor, an engineered antibody fragment, the anti-PSCA minibody (single-chain Fv-CH3 dimer), was developed[112]. Antibody fragments have demonstrated high binding specificity with rapid clearance from circulation and non-target tissue[113]. The shortened circulation half-life of the minibody enabled imaging of PSCA-expressing tumors within 21 hours post-injection[112]. However, during the development of the humanized minibody, the binding affinity to PSCA was also reduced. Therefore, to improve the affinity of the parental minibody, an affinity maturation process was used to derive minibody variants, which bound strongly to PSCA and cleared quickly from the body. Using molecular evolution combined with yeast display, the A11 minibody was developed

by Dr. Anna Wu's laboratory, which allowed successful imaging of localized and metastatic prostate cancer with high contrast[114,115].

The high affinity and specificity for PSCA-expressing cells also makes A11 an ideal candidate for targeting therapeutics for the treatment of local and metastatic prostate cancer. We first confirmed that A11 binds to PSCA-expressing cells, and exhibits a slow internalization rate (see Appendix). Subsequently, as discussed in this chapter in this chapter, we extended the application of the engineered A11 minibody to include being a targeting agent for therapy. Here, we show the PSCA-targeted polypeptide-based gold nanoshells demonstrate greater laser-induced cytotoxicity compared to non-targeted PEGylated gold nanoshells.

6.2 Materials and Methods

6.2.1 Synthesis of A11 Minibody

The A11 minibody was received as a generous gift from Dr. Anna Wu's laboratory at UCLA. The A11 minibody was produced and purified as described previously[114].

6.2.2 Making Polypeptide-Based Gold Nanoshells

The $K_{60}L_{20}$ vesicles were processed and extruded as described in Chapter 4. For conjugating to gold nanoshells, we needed to increase the amount of gold nanoshells; therefore, the synthesis process was slightly altered to accommodate a larger mass of vesicles. A 4.63 mL solution of polypeptide vesicles (1.34 mg) was adjusted to pH 7 using 7% ammonium hydroxide (Sigma-Aldrich, St. Louis, MO). Hydroxylamine hydrochloride (Sigma-Aldrich, St. Louis, MO) was added in excess (500 µL of a 0.2 M solution), followed by 154 µL of a 0.5% gold (III) chloride solution (Sigma-Aldrich, St. Louis, MO) in two 77 µL aliquots. The solution was allowed to spin overnight, and the gold coated vesicles were recovered by centrifugation at 9,000

rcf for 10 minutes. As previously determined, the pH was critical in the gold coating process, and therefore the pH was adjusted as needed to maintain a pH of 7 throughout the coating process.

6.2.3 Conjugation Scheme for A11 and PEG to Polypeptide-Based Gold Nanoshells

Gold nanoshells can be surface-functionalized with thiol-containing moieties through dative bonds. In order to conjugate A11 to the gold nanoshells, we cleaved the disulfide linker between the constant regions of the minibody to expose free thiols. Briefly, free thiol groups on A11 were exposed by breaking the disulfide linkages between the heavy chains using a 3:1 molar ratio of the minibody to dithiolthreitol (DTT), enabling conjugation to the gold nanoshells through dative bonds. The free DTT was then purified from the thiolated A11 using 10K MWCO spin concentrators (EMD Millipore, Billerica, MA). We also saturated the gold nanoshell surface using thiol-functionalized polyethylene glycol (PEG), which has been shown to provide *in vivo* stability for nanoparticles. To conjugate the PEG and A11 to the gold nanoshells, the pH of the gold nanoshell solution was adjusted to 9 using 1.5 M NaOH. Monofuctional methoxy-PEG-thiol (5,000 molecular weight) (Nanocs, Boston, MA) and thiolated A11 were added at a molar ratio of 10000:1000:1 PEG:A11:gold nanoshell. To ensure adequate conjugation of A11, 0.08 mg of A11 was added to the gold nanoshells first, and allowed to react for 30 minutes while stirring, followed by the conjugation of 0.1 mg PEG for 10 minutes. Free PEG and A11 were purified by centrifugation at 2000 rcf for 2 min. To provide stability during the recovery process, we added bovine serum albumin (BSA) in excess (50 µL of 10% wt/vol BSA) to passivate the surfaces of the plastic tube as well as the gold nanoshell. To make the PEGylated gold nanoshells, a similar protocol was followed without the addition of A11. Finally, to make the IgG conjugated gold nanoshells, a similar protocol was followed with the addition of Sheep anti-Rabbit IgG-h + I (Bethyl Laboratories, Inc., Montgomery, TX).

6.2.4 Characterization of A11-Conjugated Gold Nanoshells

Size measurements were performed on the A11-conjugated and PEGylated gold nanoshells with the Malvern Zetasizer Nano ZS model Zen 3600 (Malvern Instruments Inc, Westborough, Massachusetts). TEM images were taken of the gold nanoshells with the T20 iCorr (FEI) High-Resolution CryoEM from the FEI Tecnai G2 Family with the help of Dr. Hong Zhao's group. The extinction profile of the A11-conjugated gold nanoshells was used to verify the strong surface plasmon resonance in the near infrared region as determined by a UV-visible spectrophotometer over a range of wavelengths from 400 to 1000 nm.

6.2.5 Measuring Heat Generation

Gold nanoshells (absorbance = 0.2 a.u.) were irradiated with a 200 mW laser diode, 808 nm (ThorLabs, Inc., Newton, NJ) for 10 minutes, where the laser set-up was designed by Dr. Grundfest's laboratory. The temperature was measured at desired time points using a thermocouple.

6.2.6 Photothermal Therapy Using A11-Conjugated Nanoshells

Gold nanoshells were incubated with PSCA-expressing 22Rv1 prostate cancer cells for 30 minutes in serum-free media. After incubation, cells were washed with PBS, and after the last wash, PBS was left in the well. Cells were then irradiated with an 808 nm laser diode (200 mW) for 10 minutes. A Live/Dead Stain Kit (calcein AM and ethidium homodimer, Molecular Probes, CA, USA) was used to evaluate the viability of the cells. Cells were examined using fluorescent microscopy with EVOS fl Digital Inverted Fluorescence Microscope (Advanced Microscopy Group/Life Technologies, Grand Island, NY).

6.3 Results and Discussion

6.3.1 A11-Conjugated Polypeptide-Based Gold Nanoshells

After demonstrating success in making the polypeptide-based gold nanoshells discussed in Chapter 4, we investigated the use of the A11 minibody to enhance the specificity of the gold nanoshells. Here, we developed a conjugation scheme to create a targeted, A11-conjugated gold nanoshell and a non-targeted gold nanoshell. Both targeted and non-targeted gold nanoshells were conjugated to polyethylene glycol (PEG), which has been shown to provide *in vivo* stability to nanoparticles, preventing aggregation and nonspecific adsorption of serum proteins. Characterization of the gold nanoshells showed that they were around 200 nm in size, and formed a relatively monodisperse population (Table 6.1). The TEM images of the gold nanoshells confirmed the dynamic light scattering results (Figure 6.1). Furthermore, the extinction profile demonstrated that the targeted and non-targeted gold nanoshells maintain the strong surface plasmon resonance in the near infrared region (Figure 6.2).

Table 6.1. Characterization of targeted and non-targeted polypeptide-based gold nanoshells

$K_{60}L_{20}$ Vesicles	Size (nm)	Polydispersity Index (PDI)
Gold-coated	148 ± 3	0.11 ± 0.01
Non-targeted	183 ± 4	0.14 ± 0.03
Targeted	200 ± 5	0.21 ± 0.01

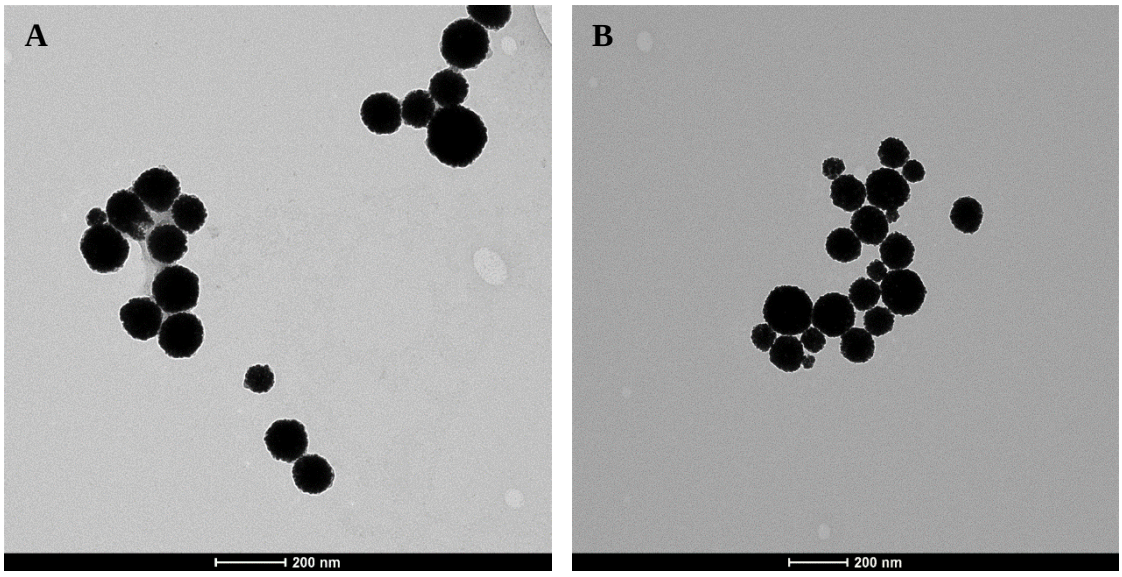

Figure 6.1. TEM images of (A) targeted, A11-conjugated and (B) non-targeted, PEGylated polypeptide-based gold nanoshells. Scale bar is 200 nm.

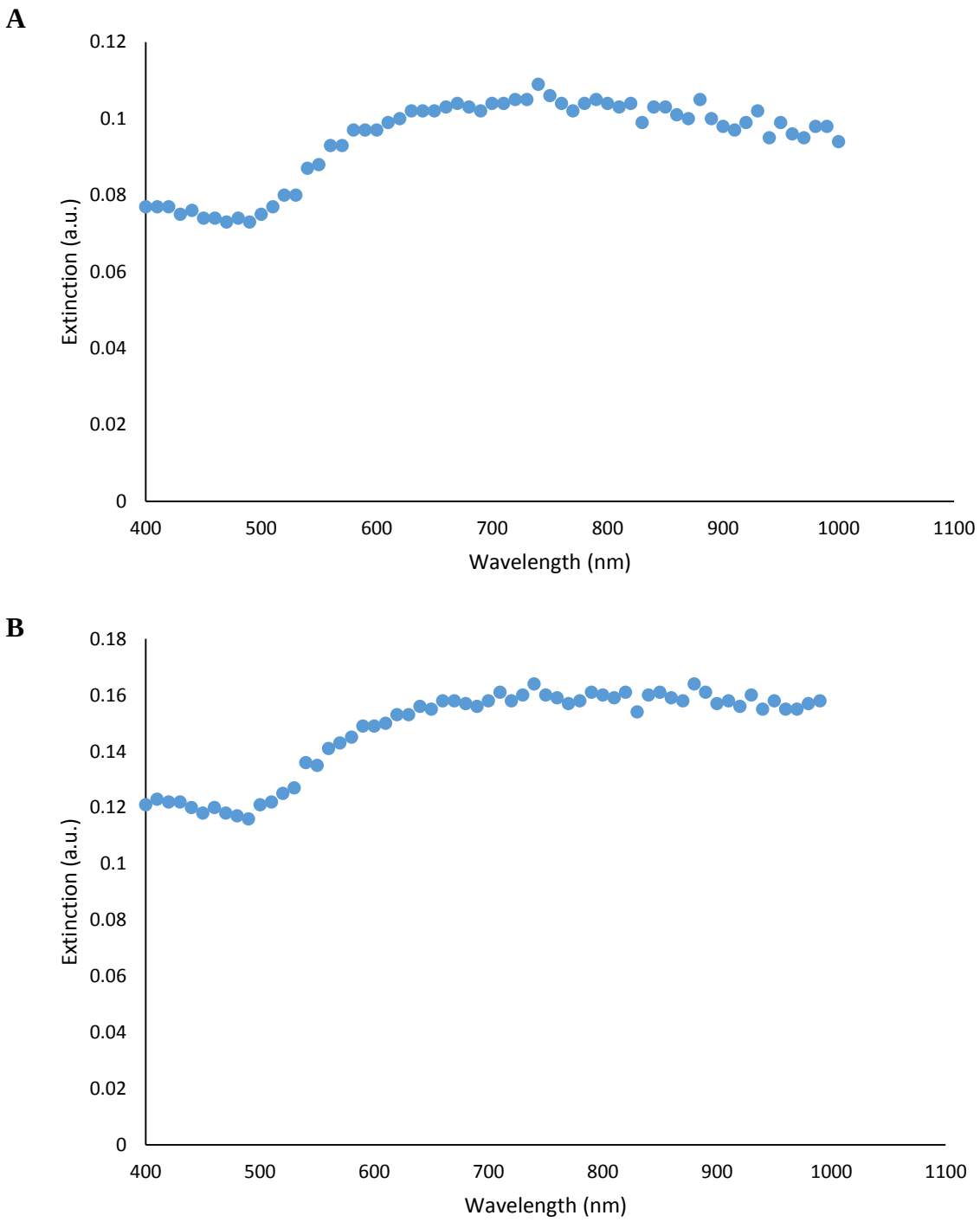

Figure 6.2. Extinction profile for (A) non-targeted, PEGylated polypeptide-based gold nanoshells and (B) targeted, A11-conjugated PEGylated polypeptide-based gold nanoshells.

6.3.2 PSCA-Targeted Photothermal Therapy Using Polypeptide-Based Gold Nanoshells

Furthermore, we evaluated the ability to generate heat in response to near infrared laser irradiation. As shown in Figure 6.3, both the targeted- and non-targeted gold nanoshells generated significant amount of heat within 10 minutes with a similar heating profile. Using these gold nanoshells *in vitro*, we demonstrated localized and specific, laser-induced cytotoxicity, where PSCA-22Rv1 cells incubated with targeted gold nanoshells showed cell death only within the irradiated region (Figure 6.4 A, B), and no similar region was observed for the non-targeted gold nanoshells (Figure 6.4 C, D). These results seem to indicate that the A11 minibody enhances the cellular binding and association of gold nanoshells, which results in greater efficacy of the gold nanoshells.

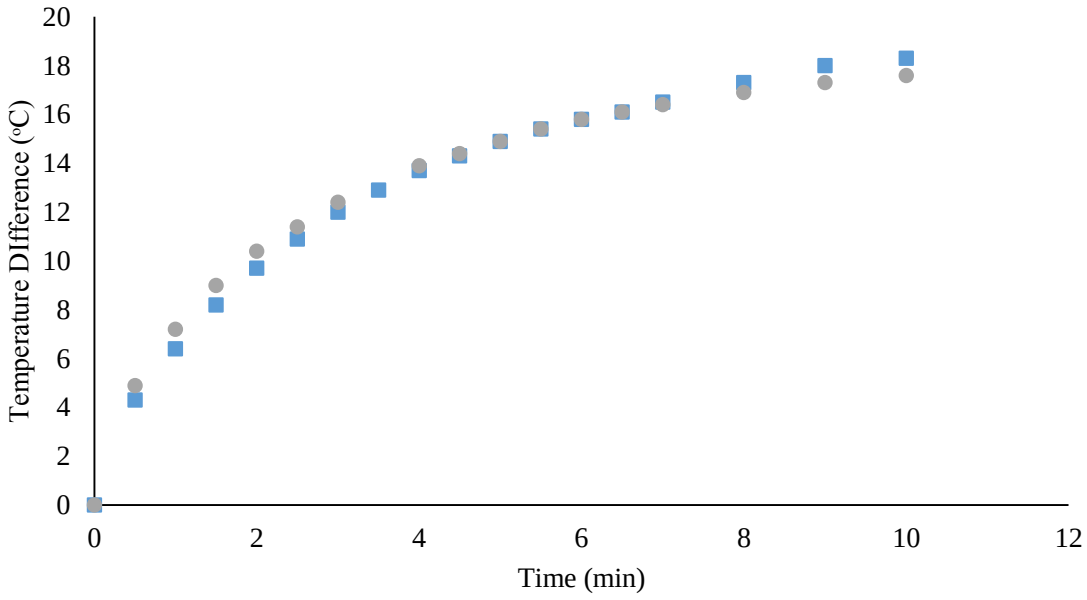

Figure 6.3. Heat generation as a function of time for targeted- (blue squares) and non-targeted (grey circles) gold nanoshells.

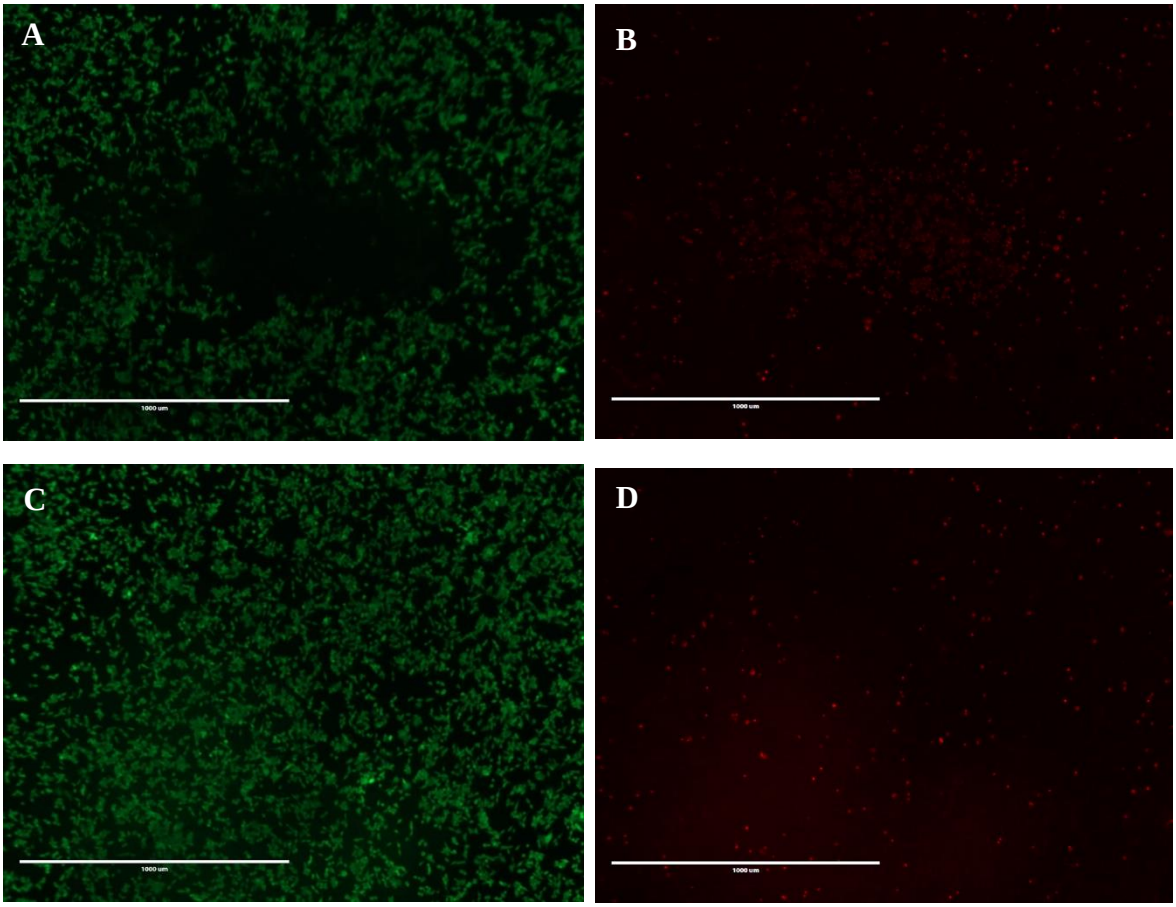

Figure 6.4. Laser-induced cytotoxicity for (A, B) A11-conjugated, targeted gold nanoshells and (C, D) non-targeted gold nanoshells. Live cells are shown in green and dead cells are shown in red. Scale bar = 1 mm. (Absorbance at 808 nm= 0.4 a.u.)

6.4 Specificity of A11-PSCA interaction

To evaluate the importance of the specific interaction of the A11-conjugated gold nanoshells with the PSCA on the prostate cancer cells, we created gold nanoshells conjugated to an IgG antibody that does not bind to PSCA. The IgG antibody was not expected to bind specifically to the prostate cancer cells, and therefore we expected to have little to no laser-induced toxicity. The results of the study are shown in Figure 6.5, where we compared the cytotoxicity of A11-

conjugated versus IgG-conjugated gold nanoshells after laser irradiation. The A11-conjugated gold nanoshells demonstrated significant laser-induced toxicity within the laser-irradiated region, while the IgG gold nanoshells demonstrated limited toxicity. As expected, the A11-PSCA interaction is critical in the enhancement of the efficacy of the polypeptide-based gold nanoshells.

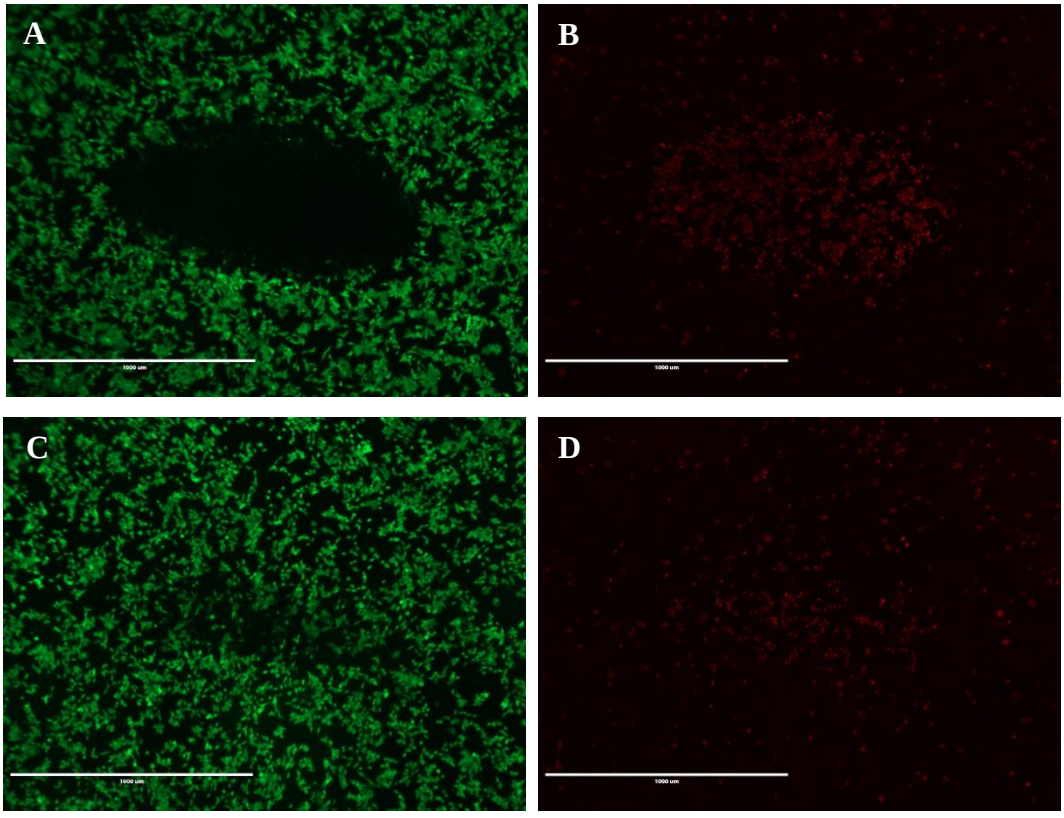

Figure 6.5. Laser-induced cytotoxicity for (A, B) A11-conjugated, targeted gold nanoshells and (C, D) non-targeted gold nanoshells. Live cells are shown in green and dead cells are shown in red. Scale bar = 1 mm. (Absorbance at 808 nm = 0.7 a.u.)

6.5 Conclusions

This work represents the first use of the A11 minibody as a targeting agent for a therapeutic nanoparticle system. Here, we combined the A11 minibody with our novel polypeptide-based

gold nanoshells, and demonstrated the ability to generate A11-conjugated nanoshells with the appropriate size and heat generation properties. These PSCA-targeted polypeptide-based gold nanoshells also showed promise by exhibiting greater efficacy as a photothermal therapy agent compared to non-targeted gold nanoshells.

7 Appendix

7.1 MATLAB CODE for Model 2

```
clc
clear

%Physical parameters
r = 0.0032; % radius of well (m)
h = 0.0107; % height of well (m)
Twall = 298; % temperature of wall (C)
Tair = 298; % temperature of air (C)
rho = 1000; % density (kg/m^3)
cp = 4181; % specific heat (J/kg K)
alpha = 1.4E-7; %constant m^2/s (k = 0.6 W/m*K, Cp = 4181 J/kg*K, p = 1000 kg/m^3)
Uwall = 1E-5; %overall heat transfer coef (W/m^2 K)
k = 0.6; % thermal conductivity (W/m K)
Uair = 0.08; %heat convection coeff (W/m^2 C)

A = 0.3; % absorbance (a.u.)
c = A/0.01; %A/l = eps*conc, where l = path length (1cm), eps = absorption coefficient
I = 6220; % power density (W/m^2) = 500000 W/m^2 or if divided over the entire well = 6220 W/m^2
Q = c*I;

%numerical parameters
nr = 51; % # gridpoints in r direction
nz = 51; % # gridpoints in z direction
dr = r/(nr-1); % spacing of the grid in the r-direction
dz = h/(nz-1); % spacing of the grid in the z-direction

t = 600; %total time (s)
dt = min([dz,dr])^2/alpha/4 %compute stable time step
nt = t/dt; % # of time loops to get to desired t

[z2d,r2d] = meshgrid(h:dz:0,r:dr:0);% create grid
R = [0:dr:r];
Z = [0:dz:h];
```

```
% Setup inital temperature = inital T of  water
Told = ones(nz,nr).*298;

T = ones(nz,nr).*298;

Qlaser = (dt*Q)/(rho*cp);

time = 0;
for n = 1:nt
    %compute new temperature

  Told = T;

      for j = 2:nr-1
       for i = 2:nz-1

       T(i,j) = alpha*dt*((Told(i,j+1)-2*Told(i,j)+Told(i,j-1))/dr^2 ...
                   + 1/(dr*(j-1))*(Told(i,j+1)-Told(i,j-1))/2*dr ...
                   +(Told(i+1,j)-2*Told(i,j)+Told(i-1,j))/dz^2) ...
                    + Told(i,j)+ Qlaser;

       end
     end
```

```
%set B.C.

   T(:,1) = T(:,2); %flux to center is zero
   for i = 1:nz
       T(i,nr) = (T(i,nr-1) - ((Uwall*dr/k)*Twall))/(1 - (dr*Uwall/k)); %flux to wall is = flux through
   end

   for j = 1:nr
       T(nz,j) = (T(nz-1,j) +((Uair*dz/k)*Tair))/(1 +(dz*Uair/k)); %flux to water surface = convection
       T(1,j) = (T(2,j) + ((Uwall*dz/k)*Twall))/(1 + (dz*Uwall/k)); %flux to bottom = flux through

   end

   time = time+dt;

  if (mod(n,1000)==0) %graph reported
   figure (1); contourf(R, Z, T,'linestyle', 'none')
   b = colorbar;
   ylabel(b, 'Temperature (K)');
   xlabel('Radius (m)')
   ylabel('Height (m)')

   time

   disp(T(20,30))

  end

end
```

7.2 MATLAB CODE for Model 3

```
%Physical parameters
r2 = 0.0032; % radius of well (m)
r1 = 0.0005; %radius of laser (m)
h = 0.0107; % height of well (m)
Twall = 298; % temperature of wall (C)
Tair = 298; % temperature of air (C)
rho = 1000; % density (kg/m^3)
cp = 4181; % specific heat (J/kg K)
alpha = 1.4E-7; %constant m^2/s (k = 0.6 W/m*K, Cp = 4181 J/kg*K, p = 1000 kg/m^3)
Uwall = 1E-5; %overall heat transfer coef (W/m^2 C)
k = 0.6; % thermal conductivity (W/m K)
Uair = 0.08; %heat convection coeff (W/m^2 C)
A = 0.006; %(a.u.) --> Vcyl = 0.02Vwell (total abs = 0.3)
c = A/0.01; %A/l = eps*conc, where l = path length (1 cm), eps = absorption coefficient
I = 250000; %power density (W/m^2)

Q = c*I;

%numerical parameters
nr = 51; % # gridpoints in r direction
nz = 51; % # gridpoints in z direction
dr = (r2-r1)/(nr-1); % spacing of the grid in the r-direction
dz = h/(nz-1); % spacing of the grid in the z-direction

t = 600; %total time (s)
dt = min([dz,dr])^2/alpha/4; %compute stable time step
nt = t/dt; % # of time loops to get to desired t

[z2d,r2d] = meshgrid(h:dz:0,r2:dr:r1);% create grid
R = [r1:dr:r2];
Z = [0:dz:h];
```

```
% Setup inital temperature = inital T of  water
Told = ones(nz,nr).*298;

%T = zeros(nz,nr)
 T = ones(nz,nr).*298;

time = 0;
for n = 1:nt
%compute T at center cylinder
T0 = time*Q/(rho*cp) + 298;

%compute new temperature
   Told = T;

       for j = 2:nr-1
        for i = 2:nz-1
        T(i,j) = alpha*dt*((Told(i,j+1)-2*Told(i,j)+Told(i,j-1))/dr^2 ...
                    + 1/(r1+dr*(j-1))*(Told(i,j+1)-Told(i,j-1))/2*dr ...
                    +(Told(i+1,j)-2*Told(i,j)+Told(i-1,j))/dz^2) ...
                     + Told(i,j);
        end
       end
```

```
%set B.C.
  T(:,1) = T0; %Temp at node 1 = T0 from equation above
   for i = 1:nz
       T(i,nr) = (T(i,nr-1) - ((Uwall*dr/k)*Twall))/(1 - (dr*Uwall/k)); %flux to wall is = flux through wall
   end

   for j = 1:nr
       T(nz,j) = (T(nz-1,j) +((Uair*dz/k)*Tair))/(1 +(dz*Uair/k)); %flux to water surface =  away
       T(1,j) = (T(2,j) + ((Uwall*dz/k)*Twall))/(1 + (dz*Uwall/k)); %flux to bottom = flux through polystyrene
   end

   time = time+dt;

  if (mod(n,1000)==0) %graph reported every so many steps
   figure (1); contourf(R, Z, T,'linestyle', 'none')
   b = colorbar;
   ylabel(b, 'Temperature (K)');
   xlabel('Radius (m)')
   ylabel('Height (m)')

   time

   disp(T(20,30))

  end
end

  T
```

7.3 MATLAB CODE for Model 4

```
clc
clear

%Physical parameters
r2 = 0.0032; % radius of well (m)
r1 = 0.0005; %radius of laser (m)GKLTempCylCond
h = 0.005; % height of well (m)
Twall = 290; % temperature of wall (C)
Tair = 290; % temperature of air (C)
rho = 1000; % density (kg/m^3)
cp = 4184; % specific heat (J/kg K)
Uwall = 100; % overall heat transfer coef (W/m^2 C)= kwall/twall
k = 0.75; %0.598; % thermal conductivity (W/m K)
alpha = k/(cp*rho); %constant m^2/s (k = 0.598 W/m*K, Cp = 4184 J/kg*K, p = 1000 kg/m^3)
Uair = 15; %heat convection coeff (W/m^2 C)
ec = 51*0.114/0.01/10; %original dilution = 51x, original abs value = 0.114, path length = 0.01, new dilution = 10x
ecabs = 0.1*ec; %10 percent is absorbed based on Mie theory of our particles
I0 = 333000; %power density (W/m^2)--> 0.2W/6E-7m^2 (assume rectangle)
volevap = 20/600; %average volume rate of evaporation (uL/s) (assume over 10 min)
massevap = volevap/1E6 %average mass rate of evaporation (kg/s)
Hvap = 2461E3; %Heat of vaporization of water at 290K (J/kg)

%numerical parameters
nr = 51; % # gridpoints in r direction
nz = 51; % # gridpoints in z direction
dr = (r2)/(nr-1); % spacing of the grid in the r-direction
dz = h/(nz-1); % spacing of the grid in the z-direction

t = 1200; %total time (s)
dt = min([dz,dr])^2/alpha/4 %compute stable time step
nt = t/dt; % # of time loops to get to desired t
```

```

[z2d,r2d] = meshgrid(h:dz:0,r2:dr:r1);% create grid
R = [0:dr:r2];
Z = [0:dz:h];

% Setup inital temperature matrices = inital T of  water
Told = ones(nz,nr).*294;
T = ones(nz,nr).*294;

%Setup initial intensity and heat generation term (Qlaser) matrices
I = ones(nz,nr).*I0;
Qlaser = ones(nz,nr).*(dt*ecabs*I0)/(rho*cp);

%Prep loop counters
p=0;
time = 0;
```

```
for n = 1:nt

    Told = T;

    %Note: i = node in z-direction, j = node in r-direction
     for j = 2:7 % Energy balance including heat generation, which occurs within laser irradiated region (@ radial nodes 2:7)
         for i = 2:nz-1 %heat generation occurs at all z locations at the radial nodes 2:7

         I(i,:) = I0*10^(-ec*(h-(i*dz))); %Intensity at each location
         Qlaser(i,:) = (dt*ecabs*I(i,:))/(rho*cp); %Heat generation at each location (based on I(z))


         T(i,j) = alpha*dt*((Told(i,j+1)-2*Told(i,j)+Told(i,j-1))/dr^2 ...
                     + 1/(dr*(j-1))*(Told(i,j+1)-Told(i,j-1))/2*dr ...
                     +(Told(i+1,j)-2*Told(i,j)+Told(i-1,j))/dz^2) ...
                      + Told(i,j)+ Qlaser(i,j);

        end
      end

       for j = 9:nr-1 %Engergy balance without heat generation, occurs outside irradiated region
        for i = 2:nz-1
        T(i,j) = alpha*dt*((Told(i,j+1)-2*Told(i,j)+Told(i,j-1))/dr^2 ...
                     + 1/(r1+dr*(j-1))*(Told(i,j+1)-Told(i,j-1))/2*dr ...
                     +(Told(i+1,j)-2*Told(i,j)+Told(i-1,j))/dz^2) ...
                      + Told(i,j);
        end
       end

```

```
 %set B.C.
  T(:,1) = T(:,2); %flux to center is zero
  T(:,9) = T(:,8); %Temperature just inside irradiated region = temperature just outside irradiated region
  T(:,8) = (T(:,9)+T(:,7))/2; %flux from the irradiated region = flux leaving irradiated region
    for i = 1:nz
        T(i,nr) = (T(i,nr-1) + ((Uwall*dr/k)*Twall))/(1 + (dr*Uwall/k)); %flux to wall is = flux through wall
    end

    for j = 1:nr

        T(nz,j) = (T(nz-1,j) +((Uair*dz/k)*Tair)-(massevap*Hvap*dz)/(k*3.14*r2^2))/(1 +(dz*Uair/k)); %flux to water surface = (cont.)
                                                                                                    %=  flux away + evaporation
        T(1,j) = (T(2,j) + ((Uwall*dz/k)*Twall))/(1 + (dz*Uwall/k)); %flux to bottom = flux through polystyrene
    end
```

```

    time = time+dt; %increase time incrementally by dt

   if (mod(n,5000)==0) %graph reported every 5000 steps

    figure (1); contourf(R, Z, T,'linestyle', 'none') %generates temperature profile graph
    b = colorbar; %inserts colored temperature scale bar
    ylabel(b, 'Temperature (K)'); %labels scale bar
    xlabel('Radius (m)') %labels x-axis
    ylabel('Height (m)') %labels y-axis

    %Report time and temperature every 5000 steps
    time
    %Temperature is reported at node (i,j) = 40,45, which is near the top
    %and outer portion of the well
    disp(T(40,45))


   end
end

   T  %At end of the code display the temperature matrix

```

7.4 Determining the Internalization Rate Constant and Cellular Association of A11 Minibody

7.4.1 Materials and Methods

7.4.1.1 Radiolabeling A11 Minibody

Tyrosine residues of A11 were radiolabeled with $Na^{125}I$ using IODO-BEADS (Pierce, Rockford, IL) (Figure 7.1). Radiolabeled A11 samples were purified from free iodine-125 with a Sephadex G10 size exclusion column with bovine serum albumin (BSA) added to prevent nonspecific binding to the column. The phosphotungstic acid (PTA) assay was used to quantify the specific activity and concentration of each radiolabeled sample[116].

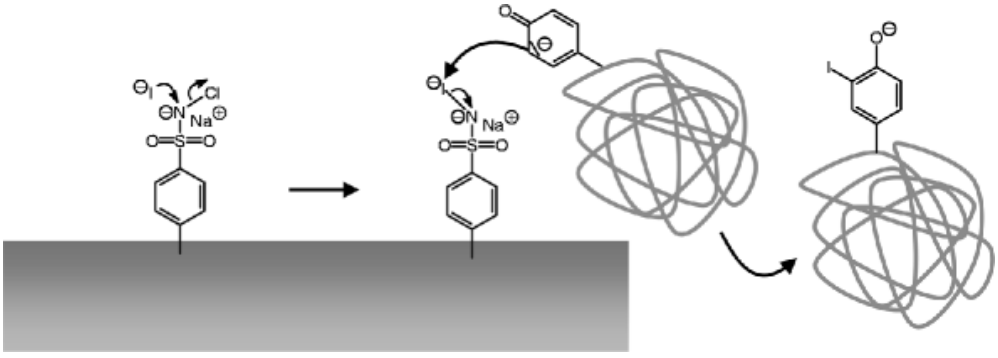

Figure 7.1. Reaction sequence for the radiodination of a protein with Iodobeads. In the first step, the *N*-cholor substituent of the benzenesulfonamide is substituted by radionucleotide. The covalently bound iodine reacts subsequently with an activated aromatic side chain of the protein. (Reprinted with permission from Radioiodination Chemistry and Radioiodinated Compounds. Eisenhut M, Mier W. Handbook of Nuclear Chemistry. 2011. 2121-2141. Copyright 2011. Springer Science+Business Media B.V.).

7.4.1.2 Cellular Binding and Trafficking

PSCA-transfected 22Rv1 prostate cancer cells were seeded onto 35 mm dishes (Becton Dickinson and Company, Franklin Lakes, NJ) with a seeding density of 1.25×10^5 cells/cm^2 in growth medium. The growth medium was RPMI 1640 supplemented with 10% fetal bovine

serum and 1% penicillin/streptomycin (pH 7.4). After 15 h of incubation in a humidified 5% CO_2 and 37°C environment, the growth medium was aspirated, and new incubation medium with 1 nM radiolabeled A11 was added to each dish. The incubation medium was RPMI 1640 supplemented with 20 mM 4-(2-hydroxyethyl)-1-piperazineethanesulfonic acid (HEPES) and 1% penicillin/streptomycin (pH 7.4). The cells were incubated in this medium at 37°C for 1, 2, 5, 7, 10, and 60 min. At each time point, the incubation medium was removed, and the cells were washed 5 times with ice-cold WHIPS (20 mM HEPES, 1 mg/mL polyvinylpyrrolidone (PVP), 130 mM NaCl, 5 mM KCl, 0.5 mM $MgCl_2$, and 1 mM $CaCl_2$, pH 7.4) to remove nonspecifically bound A11 on cell surfaces. Cell-surface bound A11 was then separated from internalized A11 by adding 1 mL of ice-cold acid strip (50 mM glycine-HCl, 100 mM NaCl, 1 mg/mL PVP, and 2 M urea, pH 3.0) to each dish. The cells were placed on ice for 12 min. Each dish was then washed once more with 1 mL of acid strip. The radioactivity in the collected acid strip washes was quantified using a Cobra Series Auto-Gamma Counter (Packard Instrument Co., Meriden, CT) to determine surface bound A11. Lastly, the cells were solubilized by adding 1 mL of a 1 N NaOH solution to each dish for 30 min, followed by another 1 mL NaOH wash. The two NaOH washes were collected, and the radioactivity in the solution was quantified as above to determine the amount of internalized A11. Each entire experiment was performed three times, where triplicate measurements were obtained for each time point in each experiment.

7.4.1.3 Mathematical Model of A11 Trafficking

Radiolabeled A11 minibody (1 nM) was incubated with 22Rv1 prostate cancer cells, and at desired time points, surface bound and internalized A11 was measured using a gamma counter. To remove the surface bound A11, an acid wash was applied to the cells, following removal of

nonspecifically bound A11 using WHIPS. Once the surface bound A11 was removed and collected, internalized A11 was collected using 1M NaOH washes.

In order to determine the internalization rate constant of the A11 minibody, a model of the cellular trafficking pathway was developed based on a species balance on the internalized A11. The change in internalized complexes with respect to time can be increased through internalization of the surface bound complexes, and is decreased through both recycling and degradation of the internalized complexes.

$$\frac{dC_i}{dt} = k_{int}C_s - k_{rec}C_i - k_{deg}C_i \qquad (7.1)$$

where, C_i is the concentration of internalized A11, t is the time, k_{int} is the internalization rate constant, C_s is the concentration of surface-bound A11, k_{rec} is the recycling rate constant, and k_{deg} is the degradation rate constant (Figure 7.2).

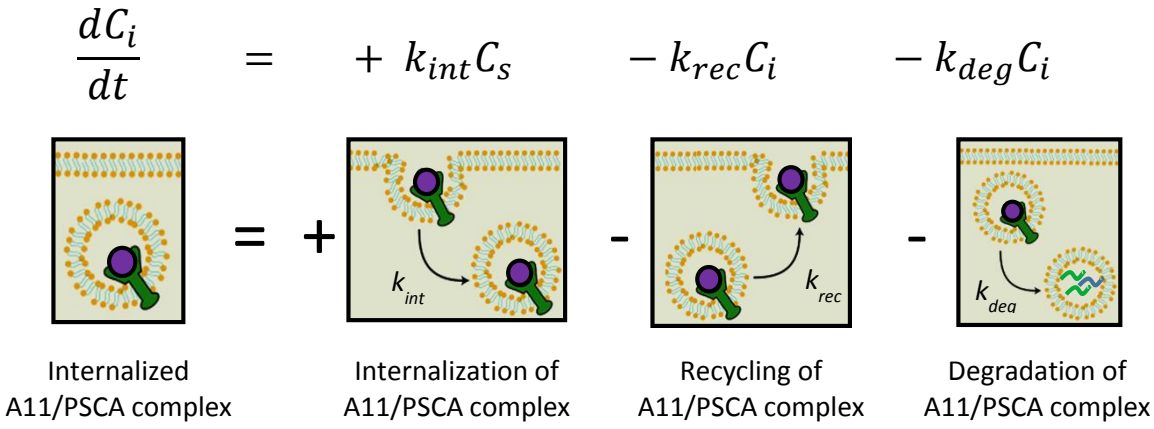

Figure 7.2. Species balance on internalized A11/PSCA complexes.

Short time points (less than 10 min) were chosen to allow recycling and degradation to be neglected. This allowed the simplification of the above equation to the following:

$$\frac{dC_i}{dt} = k_{int} C_s \quad (7.2)$$

Integrating the above equation and using the initial condition that no A11 is present inside the cell yields the following:

$$C_i = k_{int} \int_0^t C_s \, dt' \quad (7.3)$$

Based on Eq 7.3, the internalization rate constant can be determined as the slope of the graph of the concentration of internalized A11 as a function of the integral of the concentration of surface complexes over time. To obtain this data, radiolabeled A11 was incubated with 22Rv1 prostate cancer cells and the surface bound and internalized radiolabeled A11 was collected at the desired time points. As shown below, the trapezoidal rule was then applied to obtain the integral of the surface complexes over time.

$$\int_0^t C_s \, dt' = \frac{\Delta t}{2}\left[C_{s,0} + C_{s,1}\right] + \frac{\Delta t}{2}\left[C_{s,1} + C_{s,2}\right] \ldots . + \frac{\Delta t}{2}\left[C_{s,n-1} + C_{s,n}\right] \quad (7.4)$$

where $\Delta t = t_n - t_{n-1}$, which represents the time difference between the points when the surface and internalized complexes were measured, and $C_{s,n}$ is the concentration of surface complexes measured at $t = t_n$.

7.4.1.4 Development of A11-Conjugated PEGylated Nanocarriers

Fluorescently labeled polystyrene nanoparticles (Phosphorex, Hopkinton, MA) were conjugated with maleimide-PEG_{5000}-amine (Nanocs, Boston, MA) through activated carboxylate groups present on both the polystyrene nanoparticles. Briefly, the nanoparticles were placed in 2-(*N*-morpholino)ethanesulfonic acid (MES) buffer (pH 5.5) to allow activation of the surface carboxyl groups on the nanoparticles with 1-ethyl-3-(3-dimethylaminopropyl)-carbodiimide (EDC) and N-hydroxysuccinimide (NHS) (Sigma-Aldrich, St. Louis, MO). After 15 min, the reaction was quenched by raising the pH to 7.4 by adding 500mM phosphate buffer. The PEG linker was then added to the activated nanoparticles at a 5000:1 PEG:nanoparticle molar ratio. The solution was allowed to react for 2 h at room temperature to form a permanent linkage with the nanoparticles. Free EDC/NHS and PEG were purified using 30K MWCO spin concentrators (Pierce, Rockford, IL). Meanwhile, free thiol groups on A11 were exposed by breaking the disulfide linkages between A11 heavy chains using dithiolthreitol (DTT), which enabled conjugation to the maleimide groups on the PEG. The free DTT was purified from the thiolated A11 using a Zeba desalting column (Thermo Fisher Scientific, Inc, Rockford, IL) in phosphate buffer. The thiolated A11 was then incubated with the PEGylated nanoparticles at a molar ratio of 1000:1 A11:nanoparticle at room temperature overnight to allow formation of a permanent bond between the A11 and nanoparticle. Free A11 was purified using 100K MWCO spin concentrators, and the nanoparticles were resuspended in 50 mM HEPES for storage. The size and polydispersity index of the A11 minibody and the A11-conjugated nanoparticles were evaluated using dynamic light scattering with the Malvern Zetasizer Nano ZS model Zen 3600 (Malvern Instruments Inc, Westborough, Massachusetts).

7.4.1.5 Qualitative Cellular Uptake of Nanocarriers

The 22Rv1 prostate cancer cells were seeded in 8-well confocal plates at 125,000 cells/cm^2. Fluorescently-labeled nanocarriers were incubated with PSCA-transfected cells at a concentration of 10 μg/mL for 1 h. Non-specifically bound nanocarriers were removed by 3X PBS wash, and the cells were subsequently imaged using confocal microscopy. Laser scanning confocal microscopy images were taken on a Leica Inverted TCS-SP1 MP Spectral Confocal and Multiphoton Microscope (Heidelberg, Germany) equipped with an argon laser (476 and 488 nm blue excitation: JDS Uniphase), a diode laser (DPSS; 561 nm yellow-green excitation: Melles Griot), a helium-neon laser (633 nm red excitation), and a two-photon laser setup consisting of a Spectra-Physics Millenia X 532 nm green diode pump laser and a Tsunami Ti-sapphire picosecond pulsed infrared laser tuned at 768 nm for UV excitation.

7.4.2 Results and Discussion

7.4.2.1 Evaluate the Internalization Rate Constant for the A11 Minibody

In our studies, we characterized the internalization rate constant of A11 to obtain quantitative information about the internalization constant that could be used to help design an efficient drug delivery carrier. We developed a mathematical model to describe the cellular trafficking of A11, and the internalization rate constant was determined for PSCA-transfected 22Rv1 prostate cancer cells. We measured cellular binding and uptake. Similar to previous reports[115], we observed rapid binding of A11 to PSCA-expressing cells; however, cellular internalization was relatively low (Figure 7.3).

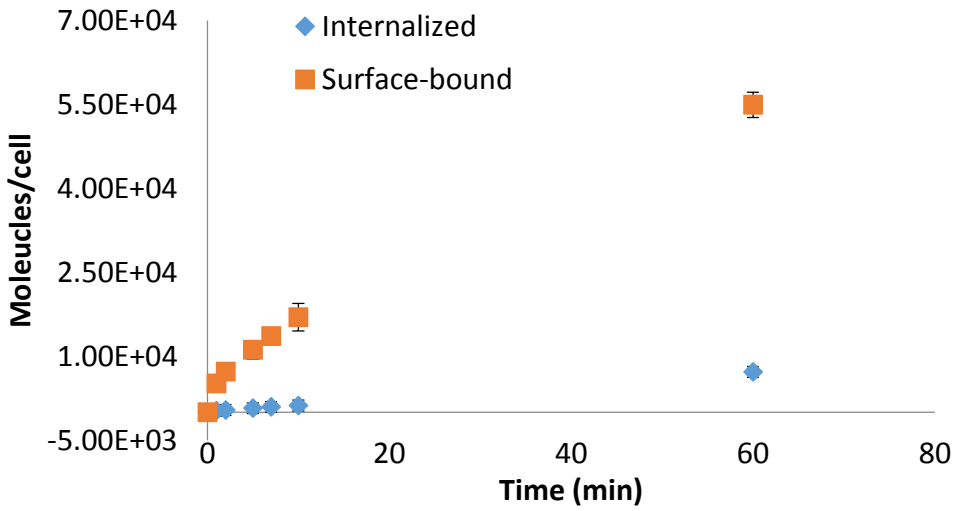

Figure 7.3. Radiolabeled A11 (1 nM) was incubated with PSCA-expressing 22Rv1 prostate cancer cells. The surface-bound and internalized A11 were measured at specific time points.

In order to focus on the binding and internalization processes, we used the data from Figure 7.3, at short time points (less than 10 minutes), where degradation and recycling processes could be neglected, thereby allowing us to focus on the binding and internalization processes. Plotting the data based on our model (Eq. (7.3)), the internalization rate constant was determined as the slope of the plot of the internalized A11 as a function of the integral of the cell surface complexes over time. The average internalization rate constant for PSCA-expressing 22Rv1 cells was found to be 0.0098 $\pm$ 0.0030 min^{-1} (Figure 7.4), which is considerably less than the internalization rate constant for ligands known to be endocytosed by cells (Table 7.1). Based on the specific binding of the A11 minibody, we chose to evaluate an A11-conjugated nanosized drug delivery vehicle.

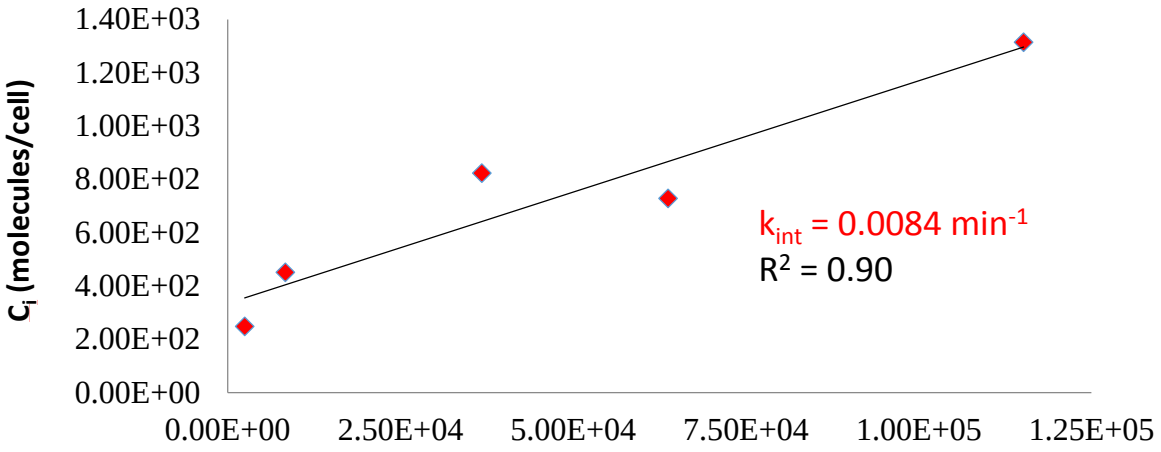

Figure 7.4. Determining the internalization rate constant for PSCA-transfected 22Rv1 prostate cancer cells.

Table 7.1. Internalization rate constants for internalized ligands.

Ligand	Internalization rate constant (k_{int})	Cell Type
Transferrin[117]	0.38 ± 0.05 min^{-1}	HeLa cervical cancer
Epidermal growth factor (EGF)[118]	0.04-0.16 min^{-1}	A431epidermoid carcinoma
Insulin[119]	0.186 ± 0.01 min^{-1}	Chinese Hamster Ovary (CHO)
Vascular endothelial growth factor (VEGF)[120]	0.282 min^{-1}	Human umbilical vein endothelial cells (HUVEC)

7.4.3 Evaluating Targeting of Nanosized Carrier Using the A11 Minibody

In order to evaluate the potential for A11 to specifically target nanosized drug carriers, we conjugated A11 to a model nanoparticle system. The size and polydispersity index of the A11-conjugated nanoparticles is shown in Table 7.2, where the A11 minibody was measured to be 9.3 ± 0.1 nm in size. In these studies, A11 enhanced the cellular association of the nanocarriers with PSCA-expressing prostate cancer cells, while non-targeted nanocarriers showed limited cellular association (Figure 7.5). This difference in uptake indicates the potential for improved specificity for delivery of the nanocarriers to local and metastatic prostate cancer cells that express PSCA. These results indicate that A11-conjugated nanocarriers have the potential to effectively target prostate cancer cells.

Table 7.2. Characterization of the A11-conjugated model nanoparticles

Sample	Diameter (nm)	Polydispersity Index
Model Nanoparticle	103	0.25
A11-conjugated nanoparticle	133	0.19

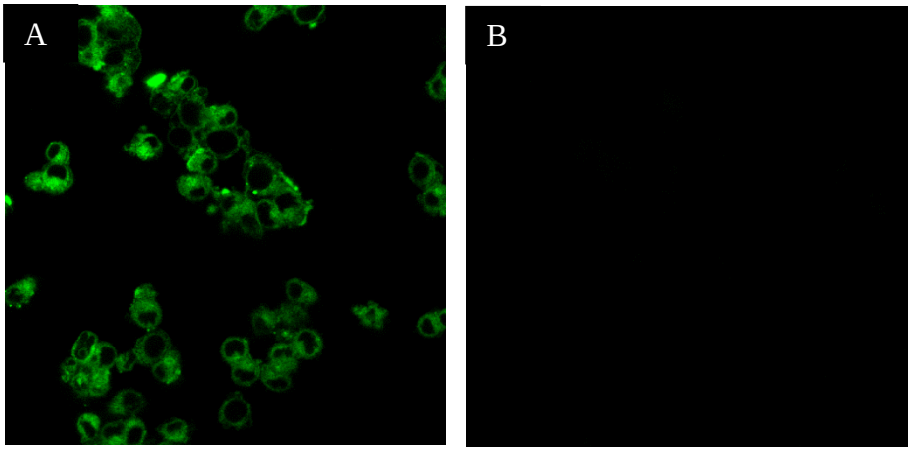

Figure 7.4. For PSCA-transfected 22Rv1 prostate cancer cells (A) A11-conjugated and (B) non-targeted PEGylated nanocarriers were incubated for 1 h and imaged using confocal microscopy.

8 References

1 R. Gulati, E. M. Wever, A. Tsodikov, D. F. Penson, L. Y. T. Inoue, J. Katcher, S.-Y. Lee, E. A. M. Heijnsdijk, G. Draisma, H. J. de Koning and R. Etzioni, *Cancer Epidemiol. Biomarkers Prev.*, 2011, **20**, 740–50.

2 A. B. Barqawi, K. J. Krughoff and K. Eid, *Adv. Urol.*, 2012, **2012**, 862639.

3 H. Maeda, J. Wu, T. Sawa, Y. Matsumura and K. Hori, *J. Control. Release*, 2000, **65**, 271–284.

4 H. U. Ahmed, C. Moore and M. Emberton, *Surg. Oncol.*, 2009, **18**, 219–32.

5 U. Lindner, R. A. Weersink, M. A. Haider, M. R. Gertner, S. R. H. Davidson, M. Atri, B. C. Wilson, A. Fenster and J. Trachtenberg, *J. Urol.*, 2009, **182**, 1371–7.

6 U. Choe, V. Z. Sun, J. Y. Tan and D. T. Kamei, 2011.

7 J. F. Lutz and H. G. Börner, *Prog. Polym. Sci.*, **33**, 1–39.

8 W. Chan, *Fmoc solid phase peptide synthesis : a practical approach*, Oxford University Press, New York, 2000.

9 S. B. Kent, *Annu. Rev. Biochem.*, 1988, **57**, 957–89.

10 H.-A. Klok, *Angew. Chemie Int. Ed.*, 2002, **41**, 1509–1513.

11 S. Plaue, S. Muller, J. P. Briand and M. H. V. Van Regenmortel, *Biologicals*, 1990, **18**, 147–157.

12 P. E. Dawson and S. B. Kent, *Annu. Rev. Biochem.*, 2000, **69**, 923–60.

13 T. W. Muir, P. E. Dawson and S. B. H. Kent, *Solid-Phase Peptide Synthesis*, Elsevier, 1997, vol. 289.

14 A. C. Braisted, J. Kevin Judice and J. A. Wells, *Solid-Phase Peptide Synthesis*, Elsevier, 1997, vol. 289.

15 D. W. P. M. Löwik, L. Ayres, J. M. Smeenk and J. C. M. Van Hest, *Peptide Hybrid Polymers*, Springer Berlin Heidelberg, Berlin, Heidelberg, 2006, vol. 202.

16 R. L. DiMarco and S. C. Heilshorn, *Adv. Mater.*, 2012, **24**, 3923–40.

17 J. C. M. van Hest and D. A. Tirrell, *Chem. Commun.*, 2001, 1897–1904.

18 C. J. Noren, S. J. Anthony-Cahill, M. C. Griffith and P. G. Schultz, *Science*, 1989, **244**, 182–8.

19 J. A. Johnson, Y. Y. Lu, J. A. Van Deventer and D. A. Tirrell, *Curr. Opin. Chem. Biol.*, 2010, **14**, 774–80.

20 A. J. van Hell, C. I. C. A. Costa, F. M. Flesch, M. Sutter, W. Jiskoot, D. J. A. Crommelin, W. E. Hennink and E. Mastrobattista, *Biomacromolecules*, 2007, **8**, 2753–61.

21 A. J. van Hell, D. J. A. Crommelin, W. E. Hennink and E. Mastrobattista, *Pharm. Res.*, 2009, **26**, 2186–93.

22 A. J. van Hell, M. M. Fretz, D. J. A. Crommelin, W. E. Hennink and E. Mastrobattista, *J. Control. Release*, 2010, **141**, 347–53.

23 E. P. Holowka, D. J. Pochan and T. J. Deming, *J. Am. Chem. Soc.*, 2005, **127**, 12423–8.

24 H. Kukula, H. Schlaad, M. Antonietti and S. Förster, *J. Am. Chem. Soc.*, 2002, **124**, 1658–1663.

25 J. Rodríguez-Hernández and S. Lecommandoux, *J. Am. Chem. Soc.*, 2005, **127**, 2026–7.

26 H. Lu, J. Wang, Y. Bai, J. W. Lang, S. Liu, Y. Lin and J. Cheng, *Nat. Commun.*, 2011, **2**, 206.

27 O. Lagrille, G. Danger, L. Boiteau, J.-C. Rossi and J. Taillades, *Amino Acids*, 2009, **36**, 341–7.

28 E. R. Blout and R. H. Karlson, *J. Am. Chem. Soc.*, 1956, **78**, 941–946.

29 J. Cheng and T. J. Deming, *Top. Curr. Chem.*, 2012, **310**, 1–26.

30 H. Werner, *Angew. Chemie*, 1988, **100**, 1145–1146.

31 T. J. Deming, *Macromolecules*, 1999, **32**, 4500–4502.

32 T. J. Deming, *Nature*, 1997, **390**, 386–9.

33 T. J. Deming, *J. Polym. Sci. Part A Polym. Chem.*, 2000, **38**, 3011–3018.

34 T. J. Deming and S. A. Curtin, *J. Am. Chem. Soc.*, 2000, **122**, 5710–5717.

35 T. J. Deming, *Soft Matter*, 2005, **1**, 28.

36 D. M. Copolovici, K. Langel, E. Eriste and Ü. Langel, *ACS Nano*, 2014, **8**, 1972–94.

37 F. Heitz, M. C. Morris and G. Divita, *Br. J. Pharmacol.*, 2009, **157**, 195–206.

38 A. D. Frankel and C. O. Pabo, *Cell*, 1988, **55**, 1189–1193.

39 M. Green and P. M. Loewenstein, *Cell*, 1988, **55**, 1179–88.

40 D. Derossi, A. H. Joliot, G. Chassaing and A. Prochiantz, *J. Biol. Chem.*, 1994, **269**, 10444–50.

41 J. Oehlke, A. Scheller, B. Wiesner, E. Krause, M. Beyermann, E. Klauschenz, M. Melzig and M. Bienert, *Biochim. Biophys. Acta*, 1998, **1414**, 127–39.

42 M. Pooga, M. Hällbrink, M. Zorko and U. Langel, *FASEB J.*, 1998, **12**, 67–77.

43 U. Soomets, M. Lindgren, X. Gallet, M. Hällbrink, A. Elmquist, L. Balaspiri, M. Zorko, M. Pooga, R. Brasseur and U. Langel, *Biochim. Biophys. Acta*, 2000, **1467**, 165–76.

44 G. Elliott and P. O'Hare, *Cell*, 1997, **88**, 223–33.

45 S. Futaki, T. Suzuki, W. Ohashi, T. Yagami, S. Tanaka, K. Ueda and Y. Sugiura, *J. Biol. Chem.*, 2001, **276**, 5836–40.

46 M. C. Morris, P. Vidal, L. Chaloin, F. Heitz and G. Divita, *Nucleic Acids Res.*, 1997, **25**, 2730–6.

47 L. Chaloin, P. Vidal, P. Lory, J. Méry, N. Lautredou, G. Divita and F. Heitz, *Biochem. Biophys. Res. Commun.*, 1998, **243**, 601–8.

48 P. Säälik, A. Elmquist, M. Hansen, K. Padari, K. Saar, K. Viht, U. Langel and M. Pooga, *Bioconjug. Chem.*, **15**, 1246–53.

49 M. Lindgren, K. Rosenthal-Aizman, K. Saar, E. Eiríksdóttir, Y. Jiang, M. Sassian, P. Ostlund, M. Hällbrink and U. Langel, *Biochem. Pharmacol.*, 2006, **71**, 416–25.

50 S. El-Andaloussi, H. J. Johansson, T. Holm and U. Langel, *Mol. Ther.*, 2007, **15**, 1820–6.

51 L. Crombez, G. Aldrian-Herrada, K. Konate, Q. N. Nguyen, G. K. McMaster, R. Brasseur, F. Heitz and G. Divita, *Mol. Ther.*, 2009, **17**, 95–103.

52 A. Bolhassani, *Biochim. Biophys. Acta*, 2011, **1816**, 232–46.

53 S. Deshayes, M. C. Morris, G. Divita and F. Heitz, *Cell. Mol. Life Sci.*, 2005, **62**, 1839–49.

54 H. Tang, L. Yin, K. H. Kim and J. Cheng, *Chem. Sci.*, 2013, **4**, 3839.

55 Z. Song, N. Zheng, X. Ba, L. Yin, R. Zhang, L. Ma and J. Cheng, *Biomacromolecules*, 2014, **15**, 1491–7.

56 M. Magzoub and A. Gräslund, *Q. Rev. Biophys.*, 2004, **37**, 147–195.

57 F. Madani, S. Lindberg, U. Langel, S. Futaki and A. Gräslund, *J. Biophys.*, 2011, **2011**, 414729.

58 B. R. Meade and S. F. Dowdy, *Adv. Drug Deliv. Rev.*, 2008, **60**, 530–6.

59 A. Som, A. Reuter and G. N. Tew, *Angew. Chem. Int. Ed. Engl.*, 2012, **51**, 980–3.

60 A. Som, A. O. Tezgel, G. J. Gabriel and G. N. Tew, *Angew. Chem. Int. Ed. Engl.*, 2011, **50**, 6147–50.

61 E. I. Geihe, C. B. Cooley, J. R. Simon, M. K. Kiesewetter, J. A. Edward, R. P. Hickerson, R. L. Kaspar, J. L. Hedrick, R. M. Waymouth and P. A. Wender, *Proc. Natl. Acad. Sci. U. S. A.*, 2012, **109**, 13171–6.

62 K. M. Patil, R. J. Naik, Rajpal, M. Fernandes, M. Ganguli and V. A. Kumar, *J. Am. Chem. Soc.*, 2012, **134**, 7196–9.

63 J. R. Kramer and T. J. Deming, *J. Am. Chem. Soc.*, 2012, **134**, 4112–5.

64 N. P. Gabrielson, H. Lu, L. Yin, D. Li, F. Wang and J. Cheng, *Angew. Chem. Int. Ed. Engl.*, 2012, **51**, 1143–7.

65 J. R. Kramer and T. J. Deming, *Biomacromolecules*, 2012, **13**, 1719–23.

66 A. C. Roche, I. Fajac, S. Grosse, N. Frison, C. Rondanino, R. Mayer and M. Monsigny, *Cell. Mol. Life Sci.*, 2003, **60**, 288–297.

67 W. J. Kollen, P. Midoux, P. Erbacher, A. Yip, A. C. Roche, M. Monsigny, M. C. Glick and T. F. Scanlin, *Hum. Gene Ther.*, 1996, **7**, 1577–86.

68 I. Fajac, P. Briand, M. Monsigny and P. Midoux, *Hum. Gene Ther.*, 1999, **10**, 395–406.

69 A. L. Kierszenbaum, E. Rivkin, P. L. Chang, L. L. Tres and C. A. Olsson, *Prostate*, 2000, **43**, 175–83.

70 J. J. Lundquist and E. J. Toone, *Chem. Rev.*, 2002, **102**, 555–78.

71 S. S. Gambhir, *Nat. Rev. Cancer*, 2002, **2**, 683–93.

72 R. B. Hamanaka and N. S. Chandel, *J. Exp. Med.*, 2012, **209**, 211–5.

73 S. L. Deutscher, S. D. Figueroa and S. R. Kumar, *Nucl. Med. Biol.*, 2009, **36**, 137–46.

74 E. Vivès, P. Brodin and B. Lebleu, *J. Biol. Chem.*, 1997, **272**, 16010–7.

75 X. Huang and M. A. El-Sayed, *J. Adv. Res.*, 2010, **1**, 13–28.

76 P. K. Jain, K. S. Lee, I. H. El-Sayed and M. A. El-Sayed, *J. Phys. Chem. B*, 2006, **110**, 7238–48.

77 S. Link and M. A. El-Sayed, *J. Phys. Chem. B*, 1999, **103**, 8410–8426.

78 S. Link and M. A. El-Sayed, *Int. Rev. Phys. Chem.*, 2000, **19**, 409–453.

79 S. . Oldenburg, R. . Averitt, S. . Westcott and N. . Halas, *Chem. Phys. Lett.*, 1998, 288, 243–247.

80 Y. Hu, R. C. Fleming and R. A. Drezek, *Opt. Express*, 2008, **16**, 19579–91.

81 J. G. Morton, E. S. Day, N. J. Halas and J. L. West, *Methods Mol. Biol.*, 2010, **624**, 101–17.

82 E. Prodan and P. Nordlander, *Nano Lett.*, 2003, **3**, 543–547.

83 E. Prodan, C. Radloff, N. J. Halas and P. Nordlander, *Science*, 2003, **302**, 419–422.

84 L. C. Kennedy, L. R. Bickford, N. A. Lewinski, A. J. Coughlin, Y. Hu, E. S. Day, J. L. West and R. A. Drezek, *Small*, 2011, **7**, 169–83.

85 K. R. Brown and M. J. Natan, *Langmuir*, 1998, **14**, 726–728.

86 C. Wu, C. Yu and M. Chu, *Int. J. Nanomedicine*, 2011, **6**, 807–13.

87 R. Bardhan, N. K. Grady, T. Ali and N. J. Halas, *ACS Nano*, 2010, **4**, 6169–79.

88 E. FarrokhTakin, G. Ciofani, G. L. Puleo, G. de Vito, C. Filippeschi, B. Mazzolai, V. Piazza and V. Mattoli, *Int. J. Nanomedicine*, 2013, **8**, 2319–31.

89 K.-T. Yong, Y. Sahoo, M. T. Swihart and P. N. Prasad, *Colloids Surfaces A Physicochem. Eng. Asp.*, 2006, **290**, 89–105.

90 S. Leung and M. Romanowski, in *Technical Proceedings of the 2011 NSTI Nanotechnology Conference and Expo, NSTI-Nanotech 2011*, 2011, vol. 3, pp. 295–297.

91 S. J. Leung, X. M. Kachur, M. C. Bobnick and M. Romanowski, *Adv. Funct. Mater.*, 2011, **21**, 1113–1121.

92 T. S. Troutman, S. J. Leung and M. Romanowski, *Adv. Mater.*, 2009, **21**, 2334–2338.

93 A. Laszlo, *Cell Prolif.*, 1992, **25**, 59–87.

94 J. R. Lepock, *Int. J. Hyperthermia*, **19**, 252–66.

95 X. Huang, P. K. Jain, I. H. El-Sayed and M. A. El-Sayed, *Photochem. Photobiol.*, **82**, 412–7.

96 H.-C. Huang, K. Rege and J. J. Heys, *ACS Nano*, 2010, **4**, 2892–900.

97 I. L. Maksimova, G. G. Akchurin, B. N. Khlebtsov, G. S. Terentyuk, G. G. Akchurin, I. A. Ermolaev, A. A. Skaptsov, E. P. Soboleva, N. G. Khlebtsov and V. V. Tuchin, *Med. Laser Appl.*, 2007, **22**, 199–206.

98 A. Elliott, J. Schwartz, J. Wang, A. Shetty, J. Hazle and J. R. Stafford, *Lasers Surg. Med.*, 2008, **40**, 660–5.

99 R. D. Averitt, S. L. Westcott and N. J. Halas, *J. Opt. Soc. Am. B*, 1999, **16**, 1824.

100 W. Callister, *Materials Science and Engineering: An Introduction*, Wiley, 6th edn., 2002.

101 F. Incopera, D. Dewitt, T. Bergman and A. Lavine, *Introduction to Heat Transfer*, Wiley, 5th edn., 2006.

102 A. R. Lowery, A. M. Gobin, E. S. Day, N. J. Halas and J. L. West, *Int. J. Nanomedicine*, 2006, **1**, 149–54.

103 R. J. Bernardi, A. R. Lowery, P. A. Thompson, S. M. Blaney and J. L. West, *J. Neurooncol.*, 2008, **86**, 165–72.

104 A. M. Gobin, J. J. Moon and J. L. West, *Int. J. Nanomedicine*, 2008, **3**, 351–8.

105 M. P. Melancon, W. Lu, Z. Yang, R. Zhang, Z. Cheng, A. M. Elliot, J. Stafford, T. Olson, J. Z. Zhang and C. Li, *Mol. Cancer Ther.*, 2008, **7**, 1730–9.

106 S.-Y. Liu, Z.-S. Liang, F. Gao, S.-F. Luo and G.-Q. Lu, *J. Mater. Sci. Mater. Med.*, 2010, **21**, 665–74.

107 R. E. Reiter, Z. Gu, T. Watabe, G. Thomas, K. Szigeti, E. Davis, M. Wahl, S. Nisitani, J. Yamashiro, M. M. Le Beau, M. Loda and O. N. Witte, *Proc. Natl. Acad. Sci.*, 1998, **95**, 1735–1740.

108 Z. Gu, G. Thomas, J. Yamashiro, I. P. Shintaku, F. Dorey, A. Raitano, O. N. Witte, J. W. Said, M. Loda and R. E. Reiter, *Oncogene*, 2000, **19**, 1288–96.

109 D. C. Saffran, A. B. Raitano, R. S. Hubert, O. N. Witte, R. E. Reiter and A. Jakobovits, *Proc. Natl. Acad. Sci. U. S. A.*, 2001, **98**, 2658–63.

110 Z. Gu, J. Yamashiro, E. Kono and R. E. Reiter, *Cancer Res.*, 2005, **65**, 9495–500.

111 T. Olafsen, Z. Gu, M. A. Sherman, J. V Leyton, M. E. Witkosky, J. E. Shively, A. A. Raubitschek, S. L. Morrison, A. M. Wu and R. E. Reiter, *J. Immunother.*, 2007, **30**, 396–405.

112 J. V. Leyton, T. Olafsen, E. J. Lepin, S. Hahm, K. B. Bauer, R. E. Reiter and A. M. Wu, *Clin. Cancer Res.*, 2008, **14**, 7488–7496.

113 A. M. Wu and P. D. Senter, *Nat. Biotechnol.*, 2005, **23**, 1137–46.

114 E. J. Lepin, J. V. Leyton, Y. Zhou, T. Olafsen, F. B. Salazar, K. E. McCabe, S. Hahm, J. D. Marks, R. E. Reiter and A. M. Wu, *Eur. J. Nucl. Med. Mol. Imaging*, 2010, **37**, 1529–1538.

115 S. M. Knowles, K. A. Zettlitz, R. Tavaré, M. M. Rochefort, F. B. Salazar, D. B. Stout, P. J. Yazaki, R. E. Reiter and A. M. Wu, *J. Nucl. Med.*, 2014, **55**, 452–9.

116 G. Lake-Bakaar, C. E. Rubio, S. McKavanagh, B. J. Potter and J. A. Summerfield, *Gut*, 1980, **21**, 580–6.

117 P. T. Yazdi and R. M. Murphy, *Cancer Res.*, 1994, **54**, 6387–6394.

118 H. S. Wiley, *J. Cell Biol.*, 1988, **107**, 801–10.

119 J. M. Backer, S. E. Shoelson, E. Haring and M. F. White, *J. Cell Biol.*, 1991, **115**, 1535–45.

120 S. M. Anderson, B. Shergill, Z. T. Barry, E. Manousiouthakis, T. T. Chen, E. Botvinick, M. O. Platt, M. L. Iruela-Arispe and T. Segura, *Integr. Biol. (Camb).*, 2011, **3**, 887–96.

121 K. L. Kelly, E. Coronado, L. L. Zhao and G. C. Schatz, *J. Phys. Chem. B*, 2003, **107**, 668–677.

122 Z. Qin and J. C. Bischof, *Chem. Soc. Rev.*, 2012, **41**, 1191–217.